Lehrstuhl für Anorganische und Analytische Chemie
Technische Universität München

Sol-Gel Derived Nanocomposites

-Synthesis, Spectroscopy, Atomic Force Microscopy-

Giovanni Schiavon

Vollständiger Abdruck der von der Fakultät für Chemie der Technischen Universität München zur Erlangung des akademischen Grades eines

Doktors der Naturwissenschaften

genehmigten Dissertation.

Vorsitzender: Univ.-Prof. Dr. St. Glaser

Prüfer der Dissertation: 1. Univ.-Prof. Dr. W. Hiller

2. Univ.-Prof. Dr. Dr.h.c. St. Veprek

3. Prof. B. Corain, Univ. degli studi di Padova / Italien

Die Dissertation wurde am 20.10.2000 bei der Technischen Universität München eingereicht und durch die Fakultät für Chemie am 23.11.2000 angenommen.

Dank

Per Sofia

Sol-Gel Derived Nanocomposites

-Synthesis, Spectroscopy, Atomic Force Microscopy-

Introduction

Material science represents a branch of the natural sciences that becomes more and more crucial in a world dominated by the importance of the choosing of the correct material. New materials are required for a wide variety of applications, which have to be extremely specialized and at the same time economically affordable. High technology materials are required in every technological field, ranging from opto-electronics or bio-materials for medical application to building materials, and they must be designed or invented with great care.

The technological effort in every field of material science involves chemistry as the primary source of materials, which can be designed starting from the molecular scale. The chemists are therefore called on to participate in the challenge of producing new materials and of optimizing and characterizing those that are already known. A correct scientific approach to the problems involved in the development of a new material requires, in fact, a continuous feedback from the loop design-synthesis-characterization-application, where the importance of every single step is decisive for successful results.

In this scenario the use of hybrid materials opens new routes to the production of materials, whose properties can be tailored depending on the demands for the different applications. Their properties, in fact, can be chosen so as to obtain the best performances of the plastic materials and the inherent stability of the inorganic ones. In particular, when the two phases are structured on a nanometer scale, the result can be considered under any point of view as a new material, with properties and a structure that can diverge from those of the starting components.

This approach to developing new materials gives the scientist an extremely wide range of parameters to play with in obtaining the desired properties. A deep knowledge of the role of every single parameter becomes more and more important as the range of possibilities increases.

As building materials, organic-inorganic hybrids are used mainly as a way to improve the properties of polymers, the inorganic particles often simply being mixed in

1

with the organic part. A wide range of treatments aimed at reducing and homogenizing the inorganic particles before they are introduced into the mixture can be done.

In the special field of stone restoration and consolidation, however, the use of hybrids is applied as a method of combining the mechanical properties of a plastic material with the necessity of using a substance as similar as possible to the stone itself. In this mixture, the inorganic part is supposed to provide the grip between the stone grains and the consolidant, while the organic part provides the elasticity and the adhesion properties necessary for an effective consolidation.

In this work the material studied is produced by the growing of an inorganic network into a preformed organic one, through the sol-gel technique. In this case a crucial role is played by the distribution of the two phases during the formation of the hybrid, and in some cases a full phase separation leads, unfortunately, to the failure of the synthesis of the desired material. In order to prevent this phase separation and to obtain a product with the desired properties, a great effort must be done to fully understand the processes involved in the formation of such a hybrid materials, especially at a nanometric level. In particular new analytical techniques are required to follow these processes.

Atomic Force Microscopy (AFM) is certainly one of the main techniques, which permits not only a deep look into the topography of the materials, but also a characterization of some of its properties. The sharp probe scanned across the sample during the AFM imaging, for example, can be used to test the mechanical properties of the material at the surface and to correlate them to the topographical position. Differing from other techniques, the extremely small dimensions of the tip used in AFM allow this information to be obtained with a resolution of few nanometers. Such a small probe can also be used to test many other properties of the surface, depending on the different possible interactions between the tip and the sample that can be monitored. Owing to the great number of possibilities, many special techniques based on the AFM technology are still not fully developed.

The innovation in this approach consists in the use of AFM to analyze materials which are usually considered only as bulk materials. Building materials, in fact, are rarely considered other than bulk, but it is now clear that an intimate knowledge of the processes involved at a microscopic level in order to understand the macroscopic properties, is necessary. In particular, the use of a special feature of the AFM called Force Modulation, based on the different mechanical properties of the components, allows us to evaluate the effects of the compositional variables on the nanostructure of the new material.

Moreover, this approach allows the study of the materials under conditions as similar as possible to those used for restoration purposes. The complexity and innovation involved in the study of the nanostructure of hybrid materials and, in particular, of materials for the protection and consolidation of natural stones, justifies the great effort done to develop a new analytical method for these materials based on AFM.

Chapter 1

The chemistry of the stone protection and consolidation.

1.1   Introduction

A wide range of treatments to protect and consolidate the stone monuments have been applied over the last centuries. The first known source about the procedures is the "*Architectura Libri Decem*" written by the roman author Vitruvius Pollio (84-10 B.C.). Most of the times the restoration of such monuments was intended as a replacement of the damaged parts, but a long tradition is documented about the use of oils, natural resins and bees' wax as protective and hydrophobic coating. Many times such substances were applied directly by the sculptor himself, and it's hard to distinguish between decorative and protective function of the coatings. Only in the XIX century, with the industrialisation of the urban areas, the problem became more and more important and studied.

The decay of stone in building and monuments is influenced by several weathering agents such as atmosphere, rainwater and rising ground moisture. Therefore a central role in the determination of the rate of destruction of the stone is played by the climate of the area in which the building or the monuments is located [1-3].

The presence of oxygen, for example, leads to oxidation of some of the components of the stone, while the moisture leads to hydration or dissolution. Moreover the chemical process of weathering is aided by mechanical break-up, which leads to the rapid enlargement of the mineral surfaces, providing accessibility to oxygen and moisture and resulting in accelerated destruction.

In the last century however, the air pollution due to the increasing industrialisation of the urban areas caused a strong acceleration of the stone decay, due mainly to chemical agents present in the atmosphere. The presence of SO_2 and SO_3 due to combustion of fossil fuels, coal, oil and gas causes the formation of sulphuric acid, which reacts easily with

limestone and marble bringing to the formation of gypsum, while the presence of combustion residuals and other particles, leads to the formation of the so called "black crusts" on the exposed surface.

Because all that, the rapid decay and disfiguring of stone monuments caused from chemical weathering is in fact nowadays a great challenge for conservators and a great effort is now made for protecting them from premature or further decay. On this purpose many different materials, both organic and inorganic, have been tested in order to find new treatments, which respond to the required characteristics [2, 3].

1.2   Characteristics of treatments.

An ideal treatment should penetrate the decayed stone, bind it together and secure it onto the sound stone beneath. It should protect the stone from further decay and it must be completely invisible. In order to avoid internal stresses, the treated stone should also have the same moisture and thermal expansion and elastic modulus as the sound stone. Possibly the treatment is also cheap, easy to apply and remain effective for a reasonable lapse of time. Unfortunately a general solution is not possible because the physical and chemical characteristics of an unlimited variety of stone types must be considered [4, 5].

In order to have a better comprehension of the processes involved in stone treatments, the action of the substances that are used can be divided in two main categories: sealers and penetrating stone consolidants.

1.3   Sealers.

The characteristic of sealers is to develop a tight, impervious surface skin, which prevents the access of moisture. Surface sealing eliminates the access of atmospheric humidity, but pressure tends to develop behind the stone surface by the escape of moisture

and flaking results when moisture is trapped behind a sealed surface, and pulled to the surface by temperature differentials. An ideal sealer should bar the flow of water from the outside, but permit the evaporation of humidity in order to reduce the internal pressure. Linseed oil and paraffin have been in use for centuries, as more recently silicones, urethanes, acrylate, epoxydic resins and other polymers. The main problem with such organic sealants is that they are not very stable over long periods of time and they can be attacked by UV radiations, causing yellowing, embrittlement and peeling of the treated surface. Acrylate seems to be the most suitable for the purpose of stone restoration.

1.4   Stone consolidants.

Stone solidification is intended as the process to replace natural grain cement lost by weathering from the stone surface inward [2, 3]. The treated stone should have improved its mechanical properties and the access of water and other salt solutions should be inhibited. The main problem is of course, the penetration depth of such treatments, and a great role is played by properties like density, volatility and contact angle of the applied solution.

The treatment employed should be appropriate for the particular stone that have to be handled. The chemical and physical characteristics of the stone determine, in fact, the kind of interaction with the material used for the consolidation process. In general the consolidants are chosen so to introduce compounds as similar as possible to the treated stone.

Two main classes stones can be considered: limestone and sandstone. For the first class of stones, consolidants are employed that introduces calcium carbonate. For the second class, silica is the final product of the consolidation. Very important is also the way in which any specific compound is applied to the stone and the environmental conditions. Sometimes the treatment is required to be reversible, in order to allow successive or different handling on the artwork.

Consolidants can be both organic [5] and inorganic [6] compounds, or a mixture between them. In general Inorganic consolidants are more hard and fragile respect the organic ones, but do not have problems of degradation typical of the polymers. Hybrid composites seem to be therefore the right synthesis between the best properties of both organic and inorganic consolidants. [7].

1.5   Inorganic consolidants for limestone

1.5.1   Limewater.

Limewater and calcium bicarbonate are the oldest and most natural methods of restoring calcitic sediments. The deposition of $CaCO_3$ resulting from the reaction:

$$Ca(OH)_2 + CO_2 \rightarrow CaCO_3 + H_2O$$
$$Ca(HCO_3)_2 \rightarrow CaCO_3 + CO_2 + H_2O$$
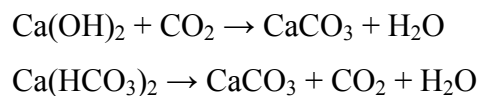
should replace the natural material solved by weathering. Unfortunately the conditions (pressure, temperature, etc) in which the newly formed $CaCO_3$ is deposited inside the stone are very different from those under which the natural stones has formed. Since long time the effectiveness of this method has proved to be not sufficient for the restoration purpose.

1.5.2   Barium Hydroxide

This method is based on the replacement of soluble carbonates with nearly insoluble barium carbonates and was developed and tested by Bear and Lewin. It is based on the reaction:

$$Ba(OH)_2 + CO_2 \rightarrow BaCO_3 + H_2O$$
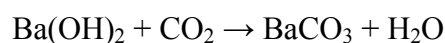
The Ba^{2+} ions should also replace the Ca^{2+} ions in the crystal lattice of the stone grains. The ions replacement is unfortunately too slow and the change of colour and blotchiness make this process undesirable.

1.5.3   Potassium aluminates.

A method similar to that of limewater involves the replacement of lost material with alumina, which can be formed from potassium aluminate:

$$2KAlO_2 + H_2O \rightarrow Al_2O_3 + 2KOH$$
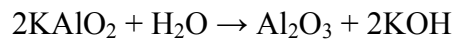
The KOH formed must be in any case completely removed, otherwise can lead to the formation of undesired salts.

1.5.4   Fluorosilicates.

Salts of Mg and Zn are employed, following the reaction:

$$2CaCO_3 + MgSiF_6 \bullet H_2O \rightarrow 2CaF_2 + MgF_2 + 2CO_2 + SiO_2$$
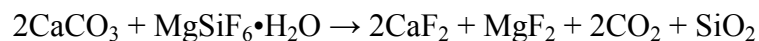
At the same time there is the formation of silica and deposition of fluorite (CaF_2), which is colourless and insoluble in water. The silica should act as hardener, while the substitution of calcite with fluorite should provide a protection from weathering. This product has been widely used since more than 90 years ago, but the results seem to be not completely satisfactory.

1.6   Inorganic consolidants for sandstone

The introduction of silica into crumbling quartz sandstone seems to be the most natural method to replenish lost grain cement. Commercial solutions of silica as sodium or potassium waterglasses (Na_2SiO_3, K_2SiO_3 in water) were developed since 150 years ago. Unfortunately the salts of sodium and potassium which form after the condensation of amorphous SiO_2 tend to effloresce, and the penetration of such water solutions into the stone is not deep enough to obtain a good consolidation. Organic solutions of silane, silicon compounds which condensate to SiO_2, like tetraalkoxysilanes, have a more effective penetration and don't produce any undesirable byproducts.

$$Si(OR_4) + 4H_2O \rightarrow Si(OH)_4 + 4ROH \qquad \text{(hydrolysis)}$$
$$2Si(OH)_4 \rightarrow (OH)_3Si\text{-}O\text{-}Si(OH)_3 \qquad \text{(condensation)}$$
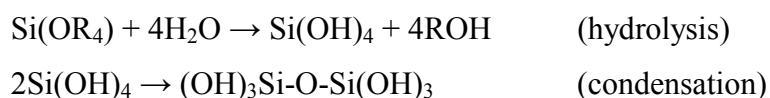
The reaction of alkoxysilane with water must be catalysed and is the basis of the sol-gel method to form amorphous Silica, as will be explained later in this work. The starting reagent may have one or more Si-C bonds, in order to have alchilic or arylic groups directly bonded to the silicon atom. These groups don't participate to the polycondensation and give to the resulting material different properties, such as protection from water and elasticity.

Many different commercial products such as *Steinfestiger OH* (Wacker Chemie GmbH), *Putzfestiger* (Colfirmit Rajasil GmbH) and *Tegovakon V* (Goldschmidt AG – now Degussa AG), are based on the chemistry of alkoxysilane.

1.7   Organic consolidants

1.7.1   Acrylic resins.

Acrylic resins with various formulas, but especially methacrylic resins such as polymethyl methacrylate, also called Plexiglas, have been widely used and experimented for stone consolidation. They are resistant to weathering and to UV radiation, and can be solved in organic solvents to permit their penetration into the stone. Unfortunately penetration deeper than 1 cm can be hardly reached. Stone objects such as statues and small artefacts can be totally impregnated, but this need to be done in a vacuum vat, and can't be applied to masonry.

1.7.2   Epoxy resins.

Epoxy resins are commercially available in a great range of products, with different properties, and are usually applied with the help of a second component called hardener. Despite their effective hardeners properties, epoxy resins are usually too viscose to reach a good penetration depth, and they yellow readily with exposure to UV.

1.7.3   Polyester resins.

Though their good mechanical properties, these resins are not resistant to either alkali or UV radiation. Furthermore their viscosity doesn't allow a good penetration into the stone, and their use is not recommended for restoration.

1.7.4 Polyurethane resins.

Trough polyurethane are widely used as building materials, they don't find many application on restoration. They have good elastic properties as well as good adhesion, and they have been used as protective coaters rather than hardeners.

1.8 Organic-inorganic Hybrid consolidants

This kind of compounds are a compromise between the properties of organic and inorganic consolidants. The final product of such consolidants is usually a composite materials between amorphous silica obtained through the sol-gel process and an organic resin. The resins are usually chosen in the family of the acrylic resins, because of their good mechanical properties and because of the possibility of chemical interaction between the C=O groups of the resin with the OH groups of the silica gel. In this way the affinity of the silica gel with the sandstone can be conjugated to the mechanical properties of the acrylic resin, and a better material can be developed. Some commercial mixtures are since some years available and have been successfully tested on different sandstone samples [7].

1.9 Characterization of the treated stone

A final word must be spent on the characterisation of the effectiveness of the treatment. Many restorers focused on the properties that change with decay and that could give an idea of the extent of the consolidation just after the treatment and after a certain period of time. The main problem is that doesn't exist any standard method for such a measurement and any laboratory works more or less on its own.

A good method was proposed by Wittmann and Prim (1983), [8] and consists in the determination of the biaxial flexural strength of drill core slices by concentrically induced

stress until fracture of the sample. This method provides a bases to asses the quality of a natural stone and the efficiency of a treatment. The measurements on each slice allow us to determine a strength profile of the drill core and to quantify the status of the historical building stone.

In situ measurements are now possible with a new apparatus called DMFS (Drilling Force Measurements System) developed as cooperation between different European countries, which measures the hardness profile of the stone before and after the treatment with a quasi non-destructive analysis by the mean of a special drill whose applied force and penetration speed can be controlled and plotted. This is particularly useful to test the properties of the stone directly *in situ* without any destructive sampling process [9].

AFM (Atomic Force Microscopy) can be a new method to understand the properties of the materials involved on protection and consolidation of stones, and their interactions. That's particularly true for what concerns the characteristics of films formed between the stone's grains and the determination of their properties on a nanometric scale [10, 11].

Chapter 2

Organic-inorganic hybrid materials

2.1   Introduction

Hybrid composite materials come from the idea to combine the properties of organic and inorganic compounds in a unique material. Some of the oldest and most famous organic-inorganic hybrids come from the paint industries, where inorganic pigments such as TiO_2 were suspended in organic mixtures. With the development of the polymer industry the possibility to improve the properties of the polymers with the addition of "fillers" such as minerals, clays and talc, led the research to new hybrids where the inorganic part (mainly silica derivates) were embedded into the polymer. Chemical modification of such fillers, like intercalation and exfoliation of layered silicates, brought indeed to many improvements on polymer's toughness, flammability, rheology, and optical and thermal properties [12, 14].

In the last ten years however, thanks to the increasing popularity of the sol-gel technique, it has been developed a new methodology to produce these hybrids materials, based on the formation *in situ* of the inorganic fillers starting from metallo-organics precursors [15-17]. This system overcomes the limitation due to the thermal lability of polymers and provides the possibility to obtain biphasic materials, where the inorganic and organic phases are mixed at the nanometer to sub-micrometer scales, starting from room temperature.

Because of the dimensions of the phases, these materials are also called "nanocomposites". Nevertheless, the properties of these materials result to be not just the sum of the individual contributions from both phases, but they are those of a new material, where the role of the inner interfaces becomes predominant [18].

The nature of the interaction between the two materials at the interface assumes therefore a central role, and two main classes can be distinguished. In the first class the two

phases are kept together only by non-covalent bonds like hydrogen, *Van der Waals* or ionic bonds. In the second class the two phases are linked by strong chemical bonds through the use of monomers containing both inorganic and organic functions (i.e. organoalkoxysilane).

2.2   Sol-gel process

Although the chemistry of the sol-gel process will be discussed more in detail in the next chapter, a brief introduction about the advantages of this technique in preparing nanocomposites must be done.

The sol-gel process is basically a method to obtain ceramic materials through the condensation in solution of metallo-organics precursors. As we will see, the features of greatest interest in this method are the possibility to work in solution and the formation of inorganic phase at room temperatures. Furthermore the formation of the inorganic network can be controlled in order to obtain the desired product.

2.3   Synthetic strategies

Many different synthetic methods have been developed until now to produce hybrid materials, but probably three different synthetic strategies can be described, which are then applied by the different research groups in many different ways. The choice of the synthetic pathway plays a crucial role on the properties of the resulting material. Different synthetic strategies are chosen if the final product must be a monolith or a film, as well as different methods lead to materials with different properties. Sometimes, as in our case, the choice of the synthetic method is forced by the conditions in which the material is supposed to be used. A natural stone consolidant, in fact, must be applied "*in situ*" under normal atmospheric conditions. This makes it impossible to proceed with a polymerization,

that would require an oxygen free atmosphere. For this reason a pre-formed polymer, usually a methacrylate resin, is chosen and the hybrid material is formed through the combination with a sol-gel process based on tetraethoxysilane hydrolysis. This brings to the formation of a composite of the first class, in which the dimension of the two different phases are of fundamental importance.

The non covalent bonds between the two materials are, in fact, developed at the interface and the contact area result to be higher as the dimension of the domains becomes smaller. For this reason a good composite material must have a good homogeneity and even if a phase separation is always present, the two phases can have domains so small that they can be effectively considered a new material.

2.3.1   Hybrid networks

Hybrid networks can be obtained by running contemporarily the polymerization and the inorganic condensation. If composites with chemical links between the two phases are desired, functionalized precursors or monomers can be used. This leads to an interpenetration of the two networks to a molecular level. (Figure 2.1). The use of organoalkoxysilane for example, functionalized with any organic group that can take part to the organic polymerization, [19] can lead to such a result. On the other hand functionalized polymers [20] can be used (Figure 2.2). In this case an inorganic group introduced on the polymer's backbone, can in a second step participate to the inorganic condensation.
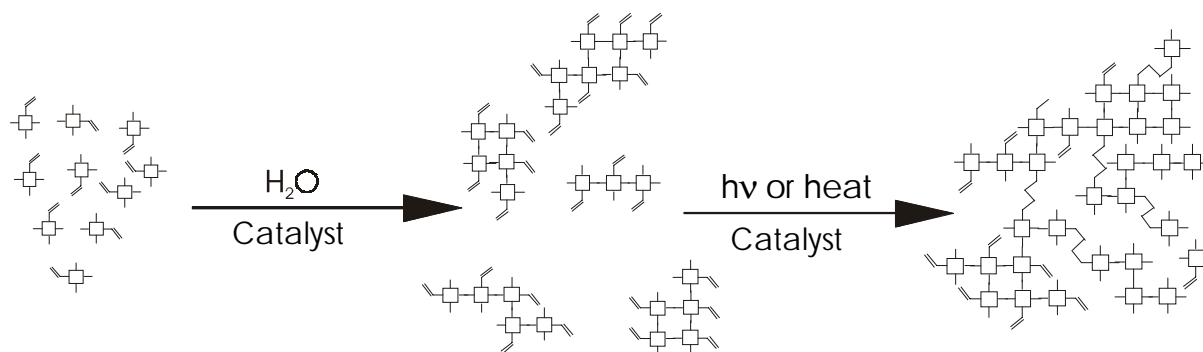
Figure 2.1   Condensation and polymerization of functionalized inorganic precursors.

In some cases the functionalized precursors are introduced as third component and provide the linkage between the phases by being incorporated at the same time in both the growing networks. [21, 22]. The silica-functionalized polymer is moisture sensible, therefore to synthesize and to store it need particulars procedures. Furthermore the gelation process can be too fast to be used for stone hardening purposes because there isn't enough time to let the solution to be adsorbed by the stone.
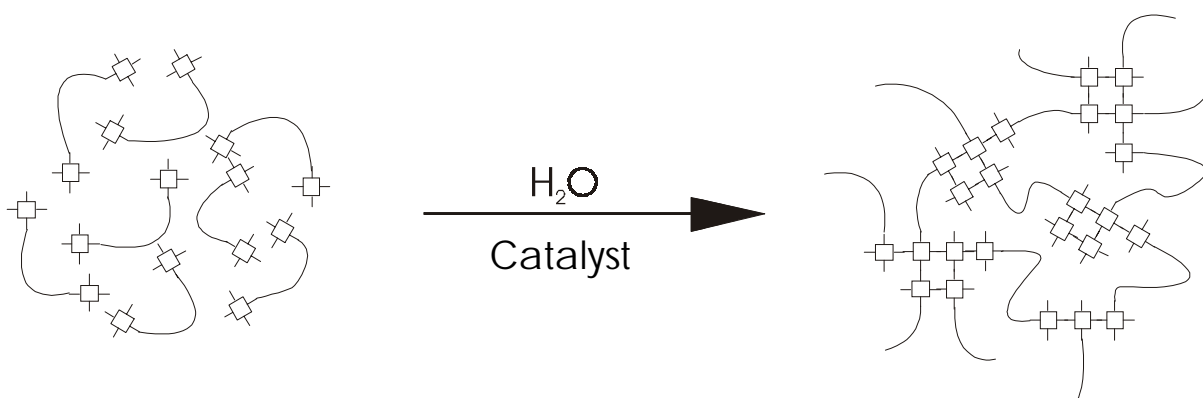
Figure 2. 2   Hydrolytic condensation of functionalized polymers

2.3.2   *In situ* formation or introduction of inorganic species.

The inorganic part of a hybrid material can be introduced or formed within an already formed polymer matrix. After the polymer has been dissolved or swelled with the appropriate solvent, the inorganic part can be introduced as particles or formed *in situ* with a sol-gel process [23, 24].

The incorporation of inorganic particles into a polymer network (Figure 2.3) to improve the properties of the material has been practiced since long time. Problems rise because of the lack of homogeneity of the resulting mixture (the high viscosity leads to agglomeration of particles).

In some cases the particles of particular layered silicate (montmorillonite, bentonite) undergo to a process of intercalation and exfoliation in order to obtain particles of a nanometer size [13].
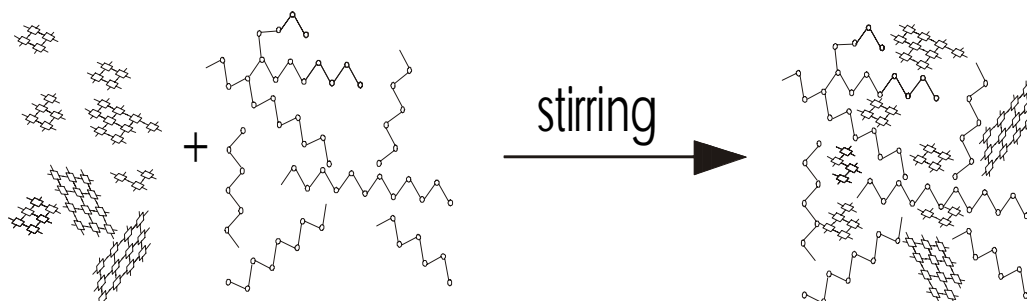
Figure 2. 3   Introduction of inorganic particles.

The formation of the inorganic phase through the sol-gel process, on the other side, is based on the idea that chemical relations between the organic and the forming phase can force the networks to interpenetrate mutually. (Figure 2.4) This method overcomes the problems of homogeneity, but a crucial role is then played by the experimental conditions used. With this method composites of the first class can be easily prepared. If the polymer is functionalized in such a way to participate to the sol-gel process during the formation of the inorganic phase, composites of the second class can be also synthesized. The operational simplicity of this method, anyway, makes it suitable for many different fields of application.

Coltrain et al. [25] Prepared different samples with and without functionalized polyacrilates and found little difference in the properties of the materials. The possibility to obtain materials with comparable properties from unfunctionalized polymers, overcomes the storage problems associated with hydrolytically unstable functionalized polymer. The use of unfunctionalized polymer requires however a greater effort in optimizing the synthetic conditions, in order to obtain homogeneous materials and to minimize the dimensions of the domains of the two phases.

Wei et al. [26] and *Saegusa* [23] proposed an AFM study of such kind of hybrids materials, relating the roughness of the samples to the organic-inorganic phase separation. These works offer a good starting point for our project, where AFM is supposed to become

a comfortable tool to test the compositional and experimental variables of the newly developed materials.
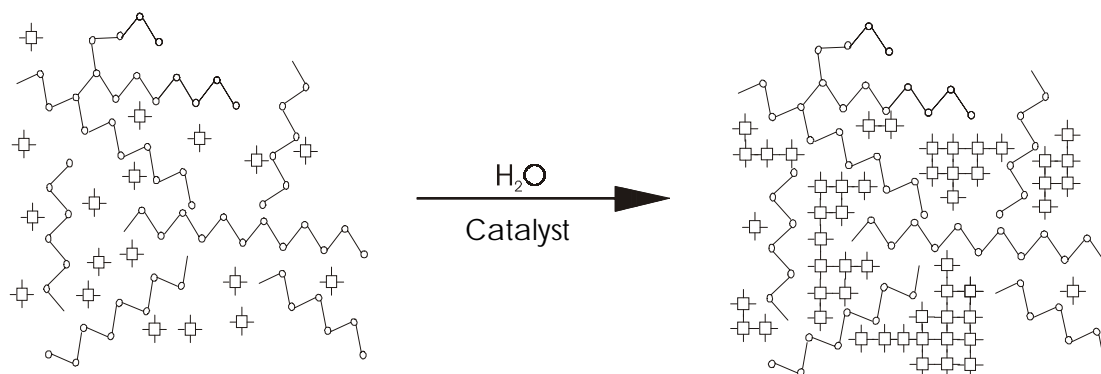
Figure 2. 4   Inorganic sol-gel condensation in an organic network.

2.3.3   Infiltration of previously formed oxide gels with polymerizable organic monomers.

Starting from the opposite direction, a pre-formed gel, which presents an open and porous structure, can be impregnated with organic monomers. (Figure 2.5). The polymerization is then carried *in situ* and initiated by thermal methods or by irradiation. Transparent monoliths of large size with a tunable refractive index can be obtained for optical applications, thanks to the different optical properties of the two materials and the geometry and dimension of the gel pores.

Problems can rise because of the mechanical stresses in the material due to difference of density between the monomer and the polymer, causing cracks and fracture in the monolith. Organic functional molecules can be also introduced, leading to sensors or fluorescent silica micro spheres.
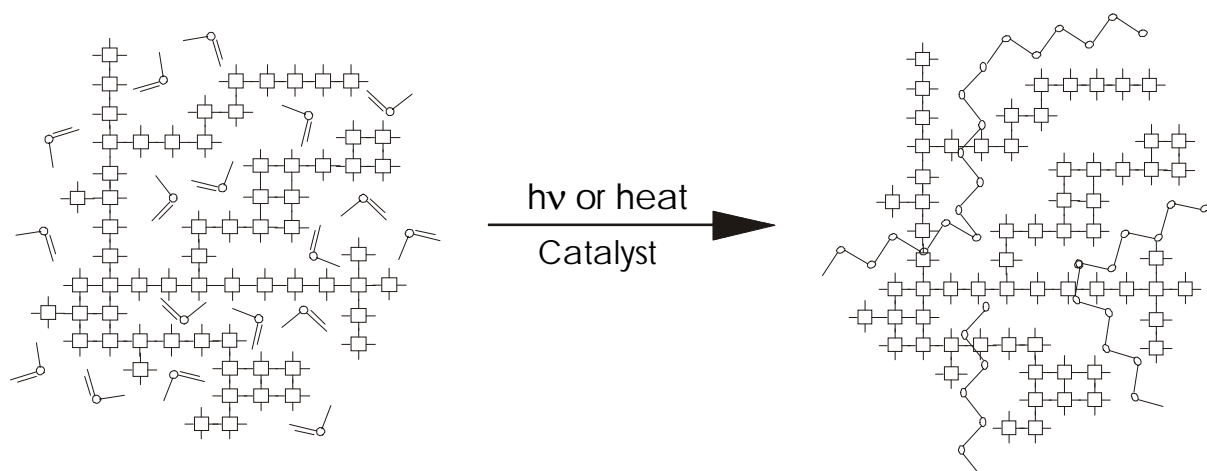
Figure 2. 5   Organic polymerization in an inorganic matrix.

2.4   Applications

Composite hybrids materials find their main application in the polymer industry, were they are used as "modified" polymer with improved qualities. The possibility to have materials with properties that belongs both to organic and inorganic compounds, have been however used for other application, i.e.:

- stone hardener [7, 27, 28]
- scratch and abrasive resistant hard coatings
- special coatings for polymer [29]
- dental resins [30, 31]

Furthermore this kind of materials can be also used in high-technological fields. In fact, even if the two phases of an hybrid material can have very different refractive indexes, the resulting material can be prepared optically transparent. This possibility comes from the small scale length over which phase separation may exist. As a result, these composite materials find application in fields were much more than their mechanical properties can play a role.

Some potential applications [23, 29] for these materials are:

- Electrical and non linear optic materials
- Contact lenses
- Catalyst and porous supports
- Tunable solid-state lasers
- Spacers of liquid Crystalline Display (LCD)

This work will be focused on the application of such materials as natural stone hardener. The experimental conditions, as well as the characterization methods have been chosen to simulate the real operational conditions and to deepen the comprehension of the phenomena occurring when the hardener material builds a film between the grains of the stone.

Chapter 3

The sol-gel method

3.1 Introduction

The sol-gel method [32-35] is a synthetic process that allows the production of ceramic or glassy materials through the formation of a *sol* starting from a solution of precursors, the condensation of the *sol* in a *gel*, and finally the removal of the solvent.

The sol can be produced starting both from organic or inorganic precursors, and the whole process is conducted at room temperature. The peculiar thing is that the solid state can be reached at low temperature starting from a solution, and this fact expands greatly the possibility to create new materials or to improve their properties. It becomes possible, in fact, to synthesize materials under conditions that are not possible in the usual preparation of metal oxides (i.e. Chemical Vapour Deposition) where high temperatures are required.

A sol is defined as a colloidal suspension in a liquid of solid particles, which dimensions, in the range of 1-1000 nm, are small enough to ignore the gravity force. In this way the interaction between the particles are dominated by short-range forces (i.e. Van der Waals and superficial charges).

A gel can be defined as a continuous solid structure that contains a continuous liquid phase. A gel can also be described as a macromolecule formed by all the monomers initially present in solution, which also contains part of the solution itself.

The sol-gel process is characterized by different phases:

- hydrolysis of the precursors
- condensation
- drying
- sintering

Any of these phases has a great influence on the properties of the resulting material and the great number of variables involved makes the control of the whole process still very empirical. Therefore a detailed knowledge of the chemical mechanisms, which permits to control the properties of the final amorphous material at a molecular scale and to synthesize defined structures, is a great challenge for the material scientists.
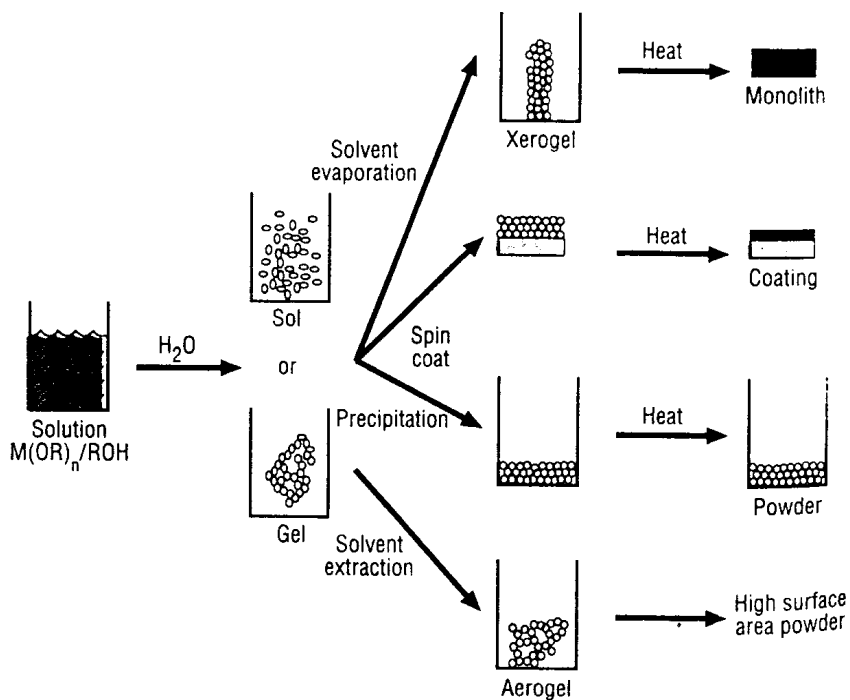
Figure 3. 1   Sol-gel process, different routes possible to synthesize solid materials [32]

3.2   Hydrolysis

The formation of the sol occurs from the hydrolysis reaction of the precursors in solution, which are usually coordination complexes or metallorganic compounds. The class of compounds generally used is the alkoxide class, with the general formula: $M(OR)_n$,

where the number of alkoxide groups n depends on the central atom M. To this class belongs also the compound used in this work: $Si(OEt)_4$ (tetraethoxysilane). [36].

This class of compounds is used because of their reaction with water in the hydrolysis reaction:

$$M(OR)_n + H_2O \rightarrow HO - M(OR)_{n-1} + R - OH$$
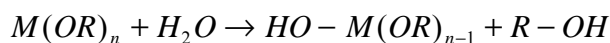
The reaction involves a nucleophilic attack of the water molecule to the central atom M, followed by a proton transfer from H_2O to an alkoxy group –OR, and the exit of an alcohol molecule with a nucleophilic substitution mechanism S_N2.

Often a catalysis is necessary because of the slow reaction rate of the hydrolysis process, as is the case when M = Si. The catalysis can be acid, basic or nucleophilic. The hydrolysis reaction rate is influenced also from the kind of precursors chosen, because of the different steric hindrance of the alkyl groups. The bigger the alkyl group, the more crowded is the nucleus M for a S_N2 reaction and the slower the hydrolysis will be. Furthermore the longer is the chain, the weaker is the inductive effect on the central atom, and the slower will be the substitution reaction.

A great role is also played by the solvent used, because of the difference in polarity, dipole moment and availability of labile protons that influence the rate of the hydrolysis and condensation reactions. Together with the hydrolysis reaction, in an alcoholic solution, two other reaction occur: the reverse reaction, or re-esterification, and the trans-esterification, in which an alcohol molecule displaces an alkoxide group to produce another alcohol molecule.

$$M(OR)_n + R'OH \rightarrow M(OR)_{n-1}(OR') + ROH$$

These reactions follow most probably the same path of the hydrolysis reaction, via a pentacoordinate intermediate. Generally the rate of the transesterification reaction depends on the steric effect of the alcohol molecule, which reacts faster as the alkyl group is less crowded. (-OMe > -OEt > -OPr^i > -OBu^t).

3.2.1 Acid catalysis:

The acid catalysis involves the reversible protonation of the alkoxy group, which assumes a better leaving character. This first step is followed by the nucleophilic substitution by water or by silanol via pentacoordinate intermediate as it's shown in the following reaction scheme where the reaction of tetraalkoxysilane is taken as example:
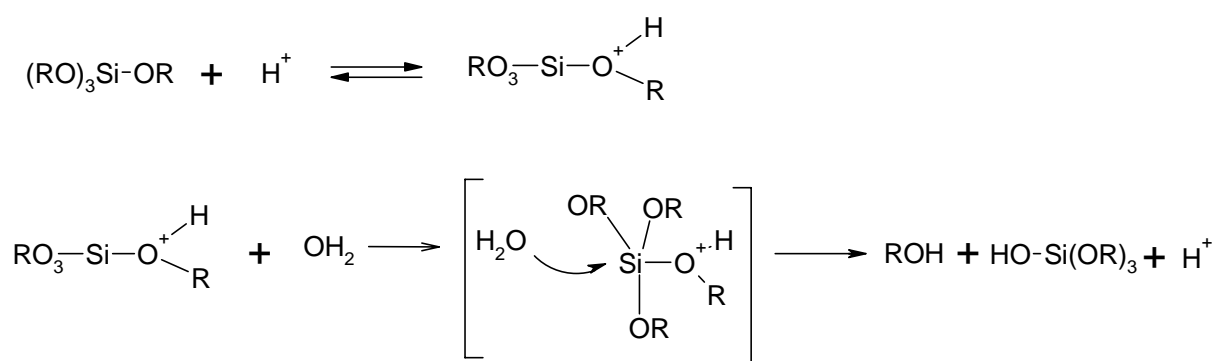
3.2.2 Basic catalysis

A nucleophilic substitution of the alkoxide RO^- by the hydroxide ion, via S_N2 mechanism occurs. The reaction of the alkoxide ion with water leads to the renewal of the catalyst. This mechanism has been questioned since bases could act also as nucleophilic catalyst (see followings). The reaction scheme for base catalysis on tetraalkoxysilane is reported as example:
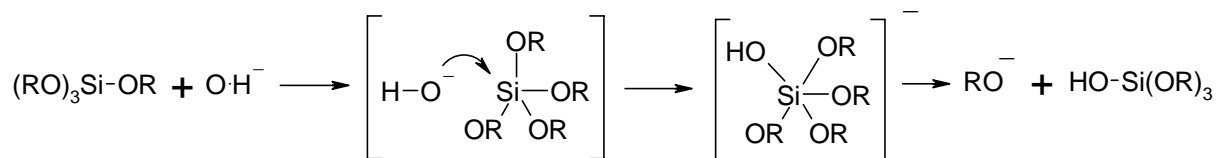
3.2.3 Nucleophilic catalysis

The nucleophilic catalyst (F⁻, N-methylimidazole, N,N-dimethylaminopyridine) forms a pentacoordinate intermediate with the alkoxide compound which is more reactive toward nucleophilic substitution (by water or silanol). This intermediate reacts, via a hexacoordinate transition state with water or silanol to give the hydrolysis or condensation product [33].

$(RO)_3Si-OR$ **+** Nu $\rightleftharpoons$ $\left[\begin{array}{c} Nu \cdots \quad OR \\ \quad | \\ Si ------OR \\ OR \quad OR \end{array} \right]$ $\xrightarrow{}$ ROH **+** $HO\text{-}Si(OR)_3$ **+** Nu

H_2O

Nu = nucleophile
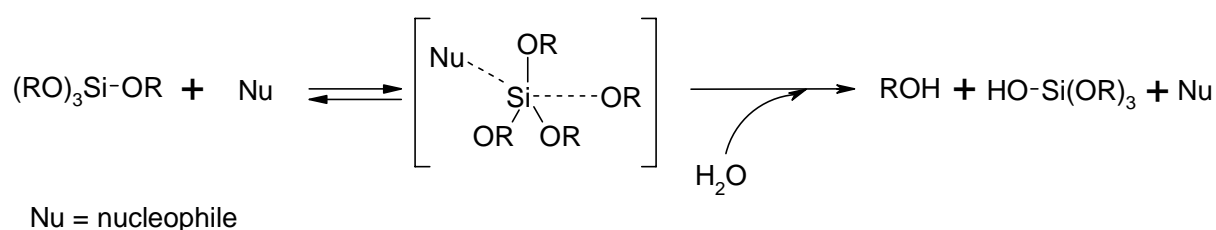
3.3 Condensation

The condensation process takes place as soon as some hydrolyzed precursor molecules are present in the solution and it occurs at the same time and with the same reaction path as the hydrolysis, depending on the quantity of water and catalyst present in solution.

The condensation reaction builds a metal- oxygen- metal bridge, and can follow two different schemes:

Alcoxolation:
$$M - OR + M - OH \rightarrow M - O - M + R - OH$$
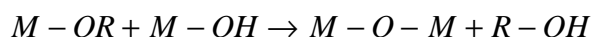
oxolation:
$$M - OH + M - OH \rightarrow M - O - M + H - OH$$
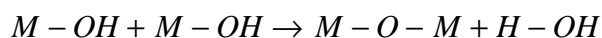
with the removal of the protonated species as either alcohol (alcoxolation) or water (oxolation). This process leads to the formation first of oligomers (Figure 3.2) and then of macromolecules which dimensions and characteristics depend on the reaction conditions used. [37].

The way in which the inorganic polymer grows depend also on the functionality f of the precursor, or on the number of oxygen bridges that can be bound to the central atom. Silicon has for example a functionality $f = 4$, but it can be decreased by chemical modification (i.e. β-diketones, carboxylic acids or other chelating ligands). When the functionality is more than 2, the chain will grow with crosslinks to build a three dimensional network.
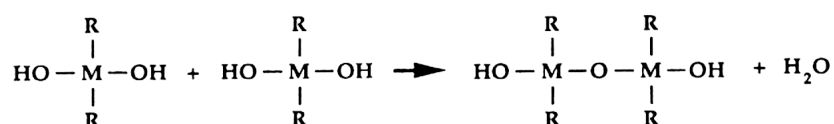
Chain
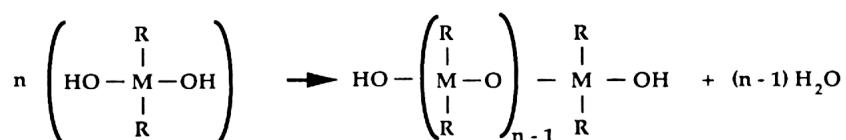
Ring
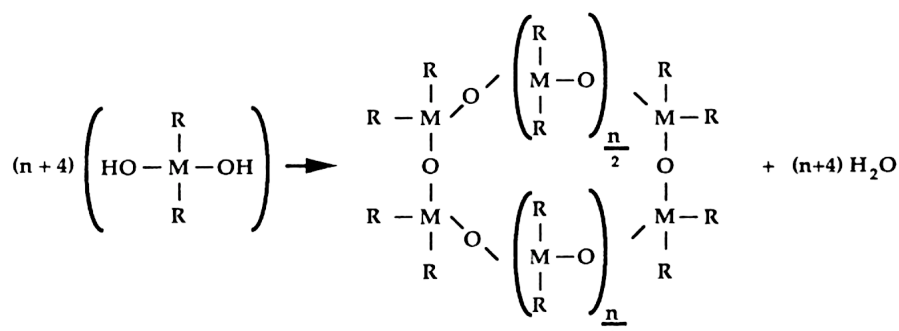
Figure 3.2 **Possible condensation pathways to form different oligomer structures for a precursor with functionality $f = 2$**

3.4 Drying

The drying process is the first step from the gel to the solid material, and it occurs with a contraction of the gel's volume and a stiffening of its structure. In this phase of the process, in fact, the solvent is expelled from the gel network and many of the structural characteristics and properties of the resulting solid material (i.e. density, elastic properties) depend on the evolution of the system also in this phase.

If we imagine a gel as a network that include a liquid phase (Figure 3.3), it's obvious that there is a high interfacial area with a great free energy associated. The decreasing of this energy is the driving force that leads the system to the shrinkage phenomenon.

The evaporation of the liquid from the gel surface, in fact, increases the vapour-solid interface, which has a even greater energy. For this reason the liquid flows from the bulk of the gel to the surface, to cover the dried surface. Because of the evaporation the liquid can't cover the whole surface without the creation of a meniscus on the pore surface. The capillary force exerted by the liquid causes the contraction of the solid phase, until the radius of the meniscus is equal to the radius of the pore. At this stage the shrinkage proceeds at a constant rate, and the contraction of the solid phase is equivalent to the volume of the evaporated liquid.

After this point the evaporation of the liquid continues moving the liquid-vapour interface towards the bulk of the solid phase leaving a dry solid. This contraction result to be irreversible, because of the further condensation of the unreacted hydroxyl or alkoxy groups that proceeds during the shrinkage process any time that two groups approach enough to react and form a new Si-O-Si bridge.

The drying of the gel produces anyway a pressure gradient in the liquid phase, which leads to differential shrinkage of the network. If the external part shrinks faster than the internal one, tensile stresses arise that tend to fracture the network. The formation of cracks is energetically favourable because at either side of the crack the material can contract more freely. To avoid this phenomenon, a slow evaporation rate of the solvent is

required. The aging of the gel in its own pore liquid reduces also the risk of fractures, because it helps to strengthen the network, especially if it's still in presence of water and catalyst.

a) Initial condition

Liquid / vapor meniscus flat

Pore liquid

Solid phase

b) Constant rate period

Evaporation

Shrinkage

c) Falling rate period

Empty pores

Minimum radius of curvature
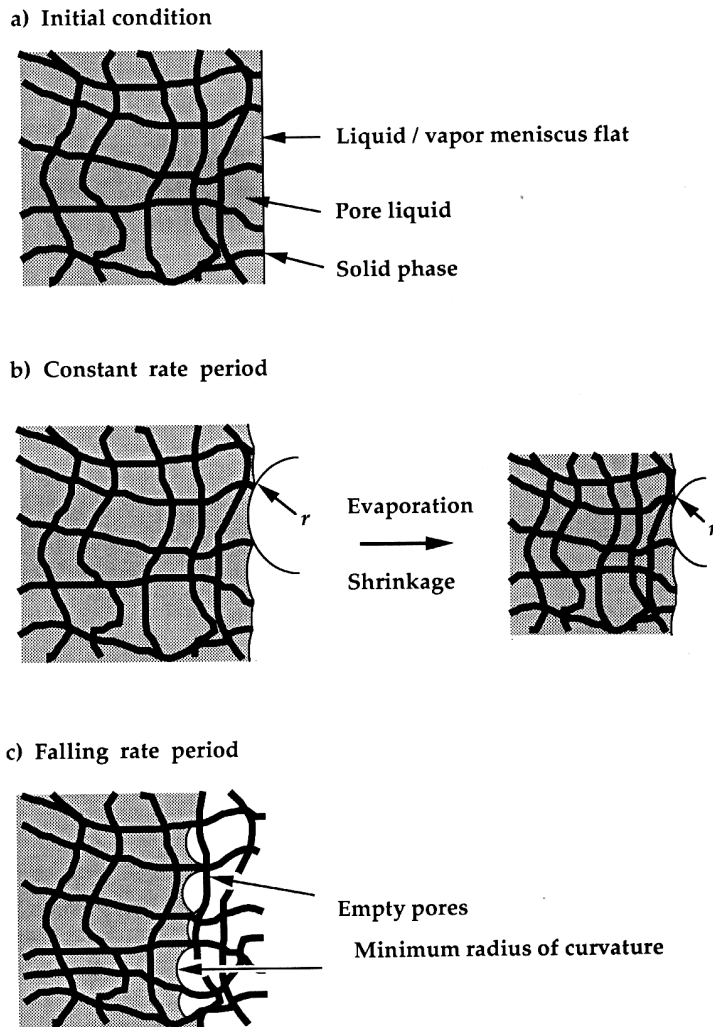
Figure 3. 3   **Drying process. a) the network deforms so easily that little stress is needed to keep it submerged. b) as the network stiffens the pressure increase and the radius of the pores r decrease until the radius of the pore is equal to the radius of the meniscus. c) after this point the liquid recedes into the gel. [32]**

3.5 Consolidation and Sintering

The last part of the sol-gel process involves the densification of the dry gel structure to give a glassy material or polycrystalline solid. This evolution of the system occurs under high temperature, and time and temperature of the thermal treatment can influence again the characteristics of the resulting solid material. The transformation involved in this phase of the process are:

- capillary shrinkage
- condensation
- structural relaxation
- viscous sintering

The fast evaporation of water and other organics during the thermal treatment causes often the presence of cracks and other structural imperfections. The weight loss and the shrinkage are in this phase not linear dependent and behave differently depending on the temperature, as it's reported on the graph below (Figure 3.4).
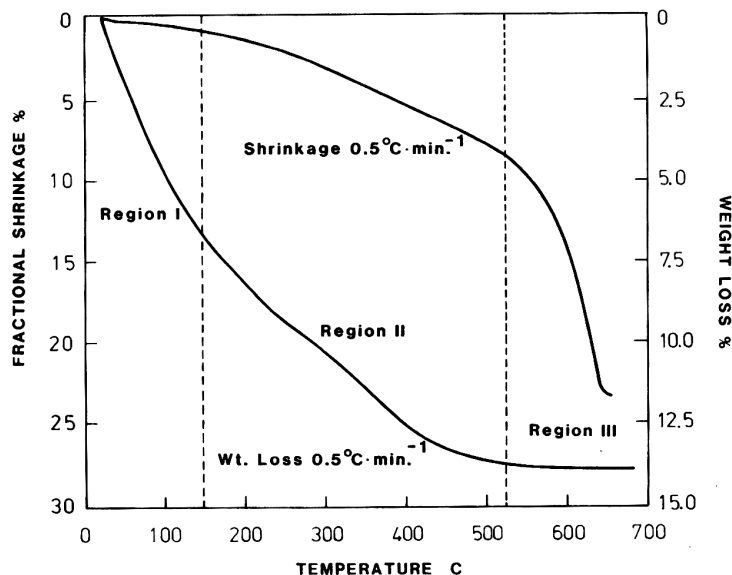
Figure 3. 4 **Shrinkage and weight loss in a gel during the thermal treatment, for a heating rate of 0,5 °C min^{-1}. [32]**

In the first region a small contraction is observed for a great weight loss. The weight loss is due to the evaporation of the water and alcohol still present inside the gel network. The small contraction is due to the increase of the surface energy owing to the desorption of the liquids. In the second region the contraction is proportional to the weight loss. The weight loss is due to the water formed as by-products of the condensation and to the removal of organics, while the contraction is due to a further condensation and to the structural relaxation due to the temperature. In the third region there is contraction without further weight loss, because of the viscous sintering in which the material moves by viscous flow or diffusion in such a way to eliminate porosity. The sintering of gels, because of their great interfacial area, can be conducted at temperatures exceptionally low compared to those used for the sintering of ceramic materials.

3.6   Film deposition – dip coating

Films of glassy or ceramic materials on hard substrates are easily deposited using the sol-gel technique. Three methods are usually employed : dip coating, spin coating and spraying. The difference between them lies mainly in the different technical arrangement used to deposit a fluid layer of the solution of the precursor on the substrate's surface. The technique chosen in this work, because of its operational simplicity is the dip coating technique, which will be further described on this paragraph.

The dip coating process can be divided theoretically in five phases as it's shown in Figure 3.5:
- immersion
- start-up
- deposition
- drainage
- evaporation

These phases can also be mixed, as it happens with volatile solvents like alcohols or THF, where the evaporation process starts directly after the start-up phase.
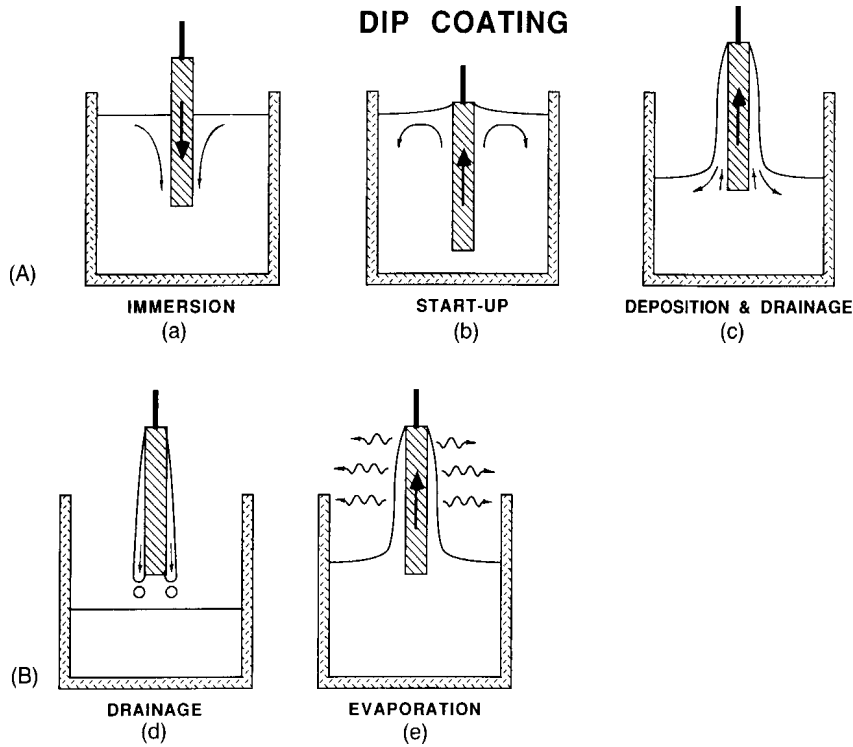
Figure 3. 5   Sol-gel dip-coating process [32]

If the viscosity of the liquid (η) and the withdrawal speed of the substrate (U) are high enough to lower the curvature of the meniscus, the thickness of the deposited film (h) is that one that balance the viscous friction (proportional to $\eta U/h$) and the gravity force (ρgh), following the formula:

$$h = c(\eta U/\rho g)^{1/2}$$

where c is a constant which depend on the liquid used.

On the other side, when the withdrawal speed of the substrate and the viscosity are not high enough, as often happens under the experimental conditions usually used in sol-

gel processes, the balance depends on the friction and on the liquid-vapour surface tension (σ_{LV}) as in the Landau-Levich relation:

$$h = 0.94(\eta U/\sigma_{LV})^{1/6}(\eta U/\rho g)^{1/2}$$

In both the relations anyway, the thickness of the film, when all other parameters are constant, depend on the withdrawal speed. The faster the substrate speed, the thicker the film and the greater the overlap between the deposition and drying stages.
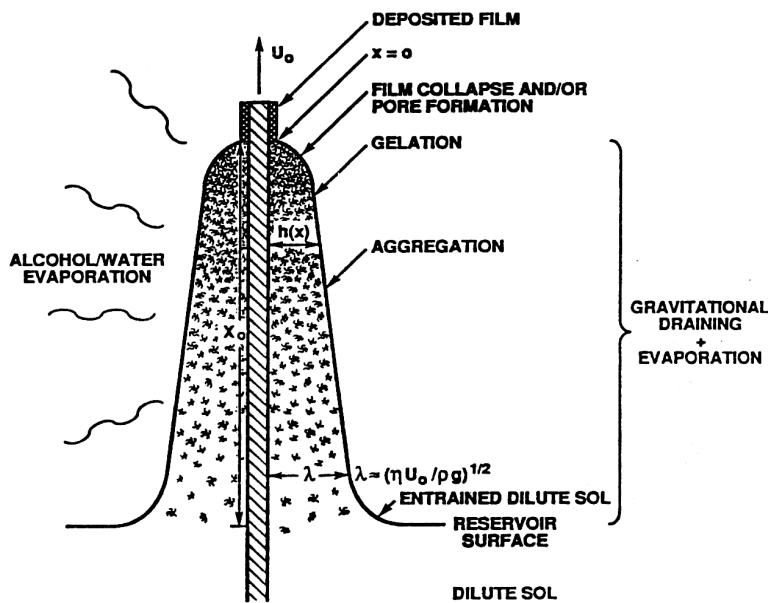
Figure 3. 6   Evolution of the system during draining and evaporation phases [32]

The structure of the forming film is influenced also by the precursor used and by the evolution of the system based on the drying solution. In figure 3.6, the evolution of the system formed during the dip coating deposition is shown. The dilute solution is concentrated at the surface of the substrate owing to the drainage of the solvent and to evaporation phenomena. The concentration of the species in solution increases greatly, approaching the oligomers and the cluster eventually present and promoting a rapid condensation of the solution into a gel.

The gelation-point is reached when the forming network prevents the solution from flowing down, including it into the gel film formed on the surface of the substrate. The further evaporation of the solvent trapped into the gel will cause eventually porosity or structural defects, as cracks and fractures.

During the extraction phase there is a competition between the evaporation of the solvent, which causes a shrinkage of the film, and the condensation process, which strengthens the structure of the network and opposes to this shrinkage. This competition is caused by the overlapping of the deposition and evaporation phases, and permit a modulation of the film structure controlling the withdrawal speed or the atmosphere in which the film is extracted.

Good films must be homogenous, free from structural defects and of uniform thickness. The experimental parameters which can influence the film structure are:

- starting solution (precursors, solvent used, catalyst, amount of water)
- temperature and aging of the solution
- withdrawal speed
- substrate

Possible defects of the films are: the presence of structural defects (i.e. cracks and fractures) and the presence of particles as well as not homogeneous distribution of the material on the substrate.

The particles come from a contamination of the solution by external agents or can form in solution as effect of the sol-gel process. The presence of particles can affect the homogeneity of the film and can be eliminated through filtration or centrifugation of the solution.

The presence of structural defects can be determined by many different factors. Often cracks grow in correspondence of particles or other impurities. The formation of cracks depend also on the thickness of the film. There is in fact a critical thickness, beyond which the film will crack as consequence of the differential shrinkage between the interface of the film with air and with the substrate. The presence of a particle can locally increase the amount of material and cause the formation of a crack.

Another defect can be the lack of homogeneity of the film, which is due to phase separation during the condensation process. In this case different areas of the film show different properties and characteristics, making the film useless for every practical purpose.

For any application and analysis it must be known that at the edges of the substrate there is always a "perturbed" area of few millimetres where the thickness of the film is not homogenous at all.

3.7   Applications

The technological applications of the sol-gel technique range in a very wide field, because of the versatility and simplicity of the method. The possible applications derive from the various shapes that can be obtained from the gel state and from the compositional and microstructural control of the process, combined with the low processing temperature.

Compared to other techniques the sol-gel method has the advantages of a good control of the starting material and of the processing parameters, a high purity of the row materials, the low temperature of the process and the homogeneity of the product due to the possibility to control the starting solution. Disadvantages are, on the other side, the high cost of the raw materials, that makes it suitable only for high quality products, the large shrinkage during processing, long processing time and the presence of residual organics in the final product.

Different shapes of the products determine different applications: dried gel without cracks larger than 1 mm are called monoliths and are used for optical components, transparent superinsulators, and special glasses [38]. Powders, grains and spheres are used as catalyst, dyes, and abrasives. Fibers drawn directly from viscous sols are used for reinforcements or fabrications of textiles. Porous gels and membranes are used as filters and as chromatographic supports. Finally films are used for protection coatings, sensors and optical materials, but their use spreads in many different fields like for example the protection and restoration of natural stones that is the subject of this work.

Chapter 4

Methods and instrumentation

4.1   Atomic Force Microscopy (AFM)

Atomic Force Microscopy is a microscopy technique substantially different from all the others based on beams transmission or reflection, and composed by beam sources, lenses and detectors. In AFM, in fact, and more generally in all the techniques of the Scanning Probe Microscopy (SPM) family, the images are generated by a computer from a matrix of data obtained point by point from the interaction of a tip with the surface. (Figure 4.1). The kind of interaction determines the specific technique of the SPM family [39-44].

In particular in Atomic Force Microscopy the force involved is the mere attraction or repulsion force between atoms at a very short distance. The use of other kinds of interactions characterizes different techniques, i.e. Scanning Tunneling Microscopy [40, 65] (STM), Magnetic Force Microscopy [45-47] (MFM) and Electric Force Microscopy (EFM) [48,49]. Sophisticated detection system are capable to monitor the response of the probe to particular characteristic of the surface, such as elasticity, stiffness and friction. These techniques produce, beside the usual topography of the surface, a map of the relative distribution of the specific properties. Lateral Force Microscopy [50] (LFM) maps relative differences in friction (typically in contact mode), Force Modulation AFM [51-53] maps relative differences in surface stiffness and elasticity (contact mode), and Phase Imaging [54-57] maps phase shifts in cantilever oscillation which can be related to changes in materials properties, such as adhesion and visco-elasticity (tapping mode).

The mean feature of SPM techniques is the possibility, depending on the probe used and on the system, to scan up to the nanometric or even atomic range [58,59], without the requirement of vacuum and without any particular sample preparation. AFM in particular can be used on any surface regardless to the conductivity of the material scanned and the samples can be analyzed even in fluid [60, 61]. This last possibility results particularly

useful for biological application [62]. By contrast, many electron microscopes, having the closest resolving power of any other class of instrument, require vacuum conditions and metal coating of samples.

Furthermore AFM images, as they are computer elaboration of data points, can be rendered in 3D representation or cut to give cross sections of the surface. Once the system is calibrated with a calibration samples whose features are well known, distances and depths can be measured with a sensibility of 10^{-10} m . The maximal extension of the scanned area is limited by the excursion of the piezo that controls the movements of the tip on the surface. Usually x-y axis have a range of 100-200 μm, while z axis has a maximum range of 5 to 10 μm. That makes AFM particularly suitable for the analysis of rather flat surfaces, like films of coating materials, polymers, ceramics and glasses.
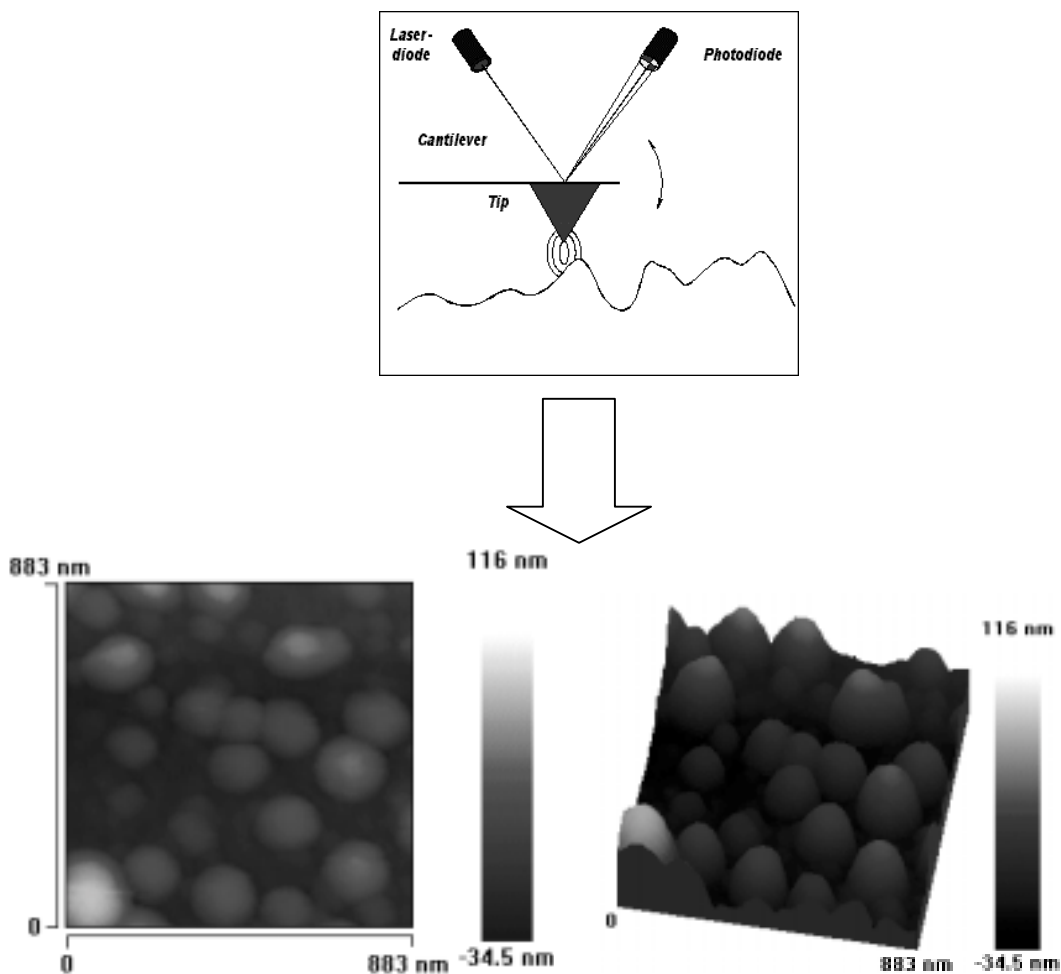
Figure 4. 1   Image generation principle in Atomic Force Microscopy (AFM)

4.1.1 Measurements Principles

The main aim of a SPM system is to scan a sharp probe across a surface and to collect the data regarding the interaction between them. In Atomic Force Microscopy the data collected are about the forces exerted at a very short distance, and they give information about the topography of the sample's surface.

Practically, the force is controlled to maintain constant a user-specified setpoint level, through the use of a electronic feedback loop. Although the meaning of the setpoint depends on the "mode" used to obtain the images, the feedback loop performs essentially the same function, that is, to vary the position of the tip in the z-axis in order to maintain constant the force (and therefore the distance) between the tip and the surface. The three different "scan-mode" of AFM are: contact mode, non-contact mode and tapping mode, as will be explained more in details on the following paragraphs.

The variation of the relative position of the tip respect to the sample is performed by the system through the use of a piezo-electric element, and brings the deflection (and so the force) of the cantilever that holds the tip back to that set by the user. The efficiency of the feedback loop is set by two parameters called proportional and integral gain, controlled also by the user depending on the roughness of the surface and on the scan rate, that is, on the speed at which the tip is scanned across the surface.

When acquiring images, the vertical position assumed by the scanner at each (x,y) data point in order to maintain constant the deflection (or amplitude of oscillation) defined by the setpoint, is stored by the computer and used to form the topographic image of the sample surface.

In principle the tip could be also roughly scanned upon the surface without any feedback loop system and the mere deflection of the cantilever due to the topography of the surface could be reported to build an image of the surface itself. This mechanism is in fact still applied when scanning at atomic level, but can no more be applied when the features of the surface exceed the possibility of deflection of the cantilever.

The use of the feedback loop prevents then the breaking of the tip or the damaging of the surface and expands the possibility of the instrument on the z-axis. Furthermore the deflection of the cantilever is maintained constant (as fast as the system reacts to the

variations) like the force exerted by the tip upon the surface. This prevent the deformation of the sample and the formation of artifacts on the AFM picture.

4.1.2 Tip-sample interaction

The comprehension of the interactions occurring between the tip and the sample are of great importance for a correct interpretation of the AFM images. These interactions occur at a very short distance (10^{-5} - 10^{-10} m) and concern the very small area of the surface "touched" by the tip. In the ideal case of a one-atom tip, just few atoms of the surface are involved. The forces involved are here reported in the same order in which they are met by the tip during the approaching process [63].

Fluid Film Damping (~ 10 μm)

The first boundary is encountered only if the Tapping Mode is used. The film damping phenomenon, in fact, is exclusive to oscillating probes because it is due to the air film which is developed when the oscillating probe comes at ca. 10 microns over the sample surface. At this distance the air squeezed between the probe and the surface during each oscillation of the probe, creates a dampening effect which may lead to false engagement. The phenomenon disappears when this boundary is passed.

Electrostatic Forces (0.1-1 μm)

The next boundary encountered is the electrostatic force zone beginning at 0.100—1.00 microns. According to the material, electrostatic forces may be either attractive or repulsive. Moreover different kinds of materials present different electrostatic properties; i.e. low-conductivity materials like silicon nitride exhibit strong electrostatic forces, while conductors exhibit smaller electrostatic properties. The distribution of the electrostatic forces over the sample's surface can be itself imaged using Electric Force Microscopy (EFM).

Fluid Surface Tension (10-200 nm)

The presence of a thin water layer on the surface of the sample results in the presence of surface tension effects. The attractive force exerted can pull the tip down toward the sample surface strong enough to cause the indentation of the tip into the material. The effect can begin at 10-200 nm above the surface, depending on the thickness of the adsorbed fluid layer. Sometimes both the tip and the sample are entirely immersed in fluid to avoid this effect. This problem can be solved also by the use of the tapping mode.

Van Der Waals Forces (Angstrom level)

Van Der Waals forces are present when the tip is only few Angstroms above the surface. These forces cause a weak attraction between atoms in the tip and the sample, which can be detected by the AFM electronics. These forces are used to obtain the images in the "non contact" mode. At this point no pressure is exerted by the tip on the surface and no damage can be caused at the sample.

Coulombic Forces (Fraction of Angstrom)

When the atoms of the tip encounter the coulombic forces of the atoms of the surface, the tip and the sample are said to "contact". The coulombic repulsion force between the electron shells from tip and sample prevents further intrusion by one material into the other. At this point is usually set the force in the contact mode AFM. Pressure exerted beyond this level leads to mechanical distortion of one or both materials, and the tip or the surface may be damaged.

4.1.3 Contact mode AFM

Contact mode AFM is the simplest way to perform AFM and operates following the principles explained above. The tip is scanned across the surface at a constant force, almost in contact with the sample. The main force involved here is coulombic repulsion and it is calculated from the Hooke's law F= -*kx* where F is the force exerted by the tip on the surface, *k* is the cantilever spring constant and *x* is the cantilever deflection. The force is usually maintained constant in a range from 10^{-7} N to 10^{-11} N.

Operation can take place in ambient and in liquid environment and the main advantage of this technique is the fact that the tip contacts the surface through the adsorbed fluid layer eventually present. That means that fluids droplets adsorbed on the surface can be neglected, making the sample preparation much easier. Contact mode AFM is particularly suitable for imaging rough surfaces, but there is a considerable risk to damage soft samples by scratching. Even if the force involved is so small, in fact, it must not be forgotten that it is exerted on a extremely small surface, and the resulting pressure can be high enough to damage both the tip and the surface.
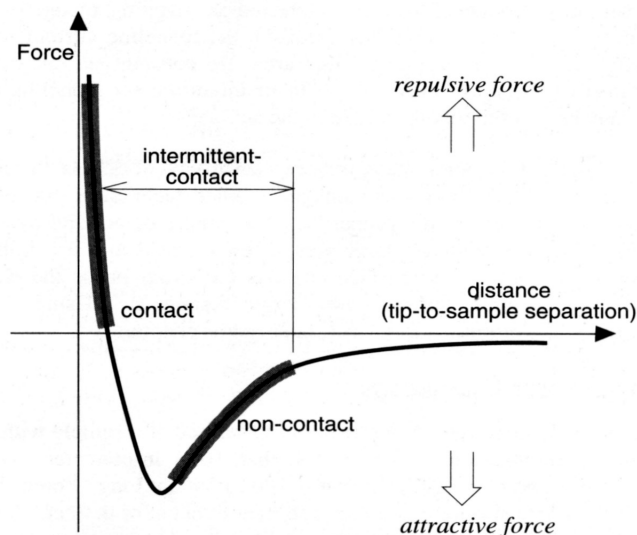
Figure 4. 2   Plot of the force versus the tip-to-sample distance
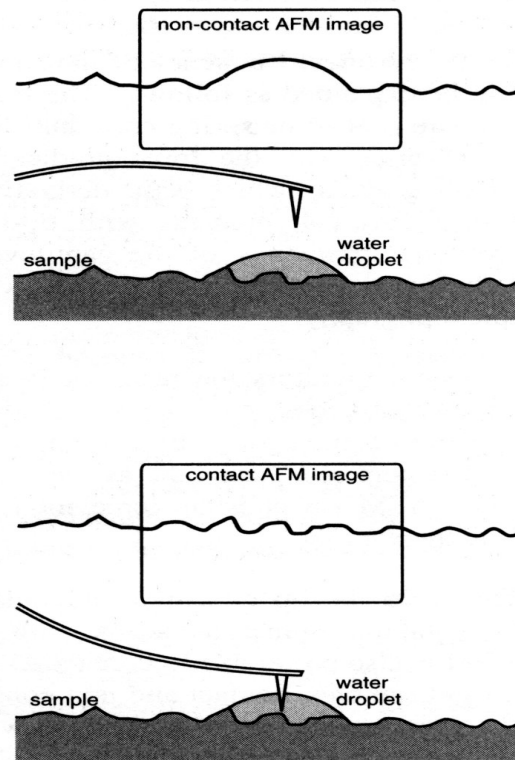
Figure 4. 3   Artifacts generated by water droplets in the non-contact mode AFM [64]

4.1.4 Non-contact mode AFM

In non-contact mode AFM the tip oscillates above the surface and feels the attractive effect of the Van Der Waals forces which extend from 1 nm to 10 nm above the adsorbed fluid layer and by other long range forces (Figure 4.2). The cantilever is oscillated at a frequency which is slightly above the cantilever resonance frequency, typically with an amplitude of few nanometers (<10nm). The cantilever resonant frequency is decreased by long range forces and that causes the amplitude of the oscillation to decrease. The feedback loop maintains constant the AC signal generated by the cantilever oscillation during the scanning of the surface and this generates the data point necessary to build the topographic image of the surface. The main problem of this method is that the tip is scanned over the fluid layer adsorbed on the surface, and droplets of liquid can hide the

real topography of the sample and generate artifacts (Figure 4.3). A great advantage is anyway the possibility to scan soft surfaces without any damage.

4.1.5 Tapping mode AFM

Tapping mode AFM resume practically the advantages of contact and non contact mode. The cantilever is oscillated at or near its resonance frequency, with an amplitude ranging from 20 nm to 100 nm. The amplitude of oscillation is larger than the one applied in the non-contact method and the tip lightly touches the surface at the bottom of its swing. In this way the tip is in contact with the surface at every period of oscillation, passing through the adsorbed fluid layer, but it breaks free in air at the end of every swing, without getting stuck.

The amplitude of the cantilever oscillation is reduced when the tip contacts the surface and it results smaller than the free amplitude of the cantilever before the approaching. (Figure 4.4). The feedback loop maintains a constant oscillation amplitude by maintaining a constant RMS of the oscillation signal acquired by the split photodiode detector, and the vertical movements of the scanner generates the topographic image of the surface. A constant oscillation anplitude guarantees a constant tip-sample interaction during scanning.

Tapping mode AFM can take place both in air and under liquid and is particularly suitable for soft or fragile samples, because every lateral force of the tip on the surface is avoided by the tapping action.
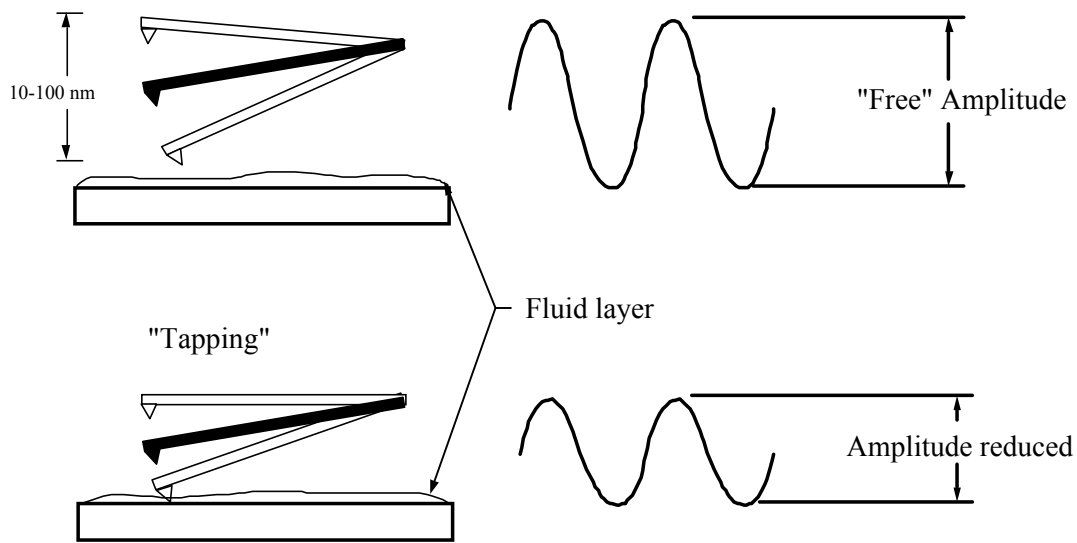
Figure 4. 4   Tapping mode AFM- cantilever oscillation amplitude response to the tip-surface distance [64].

4.1.6 Artifacts

Artifacts are defects in the AFM images due to relative geometry of the tip-surface system. In practice the topography reported on the image doesn't correspond exactly to the real topography of the sample. This phenomenon can be due to many different factor, that must be well known by the SPM user. Some of the errors are due to the geometry of the sample, and cannot be overcome, as they are a limit of the system, some others are due to defects of the tip, and are easily resolved by using a new tip or a better one.

The presence of artifacts on AFM pictures is anyway the main source of errors in the interpretation of the data and represent one of the limit of the system (Figure 4.5).
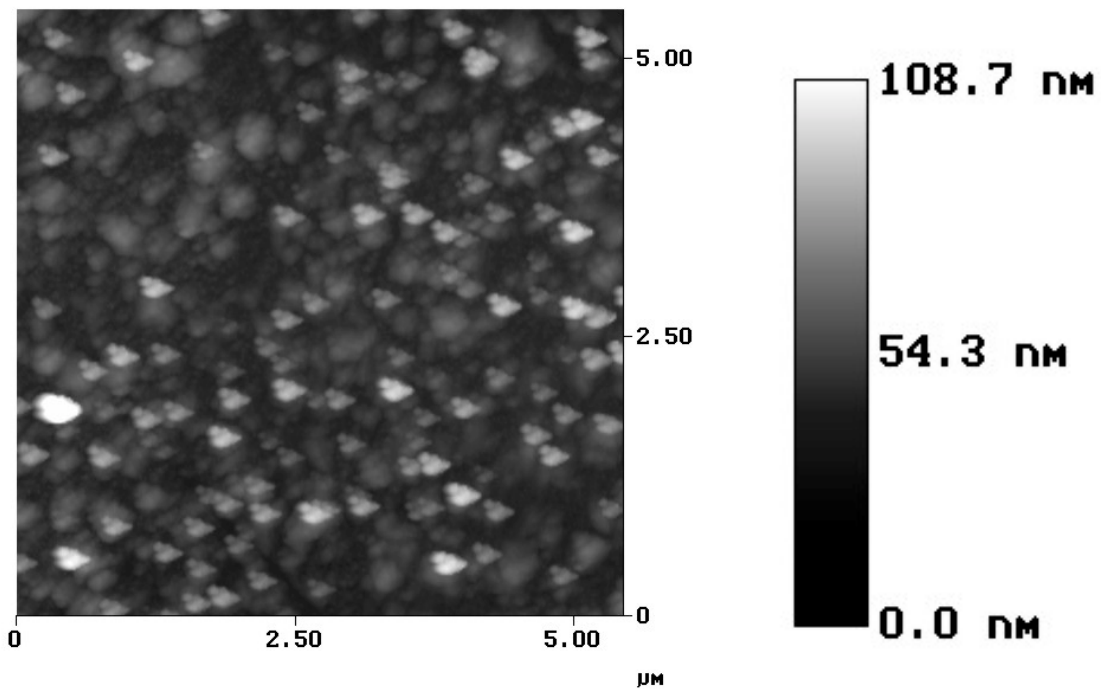
Figure 4. 5 **Example of artifacts due to contaminated tip. All the features of the surface assume the same image because of a particle stuck on the tip, whose shape is displayed instead.**

A deep fissure is the first obvious surface limitation and is represented in Figure 4.6. In this case, the tip is not long enough, or thin enough, to reach to the bottom of a recess. Although the edges would be imaged here, each square recess would be misrepresented as a wedged trench. In Practice the tip will scan only what it can reach and the topography at the bottom of the fissure will be lost.

Furthermore the tip is "blind" to angles steeper than itself. This means that a sheer wall, with an angle steeper than that of the tip, will be represented as a slope of the same aspect of the tip itself. Although this limitation is overcome slightly by using a tip with a higher aspect ratio, thus presenting a more vertical aspect to the sample's wall, this only works in the leading edge direction. The trailing edge of the tip presents an angled aspect to the sample's wall and cannot detect any angles steeper than itself.
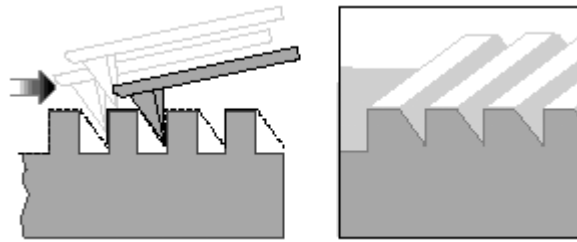
Figure 4. 6   Artifacts can be due to recess on the surface too deep to be reached by the tip [64].

Another limitation that often occurs is undercut features (Figure 4.7). These are voids created by overhanging material, which cannot be accessed by the tip. This is a general limitation of all SPM systems and cannot be overcome. The AFM user must be aware of this possibility during the interpretation of images. Often a great help is given by the use of another microscopy technique as SEM, to compare the information obtained with the two methods.
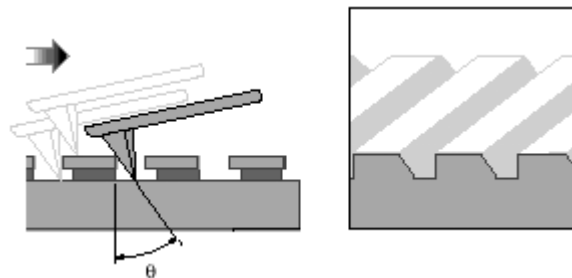
Figure 4. 7   Artifacts can be due to undercuts features present on the surface [64].

Other problems are directly due to the tip itself, because the tip's geometry—the quality of its sharpness, size, and shape—has a direct influence on the accuracy of the image data..

Consider a SPM tip having a radius R as it encounters a series of parallel, rod-shaped features as represented in Figure 4.8. The scanning tip will resolve separation between the rods to varying degrees, depending on the value of R. The tip's sensibility to the separation between the features increases as R decreases. Therefore it's clear that the ability of a tip to resolve feature separation is tied to radius. For this reason a tip with a smaller aspect ratio (ratio of length to width) or "sharpness" confers an advantage in

resolving features than a tip with larger radius R. However there will be always a limit to the accuracy of the image acquired, depending on the kind of tip used.
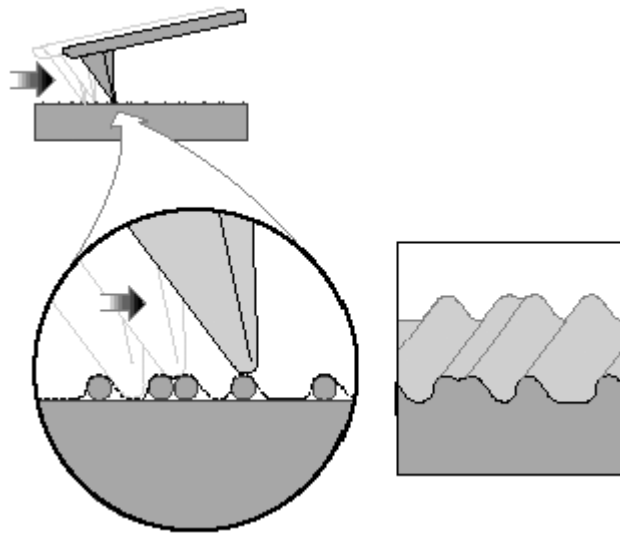
Figure 4. 8   Feature of the image can be resolved depending on the aspect ratio of the tip. [64].

Another limitation is incurred when a tip becomes contaminated by debris on the sample surface (Figure 4.9) and contaminated tips impose their own geometry to the images of the surface. The tip is kept in fact by the debris at a set distance from the surface and this creates a biased profile because the tip shape is scanned by the features of the surface rather than the contrary.

Generally the easiest way to overcome this problem is to use a new tip. Not so easy is to recognize the problem when it occurs, while usually the topography of the surface scanned is unknown. A typical imagine affected by this artifact is shown in figure 4.4. because of the contamination of the tip all the features in the imagine seem to have the same shape. In reality that is the shape of the contaminated tip.

One way of getting around limitations imposed by tip size and geometry is to first scan a surface having a precisely known geometry, then extrapolate backward to evaluate the true geometry of the tip. Afterward, it is possible to scan surfaces of unknown geometry while making compensations for the tip's true geometry to obtain more accurate

images. Generally, this method is applied to increase accuracy of wall angles and distances between upright features.
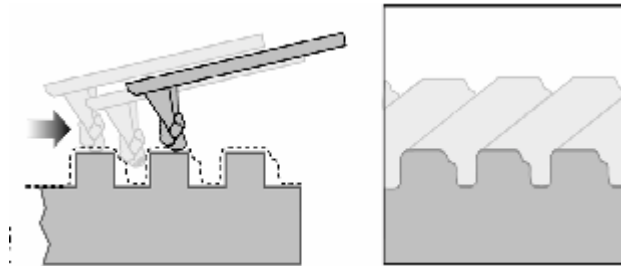
Figure 4. 9   Artifacts due to debris present on the tip [64].

4.1.7 Hardware

All SPM systems, regardless of type, have four basic hardware elements in common. These elements include: tip, scanner, detection mechanism and feedback electronics [63].

Tips (Probes)

The term "tip" is used to indicate the elements that compose the part directly interacting with the sample. Properly speaking, the tip is the sharp part of the probe mounted on a cantilever. The cantilever provides a support for the tip and is deflected by pressure upon the tip. By monitoring how the cantilever is deflected, the tip's travel over surface features is interpreted, then rendered into an electronic image.

Most contact AFM and Tapping Mode tips are fabricated from silicon-based materials, (Figure 4.10) largely because micro-fabrication of silicon has been extensively developed in the microelectronics field. These tips are made in various lengths and thickness, depending upon a desired spring constant. Probes having a lower spring constant exert smaller forces against samples and are, therefore, less intrusive. Unfortunately, probes having lower spring constants are more subject to entrapment by surface tension

forces on the sample surfaces. Stiffer probes are more easily pulled away from the sample surface, but exhibit less sensitivity.

Some specialized tips are available for special application. Chemical functionalized tips, for example, can be used to scan the chemical properties of a surface, detecting the attraction or repulsion forces exerted by the surface on the functionalized tip.

The choice of tip type, cantilever spring constant, etc. is made according to the sample being imaged.
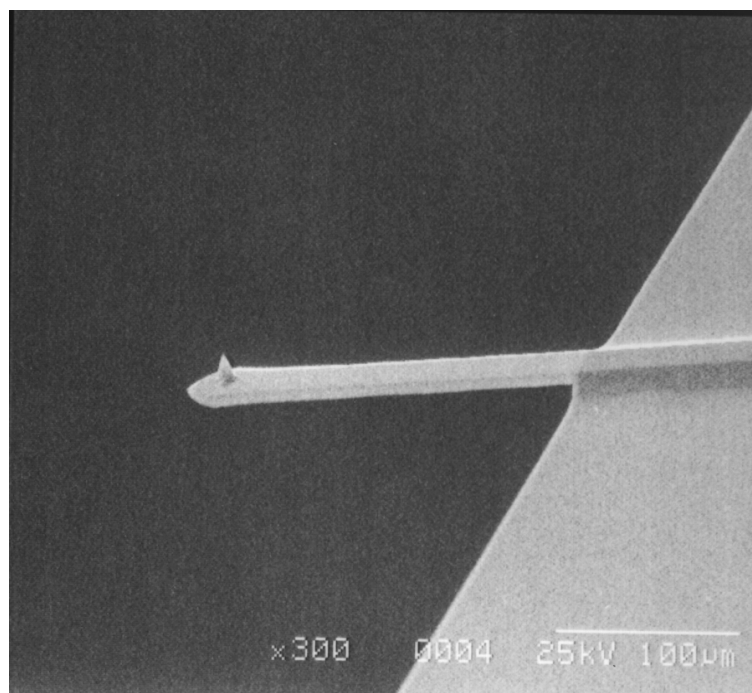
Figure 4. 10   SEM image of an AFM tip [64].

Scanners

Scanners are used to very precisely manipulate sample-tip movement in order to scan the sample surface. Typically, they consist of a hollow tube made of piezoelectric material such as PZT (lead zirconium titanate). Piezo materials contract and elongate when voltage is applied, according to whether the voltage is negative or positive, and depending upon the orientation of the material's polarized grain structure.

In some models the scanner tube moves the sample relative to a stationary tip. In other models the sample is stationary while the scanner moves the tip in order to scan larger samples. Not all scanners react exactly the same to a voltage. Because of slight variations in the orientation and size of the piezoelectric granular structure, material thickness, etc., each scanner has a unique and not linear sensitivity relationship. In fact piezo scanners exhibit more sensitivity (i.e., more movement per volt) at higher voltages than they do at lower voltages. This non-linear relationship is determined for each scanner crystal and the necessary compensations are made by the system, in order to correlate the voltage applied to a definite movement of the scanner. As the scanner ages, its sensitivity will decrease somewhat, necessitating periodic recalibration.

Feedback Electronics and detection mechanism

Another element common to all types of SPM is the feedback system used to control tip-sample interaction. Feedback systems are designed to keep the tip-sample interaction constant as was described before.

The feedback response is based on the electrical signal of a photodiode, that detect the deflection of the cantilever through a optical lever. A laser beam is in fact reflected on the cantilever's edge and multiply its deflection and torsion movements.

The detection mechanism is included in the microscope head as displayed in Figure 4.11
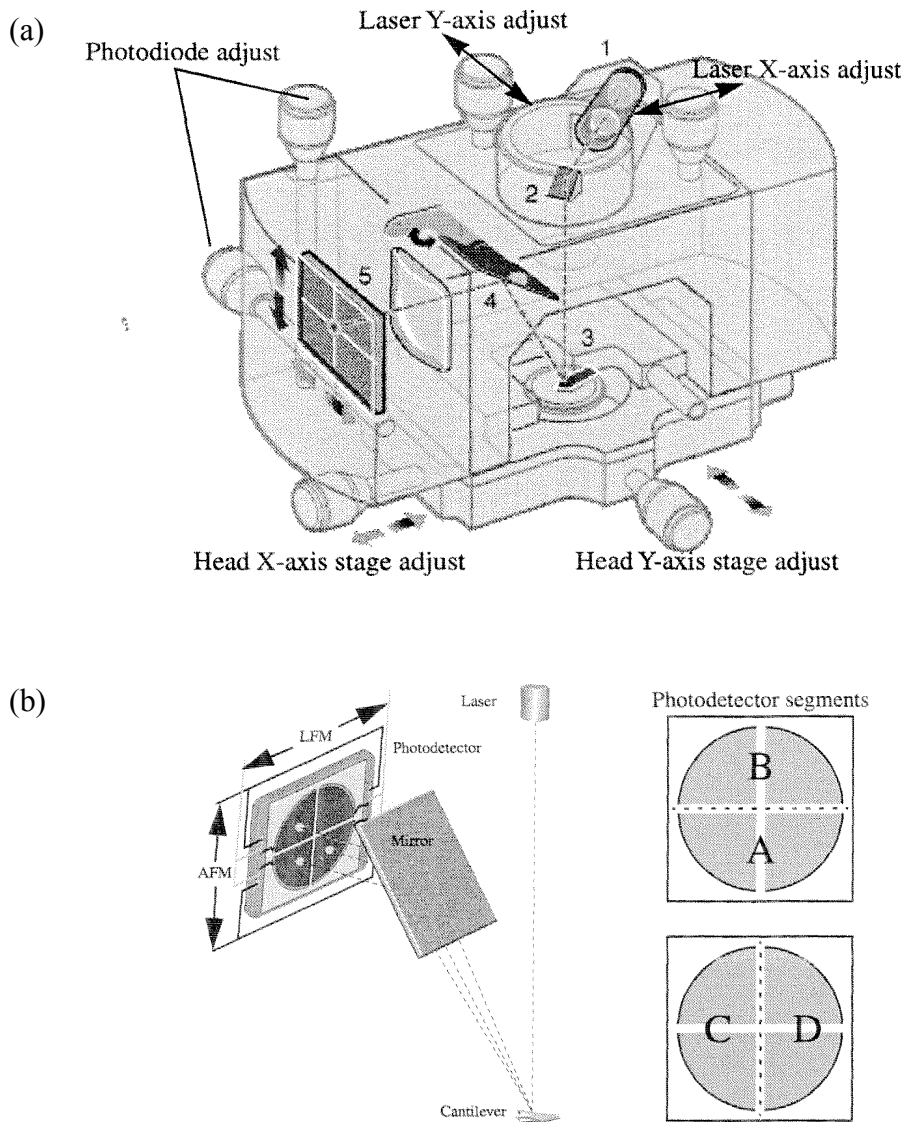
Figure 4. 11   Scheme (a) of the AFM head and (b) of the laser beam used to detect the cantilever deflection [64].

4.1.8 System specifications

Atomic Force Microscopy (AFM) and Force Modulation AFM measurements in this work were conducted in air using a Digital Instruments Multimode, Nanoscope IIIa, equipped with "J" type scanner (x-y range: 125 µm, z range 5µm).

Tapping mode Etched Silicon Tips (TESP, spring constant: 20-100 N/m; nominal tip radius curvature: 5-10 nm, cantilever length: 125 μm) for normal imaging and Force Modulation Etched Silicon Tips (FESP, spring constant: 1-5 N/m; nominal tip radius of curvature: 5-10 nm) for Force modulation were used. Cantilevers for Force Modulation were mounted on a special holder equipped with a piezoelectric bimorph with resonant frequency amplitude of ca. 19 kHz.

4.2 Force Plot

As written before, there are many different interactions between the tip and the surface, that contribute to the force effectively measured by the system. In particular, in contact mode AFM, the force theoretically calculated by the Hooke's law doesn't take in account many parameters as electrostatic forces or the elasticity of the materials. It's however possible to obtain the actual force-distance relation for the tip approaching to the surface and retracting from it. This can be done under normal operational condition, and consist in repeatedly advance the tip towards the surface until it makes contact and then withdraw it. By graphing tip movement versus cantilever deflection, it is possible to obtain a force curve as shown in Figure 4.12.

Force plot, also called Force calibration mode, is usually used to choose the best setpoint to scan a sample without damaging it, but it can also be used to obtain many useful information about the properties of the sample [66-70]. Furthermore this method can be used to calculate a parameter relative to the system used, that is the Detector sensitivity. This parameter depend on the geometry of the laser-tip-detector system and it reflects the amount of voltage change at the photodiode for a given amount of scanner movement. If no indentation of the tip into the surface is assumed, the sensitivity is given by the slope of the force curve after the contact of the tip with the surface. This parameter must be calculated every time that the laser focus on the tip's edge is adjusted. Usually this work is easily done with the help of the AFM software.

The different phases of a typical force plot curve are shown in Figure 4.12. at the beginning the tip descends, but there isn't any contact between the tip and the surface yet (phase 1) . As it becomes close enough to the surface, the tip is pulled down by attractive forces. This is called "jump to contact" point and is usually due to electrostatic attraction or capillary forces. (Phase 2). As the tip is then pressed into the surface, the cantilever bends upwards and the photo-detector signal increases (Phase 3). At the end of the course set by the user, the piezo retracts and the cantilever relaxes downward until tip forces are in equilibrium with surfaces forces. (Phase 4). As piezo continues retracting, the tip sticks to the surface because of adhesion force. (Phase 5). Eventually the tip breaks free and the cantilever rebounds sharply upward. (Phase 6). The piezo goes back to the starting position and there is no further contact with the surface. This cycle is repeated with a frequency set by the user.
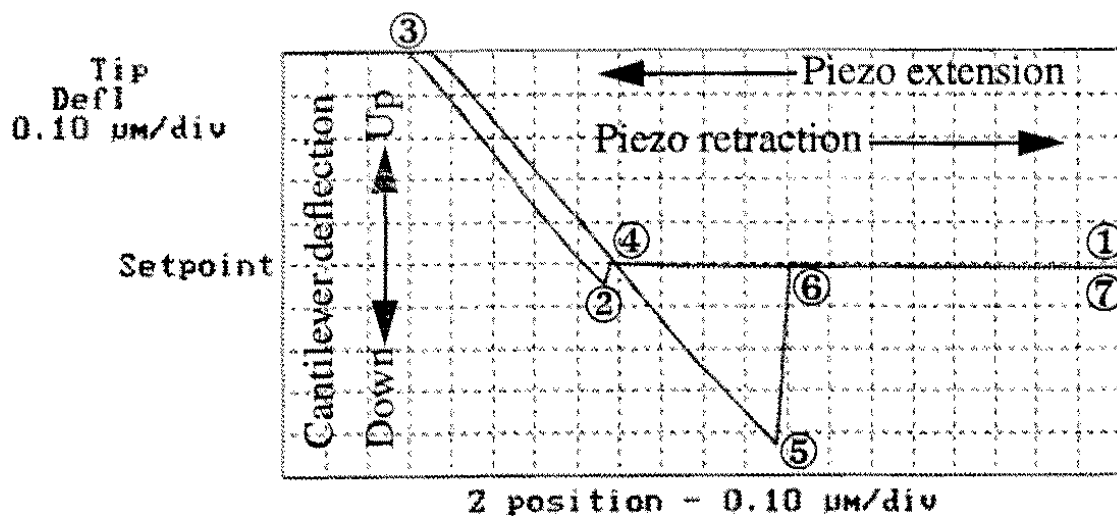
Figure 4. 12   **Typical force plot image- Tip deflection versus tip position**

By studying the shape of the force curves is possible to extract some qualitative information about the elasticity of the sample. In fact, as the tip is pressed against the surface (phase 3) two contemporary phenomena occur: the cantilever bends upwards and the tip indents into the surface. The deflection of the cantilever depend of course on its length, and it's constant, while the indentation amount depend on the elasticity of the

material. For this reason the slope of the force plot in the region 3 and 4 can give information about the elasticity or the hardness of the material [71-75].

Many different theoretical models have been developed to explain this indentation phenomena. Both in the elastic and inelastic deformation case and in some particular cases the amount of cantilever flexion for a given amount of downward tip movement can be correlated to defined physical constant as E-modulus. The slope itself can anyway be taken as parameter for a qualitative measurements of the hardness of the sample at a nanometer scale. The amount of the indentation depends of course on the material's properties and on the spring constant of the cantilever used. For indentation purposes cantilevers with higher spring constant and diamond coated tips are used [76-82].

4.3   Force modulation AFM

Force Modulation AFM is a special feature of Atomic force microscopy that uses the tip as a test probe to obtain information about mechanical properties of the surface. With this method it is not possible to obtain absolute values, but is possible to image contrast between regions of different elasticity and to associate this relative values with the topography of the surface.

This method is therefore useful for many different purposes, i.e.: mapping different components in composite materials, [83,84] for identifying materials domains or organics and other contaminants over high-tech surfaces [85] and for delineating coverage by coatings and other surface layers.

Force modulation works on the basis of contact mode AFM, and the tip is scanned across the surface while the feedback loop maintains constant the force set by the user in the setpoint parameter. This produces of course a normal topographic image. To the tip moving at a constant distance from the surface is then superimposed an oscillation generated by a piezoelectric bimorph assembled in the tip-holder at the resonance frequency of the bimorph.

This oscillation brings the tip to slightly indent into the sample and the response due to variations of the oscillation amplitude is related to the material elasticity, because the tip will be able to indent a soft material more easily than a hard material. The amplitude of the oscillation, detected through the amount of cantilever deflection, is therefore inversely related to the amount of indentation, because a deeper indentation (in soft materials) will cause a smaller cantilever deflection, while a small indentation (in hard materials) generates a larger cantilever deflection. In practice, when the tip encounters a hard site embedded in a softer medium, the harder material absorbs less of the cantilever's energy, causing an increase in the cantilever's response and signal amplitude. (Figure 4.13).

All this is graphically rendered with darker colours for the harder sites and lighter colours for softer sites. That means that a larger oscillation amplitude is reported in the force modulation image with a darker colour.

The contrast generated by areas with different elasticity depends on the difference between the materials and on the experimental conditions used, (i.e. the cantilever spring constant, the amplitude of oscillation and the force applied by the tip on the surface) and cannot be used to compare different scans because of the impossibility to maintain all the parameters constant. A force modulation image can be anyway be used to have an idea of the distribution of two materials on a sample and gives a map of the relative elasticity together with the topography of the area scanned.
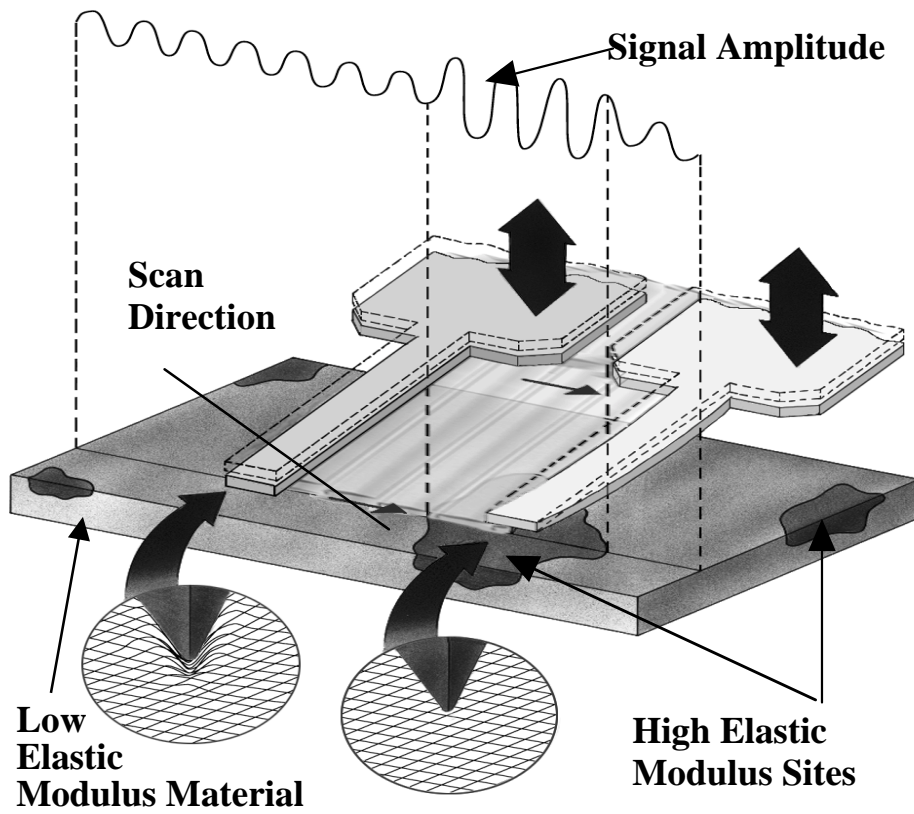
Figure 4. 13   Force modulation AFM – measurement principle [64].

4.4   Polarization Microscopy

Polarization microscopy, and more generally transmission microscopy, are techniques that belong to the domain of the geosciences and are normally used as powerful tools for the geological and mineralogical characterization of rocks and minerals [86-88]. The applications of these techniques are also extended to include artificial materials, such as glasses, polymers and ceramics. The general arrangements of the optical elements is shown in Figure 4.14.

Polarization microscopy is a branch of transmission microscopy that employs polarized light to obtain information about the crystal system as well as orientation and texture. By using crossed polarizers, isotropic cubic or amorphous materials can be

distinguished from anisotropic materials, and this particular feature has been used in this work to analyze samples formed by sand consolidated by amorphous material.

Isotropic cubic or amorphous materials are easy to recognize because of the permanent darkness of the transmitted beam at any orientation when using crossed polarizers. That is easily understood because isotropic cubic or amorphous materials do not cause any birefringence and the polarization of the light remains constant at any orientation of the sample. If the analyzer is oriented at 90° respect to the polarizer the light will be stopped completely.

On the other side if the transmitted beam propagates through an anisotropic material, splitting of the propagating waves takes pace. Interference phenomena due to birefringence generate therefore polarized light which wavelength and amplitude are different to that entering the crystal.

The observed beam has therefore a wavelength and an intensity that depends on:

a) the wavelength of the incident beam
b) the optical properties of the crystal (extent of birefringence, coefficient of absorption)
c) the relative orientation of the crystal with respect to polarizer and analyzer
d) the thickness of the sample

If the vibration planes of the polarizer and analyzer are mutually perpendicular the intensity of the transmitted beam has for a particular wavelength maximum and minimum points depending on the relative orientation of the crystal respect to the polarizer and analyzer. Usually the sample is mounted on a rotating platform, whose complete rotation brings the crystal four times in a extinction points, where the light doesn't pass through the analyzer.

In a sample composed by quartz sand corns embedded in amorphous matrix, the anisotropic sand corns show a brightness that depend on the rotation angle of the sample on the plane perpendicular to the light beam. The amorphous phase, on the other side, result always dark under polarized light, at every orientation of the sample.

(a)
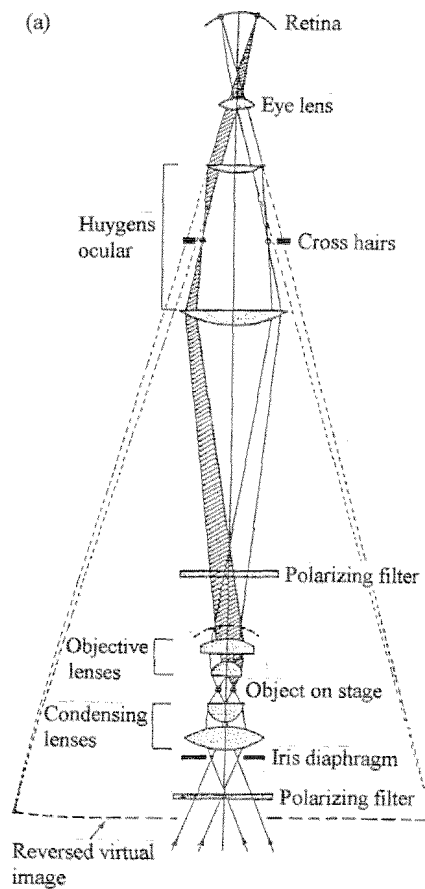
Figure 4.14   Beam-path in Orthoscopic light transmission microscopy

4.5   Biaxial flexural strength

Biaxial flexural strength is in this work intended as a mechanical method to assess the quality of a consolidating treatment on natural stone. The consolidation of an aged stone is in fact intended as the replacement by the consolidating agent of the previously lost bounding materials and the improvement of the contact between the grains. Biaxial flexural strength is here used to measure the cohesion between the grains that form the stone [89-91].

This method, based on the modulus of rupture σ obtained from a bend test, is applied to stone disks through concentrically induced stress until fracture of the sample. This particular application of the biaxial flexural strength method has been developed in

1983 by Wittmann & Prim [8] as analytical method for drill core slices, because of the substantial differences of the samples obtained for restoration purposes from those that can be analyzed by the standard 3 point flexural strength method. These samples consist in drill core slices with a diameter of 5 to 10 cm and a thickness of 0,5 to 1 cm, that are analyzed in order to have a profile of the stone's mechanical condition.

The value of the modulus of rupture is obtained by the formula:

$$\sigma = \frac{3 \cdot F_{br}}{4\pi \cdot d^2} \left[2(1+v)\ln\frac{a}{b} + \frac{(1-v)\cdot(a^2-b^2)}{a^2} \cdot \frac{a^2}{R^2} \right]$$

where:
- F_{br} = Force applied on the load rings at the rupture point. [N]
- d = Thickness of the sample disk [mm]
- v = Poisson's ratio (here v = 0.25)
- a = Radius of the load ring [mm]
- b = Radius of the bearing ring [mm]
- R = Radius of the sample disk [mm]

The Elastic-modulus E can be also calculated from the slope of the curve obtained plotting the deformation of the sample versus the force applied by the mean of the formula:

$$E = \frac{1,5 \cdot F}{f_0 \cdot d^3} \cdot (1-v^2)\left[b^2 \ln\frac{b}{a} + \frac{(a^2-b^2)\cdot(3+v)}{2 \cdot (1+v)} \right]$$

where:
- F = Force applied on the load rings [N]
- f_0 = flexure of the sample [mm]
- d = Thickness of the sample disk [mm]
- v = Poisson's ratio (here v = 0.25)
- a = Radius of the load ring [mm]
- b = Radius of the bearing ring [mm]
- R = Radius of the sample disk [mm]

In both the formulas the Poisson's ratio ν for elastic deformation is hold constant at $\nu = 0.25$. This value is for natural stone between the range 0.18- 0.32 , but specific values for particular samples are not to be found in the literature. The variation of the Poisson's ratio in the given range and for the forces normally exerted for natural stones causes anyway small effects on the calculation of σ (error $< \pm 0,5$ N/mm) and can be taken as arbitrary chosen parameter. [91]
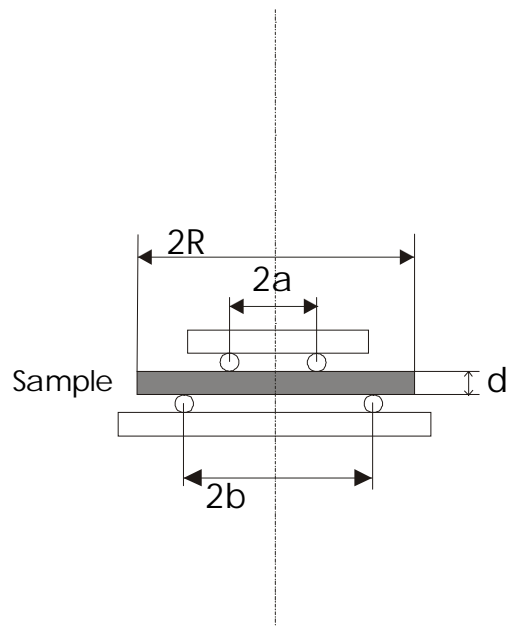
Figure 4. 15   Scheme of the load cell in biaxial flexural strength on disk-shaped sample

Chapter 5

Sample preparation

5.1   Introduction

To obtain concrete results from AFM analysis, a great care should be taken over the choice of the samples and on the way used to prepare them. AFM is, in fact, a surface technique and gives many information about surface's topography and properties. Nevertheless it's a difficult task to prepare the samples in such a way that the properties of the surface are not altered by the preparation itself.

For the composite materials which are the object of the present work, most interesting is to see how the topography and the surface properties of the samples change in relation to the conditions chosen to prepare them. The main problem is that the surface is rarely representative of the whole system, and in general it has different properties and characteristics. For example a bulk sample prepared with the sol-gel technique, assumes different properties at the air interface, because of the thermodynamic surface energies and because of the air moisture. The behaviour at the interface is in any case the most interesting thing, in order to develop a model to understand how a hardener reacts or adheres to the stone. Since the macroscopic properties of the bulk material can be easily studied, more difficult is to understand how the new material interacts with the old stone, and to do that, the characteristic of the two surfaces must be known.

For what concerns composite materials, this means to understand how the two phases are distributed and how this distribution can be controlled. For this reason a particular care is given to the preparation of the samples and to the experimental conditions used.

5.2   Model system

The commercial hardeners like *Rajasil Putzfestiger*, *Wacker Steinfestiger*, *Goldschmidt Tegovakon V*, are mixtures of different solvents, hydrolysed TEOS and an acrylic resin. Since the chemical formula of the resins and the exact composition of the mixtures are not specified by the manufactures, we decided to start the study on a simplified model system.

For this purpose methyl methacrylate and pure TEOS were used and mixed in well defined proportions. Furthermore a single solvent was used. The commercial products usually contain at least two solvents, an alcohol (i.e. isopropanol) for the sol-gel process and an aromatic mixture to solve the resin. This can lead to phase separation due to different volatility and different properties of the two solvents since the first steps of the process.

In the system chosen THF was used as single solvent. Though THF is not the best solvent for sol-gel deposition of silica because of its high volatility, it has a low density in order to promote the penetration of the solution into the stone and can solve both the TEOS/H_2O mixture and the Methyl methacrylate resin. The simplified system was studied and analysed, changing only the composition of the starting solutions.

Two different preparation procedures were used. The first one is to prepare bulk samples and to analyse the fracture surface. The second one is to prepare the samples as thin films on an amorphous substrate with the dip-coating technique and then analyse them. This is consistent with the idea that when a composite material acts as consolidant, it builds a thin film between the loosed grains, which has a thickness of the same order of that obtained with the dip-coating technique.

To reproduce the formation of the film inside a stone, the deposited film were hanged over the solutions vapours for two minutes, to slow down the solvent evaporation. In this way more homogeneous films have been formed. The preparation of the samples as films is important also for another reason. The phase separation process, in fact, continues until the mobility of the system is too low to allow further separation, and the system results quenched at that point. In thin films this point is reached much earlier, because of the fast evaporation process and the small amount of material respect to the large surface

involved. The formation of thin films is therefore much more significant in order to understand the first steps of the separation process.

To check if both the organic and inorganic part are deposited during the film formation and to control the kind of interaction occurring between them, an IR spectroscopy analysis was done as it's described in chapter 7.

To reduce the influence of the moisture, an excess of water was added to the starting solution. Furthermore the solutions were left for 24 hours to react in a closed vessel prior to mix them with PMMA solution and let the solvent dry.

5.3 Catalysis

The sol-gel process involved in the formation of silica gel starting from a solution of tetraethoxysilane (TEOS), requires a catalysis because of the low reactivity of the hydrolysis process. As explained in chapter 3, three different catalysis are possible for these systems: acid, basic and nucleophilic. In this work the acid catalysis was chosen as reference method.

The acid catalysis, in fact, produces a three dimensional molecular network, rather than the colloidal particles produced with basic catalysis. This tendency helps the homogeneous growth of the hybrid system promoting the interpenetration of the organic network with the growing inorganic one. Furthermore acid catalysis, because of this fast three dimensional growth of the network and a not complete condensation of the system, leaves many OH groups unreacted at the Silicon atoms [32]. These OH groups can form H-bonds with the carbonyl groups present on the organic polymer.

On the other side, basic catalysis produce closed particles which grow with a nucleation process and which promote phase separation between the organic and inorganic part of the hybrid material. Some test samples done with basic catalysis confirm this tendency. Some test films were produced starting from a solution with basic catalysis, but phase separation was evident (opaque films) at any PMMA/silica ratio. (see Figure 5.1).
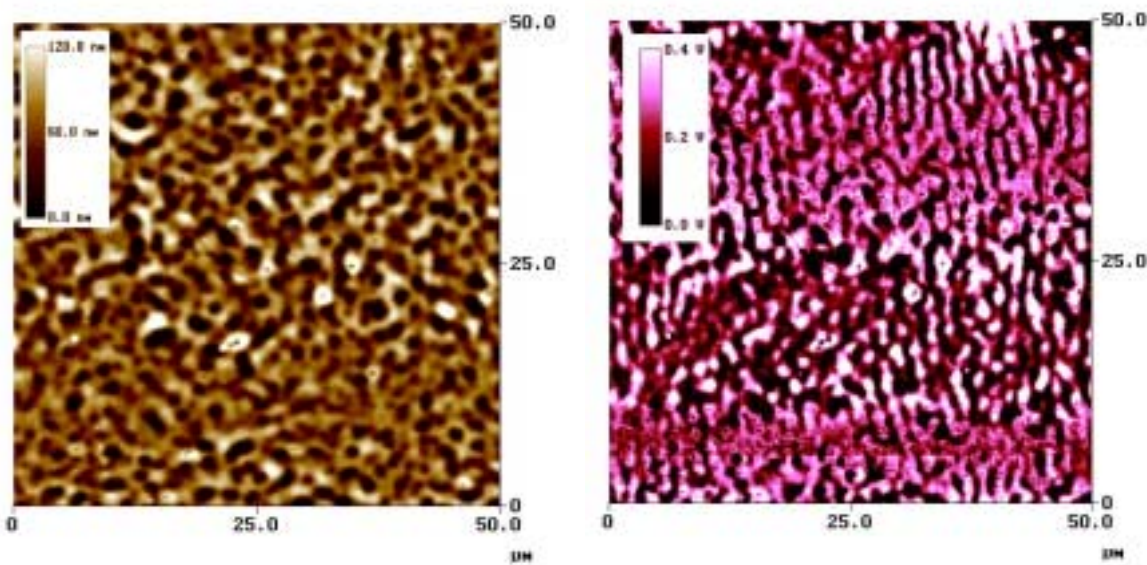
Figure 5. 1 **a) Topography of the film Nap2t3 (example: film with lower opacity was taken) on a 50×50 μm area. The surface is highly rough. b) Force modulation image of the same area (z-axis = amplitude) shows phase separation on a micrometer scale.**

Together with the acid catalysis, which is well known and described in literature, another catalyst was used, which is typically employed in the commercial stone hardener products. This catalyst is a tin compound, dibutyltindilaurate (DBTL), which is known as a catalyst for silicones curing [92-94].

The main advantage in using such a tin compound is the fact that it promotes the gelation of silica at a neutral pH. This is particularly useful in materials that have to be used on natural stones, because it reduces the possible damages by acid or basic solutions to the stone's structure.

The catalytic path for DBTL silicones curing is well known and shown in scheme 5.1, but any literature can be found for the catalysis of the hydrolysis reaction of alkoxysilanes. Most likely the first step of the sol-gel process, the hydrolysis, follows a path similar to that of the basic or nucleophilic catalysis, while the condensation follows the same path described for the silicone curing. Some evidences supporting this hypothesis are reported in chapter 6 and in chapter 7.
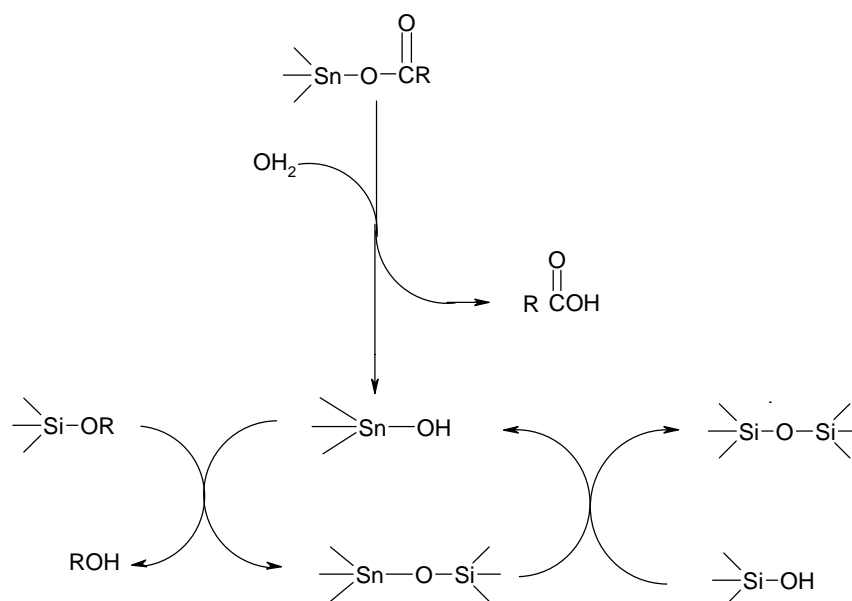
Scheme 5. 1 **Catalysis of silicones condensation by dibutyltindilaurate (DBTL)**

5.4 Experimental

The procedure used to prepare the starting solutions for thin film preparation is described. The same procedures were used to prepare all the samples for the different analysis, even if with different quantities. The name of the samples is defined by the proportion between the PMMA and the TEOS solution. the first part of the name describes the catalyst used.

Example: DBP2T2   (catalyst: DBTL, 2g PMMA 10%, 2 ml TEOS 1M)

5.4.1   Reagents and materials.

- TEOS (tetraethoxysilane), DBTL (dibutyltin dilaurate) and PMMA were purchased from Fluka and used as received.

- PMMA [Poly(methyl methacrylate-co-methacrylic acid)] low molecular weight, purchased from Fluka. The molar proportions of methyl methacrylate to methacrylic acid is: 1 : 0,16, Average Mn: ca. 15000, Mw: ca. 35700 (calibration versus Polystyrene) and ca. 33800 (calibration versus Poly-methyl methacrylate).

- THF was purchased in reagent grade and used as received.

- Soda lime slides, purchased from *Menzel-glaser* (Germany), were used as substrate and were washed prior to be used as described below.

- Silicon wafers were purchased from Wacker.

5.4.2 Starting solutions

TEOS 1 M in THF and PMMA 10% weight in THF were prepared. A solution of DBTL 0,1 M in THF was freshly prepared few minutes before to be added to solution a).

a) To 15 ml of a stirred solution of TEOS 1M in THF were added 1080 µl of H_2O ([H_2O]/[TEOS] = 4) and 496 µl of DBTL 0,1 M (1% wt. respect TEOS) in THF by a micropipette. The mixture became slightly opaque just after the water addition. After few minutes stirring the mixture returned clear.

b) To 15 ml of a stirred solution of TEOS 1M in THF was added a solution of 0,15 g HCL conc. ([HCl]/[TEOS] = 0,1) In 1080 µl water ([H_2O]/[TEOS] = 4). The mixture became slightly opaque just after the water addition. After few minutes stirring the mixture returned clear.

The solution a) has been mixed with the PMMA solution after 24 h. stirring, following the proportions:

Solution name	PMMA 10% in THF (g)	TEOS 1M in THF (ml)	SiO_2/PMMA weight (Theoretical after TEOS complete condensation)
DBP1T4	1	4	2,3
DBP2T3	2	3	0,9
DBP2T2	2	2	0,6
DBP3T1	3	1	0,2

The solution b) has been mixed with the PMMA solution after 24 h. stirring, following the proportions:

Solution name	PMMA 10% in THF (g)	TEOS 1M in THF (ml)	SiO_2/PMMA weight (Theoretical after TEOS complete condensation)
HCLP1T4	1	4	2,3
HCLP2T3	2	3	0,9
HCLP2T2	2	2	0,6
HCLP3T1	3	1	0,2

5.5   Film deposition

Films were deposited with the dip-coating technique. A preliminary series of films were deposited by hands and then checked with AFM. Two series have been deposited with controlled drawing speed by the use of the apparatus described in Figure 5.2. The dip-coating apparatus is a home made box, [95] where a metallic bar used to hold the substrate can be moved up or down into the solution with a controlled speed. A solid bar is used to

avoid as much as possible lateral movements of the sample, as well as vibrations and swings. These movements affect, in fact, the homogeneous distribution of the film on the substrate. The box can be closed and the atmosphere inside controlled. A thermometer inside the box is used to check the operational temperature. Beneath the substrate is placed the starting solution, prepared as described before.

First series:

       dipping speed   : $0,14 \pm 0,02$ cm/sec

       withdrawal speed : $0,13 \pm 0,02$ cm/sec

       T = 25 °C

Second series:

       dipping speed   : $0,45 \pm 0,07$ cm/sec

       withdrawal speed : $0,41 \pm 0,07$ cm/sec

       T = 24 °C

in both the series the substrate was left 15 sec dipped in the solution and then left hanged over the solutions vapours for 120 sec after being withdrawn. This was done to slow down the evaporation of the solvent. Soda lime slides were used as substrate after being cut in a suitable format. (ca. 2,5×1,5 cm). Substrates were prepared repeating 10 times a cycle of washings with water and soap, distilled water, isopropanol, to eliminate powder and other contaminants and then let dry [96].
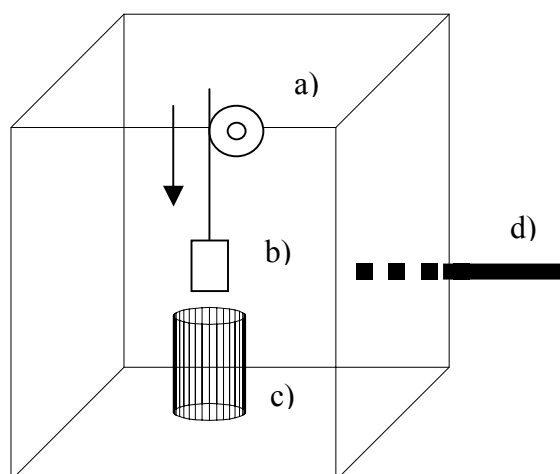
Figure 5. 2   Dip-coating apparatus. a) motor, b) substrate slide, c) sol-gel solution, d) thermometer.

Table 5. 1   Film and monolith appearance description

Sample names (starting solutions)	Film appearance	Monolith appearance (after 3 months)
DBTEOS	Transparent, clear	Transparent, clear, fragmented
DBP1T4	Transparent, clear	Transparent, clear, broken
DBP2T3	Transparent, clear	Transparent, clear, bulk
DBP2T2	Transparent, clear	Transparent, clear, bulk
DBP3T1	Transparent, clear	Transparent, clear, plastic deformations
HCLTEOS	Transparent, clear	Transparent, yellow, fragmented
HCLP1T4	Opaque, white	Phase separation (opaque-yellow) broken
HCLP2T3	Opaque, white	Phase separation (opaque-yellow) broken
HCLP2T2	Transparent, clear	Opaque, cracks
HCLP3T1	Transparent, clear	Opaque, bulk

5.6 Monolith preparation.

Monolith were prepared letting the solutions slowly dry in closed vessels with some holes in the stopper. A week was required to observe the first gelation phenomena on DBTL catalysed solutions. At least three months to have all the samples dried. It was clearly observed that under the conditions used, DBTL catalysed solutions gelate faster than the HCl ones. The gel obtained from HCl catalysed solutions is colourless like the one obtained by DBTL catalysis, but the monoliths obtained after some months aging show in the HCl catalysed silica a strong yellow colour, probably due to the reaction of HCl with the solvent. In fact monoliths previously prepared using isopropanol as solvent result to be colourless as described in the literature.

Severe phase separation was observed on some of the HCl catalysed samples. (Table 5.1). Photos of the resulting monoliths are reported (Figure 5.3). For all the monoliths were used the same names of the solutions from which they were obtained. The most severe phase separation was observed on the samples HCLP1T4 and HCLP2T3, where practically two different bulk materials can be observed. The fact that the acid catalysed silica assumes a yellow colour, helps to distinguish between the two phases (Figure 5.7). These samples correspond to the two films that show phase separation. In the films the phase separation is still at a micrometric scale, and that confirms the idea that the rapid solvent evaporation during the film formation stops the process of separation after the first steps. For the solutions HCLP2T2 and HCLP3T1, in fact, the films result to be transparent and homogeneous, but the monoliths are opaque due to phase separation at a micrometer scale (Figure 5.6).

Under the conditions used most of the monoliths with a higher silica content result broken, probably because of the high evaporation rate of THF. If the solvent is let to evaporate faster (without stopper), phase separation phenomena are observed also in the DBTL series. If slower, good monoliths of Silica alone can be obtained, but HCl composites result not yet formed after three months.

Samples obtained from solutions with a higher percentage of PMMA result to be unbroken but they show some plastic deformations due to the drying process. Monoliths of hybrid material transparent and not broken were obtained from the solutions DBP2T2

(Figure 5.4) and DBP2T3 (Figure 5.5). Monoliths with higher PMMA contents (DBP3T1, HCLP3T1) do not show the high volume contraction typical of sol-gel process that can be easily observed for example on sample DBP2T2. Shrinkage occurs in fact during Silica formation, while PMMA volume remains constant after the loss of solvent. At a certain TEOS/PMMA ratio the shrinkage phenomena result to be negligible.

Figure 5. 3   Monoliths obtained by sol-gel process

Figure 5. 4   Monolith DBP2T2

Figure 5. 5   Monolith DBP3T3

Figure 5. 6   Monolith HCLP3T1, sample is opaque due to phase separation at a micrometer scale

Figure 5. 7   Monolith HCLP2T3, full phase separation between silica (yellow) and polymethylmethacrylate.

5.7 Conclusions

Some information about the evolution of the solutions to give monolith and films can be achieved immediately from the bare observation of the resulting samples. The fact that a film can result transparent or opaque, gives a first idea of the phase separation, and the observation of the aspect of the monolith gives more information about the homogeneity of the material after the two phases had time to separate.

From all the experiments done it results anyway clear that the conditions used (i.e. solvent, gelation time, composition of the starting solution) have a great influence on the resulting material. Nevertheless it seems possible to use some of these variables to tailor the properties of the material according to the needing of the practical application.

The evaporation rate contributes significantly to yield a transparent and unbroken monolith. This confirms the fact that the growing of the inorganic network in the organic matrix is a matter of kinetic and not only of thermodynamic equilibrium.

Chapter 6

Properties on a nanoscale

6.1   Introduction

To obtain information about the evolution of the reaction mixture and therefore the generation of the final hybrid system, films from solutions with different TEOS/PMMA rate were prepared through dip-coating deposition using both acid and dibutyltindilaurate (DBTL) catalysis and then analyzed by different techniques. The analysis of thin films is particularly useful in order to understand their use as natural stone consolidants. In fact, the composite materials investigated here as model films should be not too different from those formed among stone grains under real operational conditions.

A first analysis on the samples topography has been made, to compare the surfaces of the films obtained with different composition of the starting solution and parameter like Z-range and roughness have been calculated. Topography gives only few information about a system composed by two materials, but it's important to distinguish if the system develops like a real hybrid material or if it separates into two different phases.

A study of the thickness of the films has also been made. Problems rise in fact if the films are too thin. In this case the substrate influences greatly the system, destabilizing it and promoting phase separation. Film thickness depends, on the other hand, also from the composition of the Sol-Gel solution. PMMA-rich films are in fact much thicker than Silica-rich films. Since the films were made by a single dip deposition, film thickness is given by the step height between film and substrate, and can be easily determined by a profilometer.

Finally, force modulation analysis allows us to observe how the two phases separate, creating a map of the relative hardness on the surface of the resulting films. This analysis method helps us to understand what happened in the system, letting us to observe

it at the end of the entire process. In fact, several considerations can be drawn about phase separation, observing how the system had developed starting from different solutions.

Another feature of AFM is the possibility to compare the force plots made on the various samples. The slope of the contact region of the curves can be in fact correlated to the elastic and plastic properties of the samples, and this allows us to advance hypothesis about the E-modulus of the film prepared. The importance of the elastic modulus in materials for consolidation of natural stones is given by the fact that the amorphous silica formed by sol-gel process is too brittle for such a purpose. The use of hybrids materials is therefore aimed to decrease the E-modulus of the consolidant material and to improve the properties of the treated stone.

6.3   Topography

The main feature of the AFM is the possibility to provide in a short time and almost without sample preparation, the topography of a surface from a micro to a nanometer range. All the samples were analyzed in different position and with different magnifications. The pictures more representative of the surfaces analyzed are shown in Table 6.2-6.4

6.2.1 Experimental

Thin films were prepared on soda lime substrates as described in chapter 5. Pieces of suitable dimensions (ca. 1 × 1 cm) were then cut and mounted on steel disks sample holders for AFM by the use of adhesive tabs. All the experiments were conducted in air and at room temperature.

For the topography images, Tapping mode Etched Silicon Tips were used (TESP, spring constant: 20-100 N/m, nominal tip radius curvature: 5-10 nm, cantilever length: 125 μm).

AFM pictures were made using mainly tapping mode, in order to avoid any damage to the surface. For every sample, AFM pictures in the range 1×1 μm, 5×5 μm, 20×20 μm were made in different locations. Because the surface appears to be rather smooth and flat, only differences on a larger scale can be seen. Therefore only measurements of 20 μ size or more are shown. (Table 6.2-6.4). Experimental parameters related to the shown pictures are reported in Table 6.1.

Table 6. 1 **Experimental parameter used for the AFM pictures shown. Measurements were performed with tapping mode, except where explicit written**

Sample name	Scan size (μ)	Scan rate (Hz)	Z limit (μ)
DBTEOS.024	20	1,22	5,399
DBP1T4.027	20	0,9	5,399
DBP2T3.027	30	1,03	5,672
DBP2T2.021	20	0,825	5,399
DBP3T1.026	20	1,44	5,672
PMMA.021	20	0,731	5,399
HCLTEOS.024	20	1,09	5,399
HCLP1T4.025	50 (contact mode)	0,690	5,399
HCLP2T3.022	50 (contact mode)	0,866	5,672
HCLP2T2.024	20 (contact mode)	0,607	5,399
HCLP3T1.024	20	0,878	5,399

6.2.2 Results and Discussion

All the samples, except HCLP1T4 and HCLP2T3 are transparent and homogeneous at a first sight. HCLP1T4 and HCLP2T3, result to be white-opaque films and their topography reveals the presence of features with a micrometer size. Roughness parameters and Z-range have been calculated, in order to rationalize the information achievable from the pictures.

Z-range is the height difference between the highest and the lowest point of the scanned surface. Roughness can be expressed by two different parameters. R_a is the mean value of the surface relative to the center plane and is calculated using the formula:

$$R_a = \frac{1}{LxLy} \int\limits_0^{L_y} \int\limits_0^{L_x} |f(x,y)| d_x d_y$$

where f(x,y) is the surface relative to the center plane and L_x and L_y are the dimensions of the surface [63].

RMS is the standard deviation of the Z values within the given area and is calculated as:

$$RMS = \sqrt{\frac{\sum (Z_i - Z_{ave})^2}{N}}$$

where Z_{ave} is the average of the Z values within the given area, Z_i is the current Z value, and N is the number of points within the given area [63]. Because all roughness parameter are affected by flattening and plane fitting process, all the images have been treated with the same second order flattening.

As can be easily seen from Table 6.4, the roughness data relative to these two samples are several orders of magnitude higher than all the other, which are smooth and flat. This agrees with the fact that a strong phase separation leads to a rough topography with precise features. The features showed for both HCLP1T4 and HCLP2T3 result exactly reproducible for the given starting solutions, but show a dependence on the position with respect to the withdrawal direction during the film deposition.

Generally, samples with a higher percentage of PMMA seem to have lower roughness than samples containing more silica (Table 6.2). this is justified by the greater contribution of the organic part of the composites to a smooth surface.

Table 6.2   **AFM topography and roughness data of the samples obtained with DBTL catalysis.**
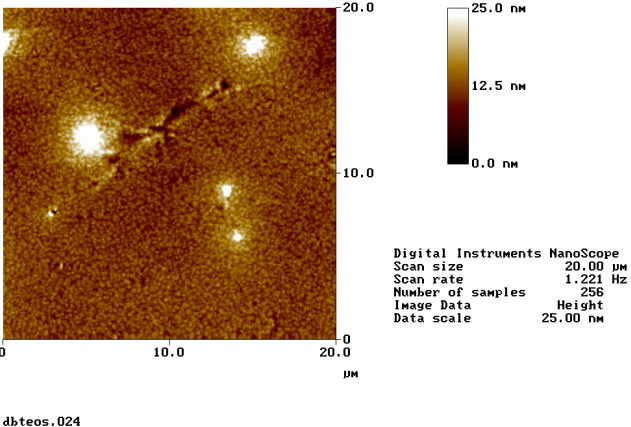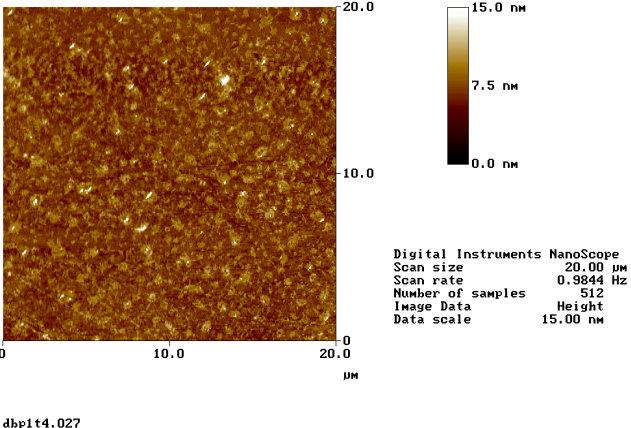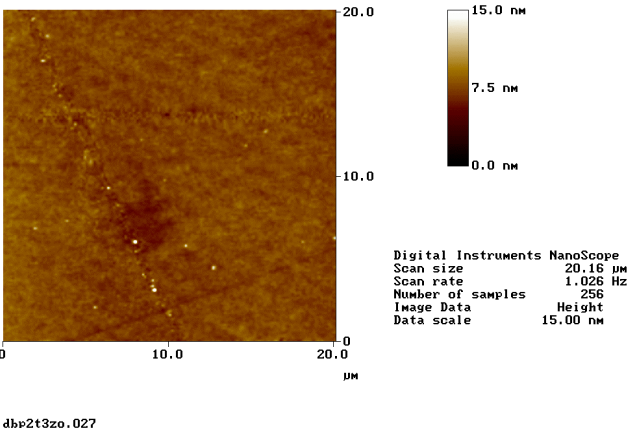
Sample name	Topography	Roughness (nm)
DBTLTEOS (20×20 μm)		Z range = 86.039 RMS = 3.166 Ra = 2.010
DBP1T4 (20×20 μm)		Z range = 28.639 RMS = 1.262 Ra = 0.955
DBP2T3 (20×20 μm)		Z range = 12.029 RMS = 0.557 Ra = 0.422

Table 6. 2   **Continued**
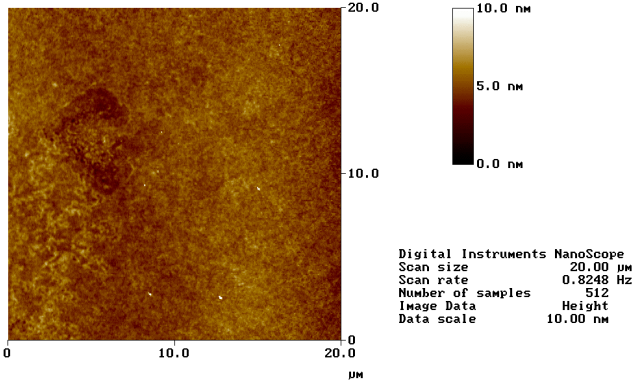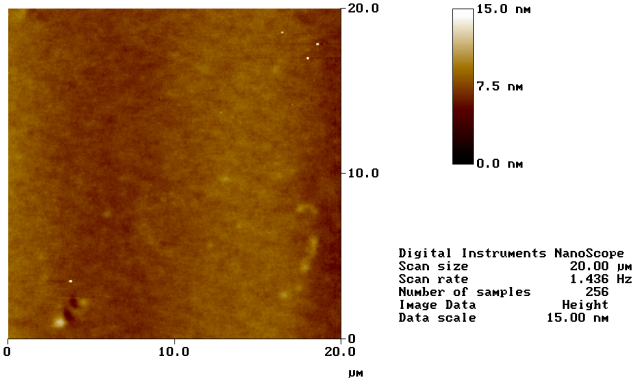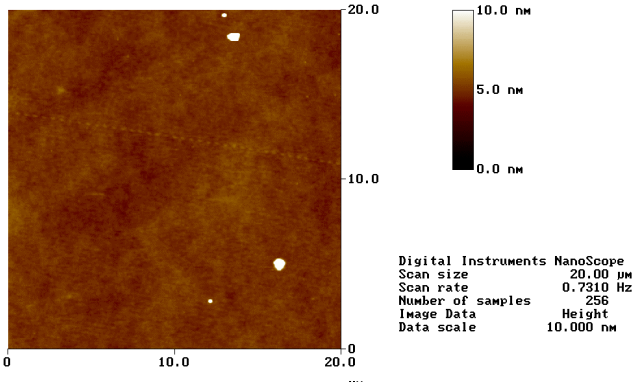
DBP2T2 (20×20 μm)		Z range = 15.388 RMS = 0.614 Ra = 0.481
DBP3T1 (20×20 μm)		Z range = 10.622 RMS = 0.726 Ra = 0.600

Table 6. 3   **AFM topography of PMMA film and roughness data**

PMMA (20×20 μm)		Z range = 3.337 RMS = 0.298 Ra = 0.235

Table 6.4 **AFM topography and roughness data of the samples obtained with HCl catalysis.**
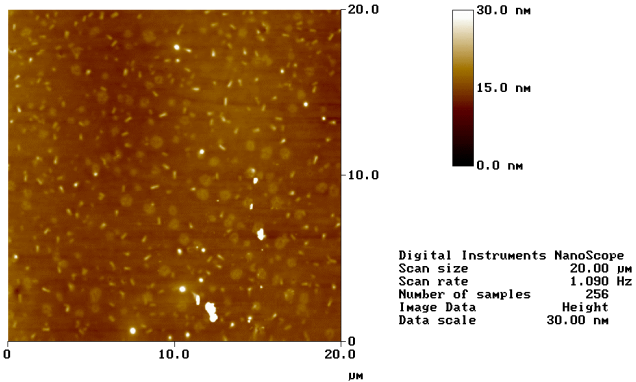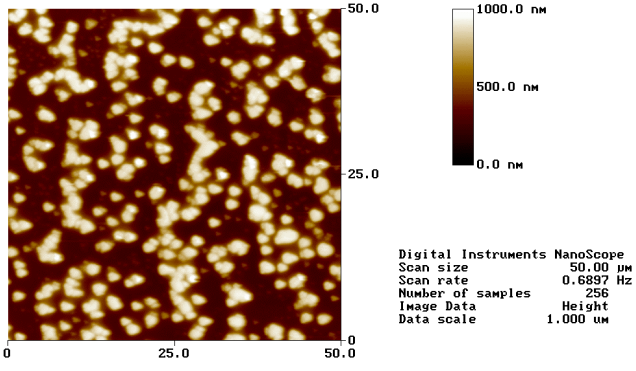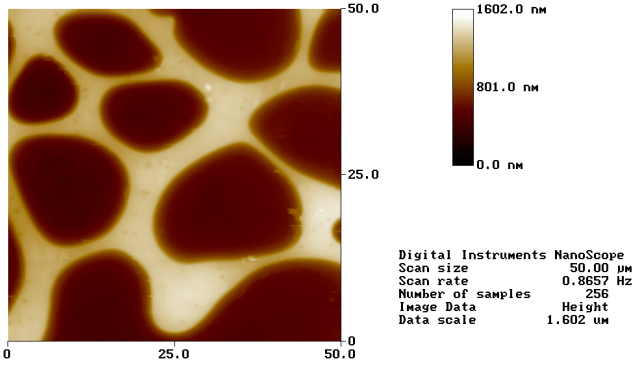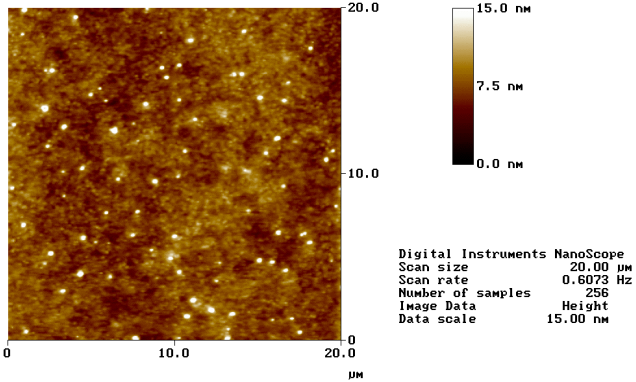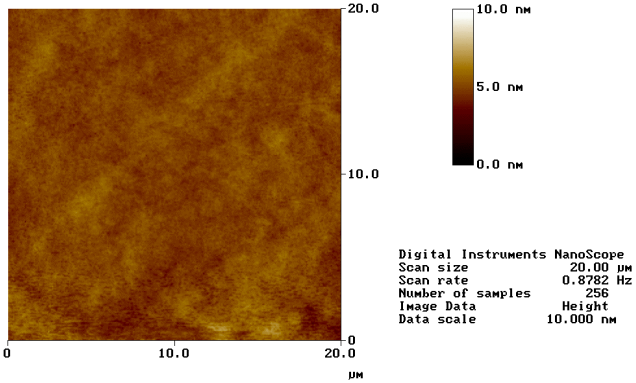
Sample name	Topography	Roughness (nm)
HClTEOS (20×20 μm)		Z range = 40.659 RMS = 1.503 Ra = 1.001
HCLP1T4 (50×50 μm)		Z range = 933.75 RMS = 230.22 Ra = 204.47
HCLP2T3 (50×50 μm)		Z range = 1138 RMS = 319.53 Ra = 288.71

Table 6. 4   **Continued.**

HCLP2T2 (20×20 µm)		Z range = 23.350 RMS = 1.507 Ra = 1.083
HCLP3T1 (20×20 µm)		Z range = 5.120 RMS = 0.445 Ra = 0.342

6.3 Thickness

Although the thickness of a film produced with the dip-coating sol-gel technique depends mainly on the withdrawal speed (see chapter 3), for these composite materials it clearly depends also from the composition of the starting solution. The higher the PMMA content, the thicker is the resulting film, at a constant withdrawal speed.

Furthermore, different adhesion phenomena occur at the film boundary between the substrate and the various solutions employed. PMMA richer films present, in fact, an accumulation of material at the film boundaries, corresponding to the start-up phase, while silica richer films do not (Figure 6.1).

The solvent employed seems to have also a great role, since the kinetic of the gelation process of silica depends greatly on the evaporation rate of the solvent. Because of this reason it was chosen to use a single solvent (THF) in all the experiments, in order to simplify the variables involved.

Profile DBP1T4   **Profile PMMA**
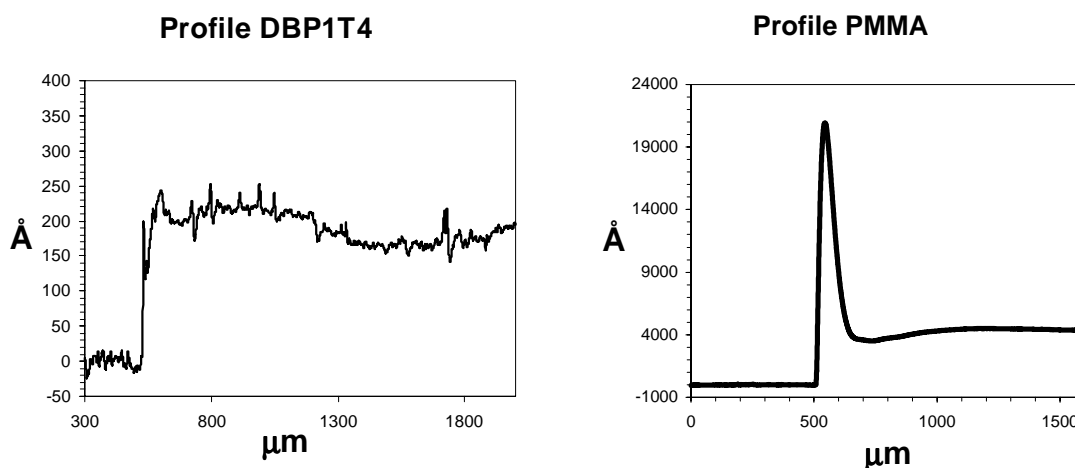
Figure 6. 1   **Profiles of samples DBP1T4 and PMMA. PMMA film is much thicker than DBP1T4 and it presents a high material accumulation at the film boundaries. Withdrawal speed = 0.41 cm/s**

6.3.1 Experimental.

Measurements were performed on samples prepared with the same experimental conditions used for samples analysed by AFM. Scans were made on each sample with 1 mg weight applied to the tip, not to ruin the surface. Furthermore, to check the profile obtained, each sample was turned of 180° and measured on the other direction. Value reported in Table 6.5 are the mean value of 5 different profiles measured at different positions.

6.3.2 Results and Discussion

In Figure 6.3 the thickness of two series of samples prepared with DBTL as catalyst are shown. The two series were prepared under the same experimental conditions, but using different drawing speed. Though the series with the slowest speed should be thinner, it is not. This is particularly true for what concerns the samples DBTEOS and DBP1T4, where the silica content is higher. In this case the film prepared at lower speed is not thinner, but it results not homogeneous, as can be seen from AFM analysis, and it doesn't cover the whole substrate. This is probably due to the solvent, which has a high volatility and doesn't consent a proper film deposition.

On the other hand, the sample PMMA shows a clear dependence on the drawing speed and it results thicker as the withdrawal speed increases. The same comparison can't be done for the films made using HCl as catalyst, because of macroscopic phase separation that occurs on the samples with the higher silica amount. The phase separation increases in fact greatly the thickness of the films as can be seen from a comparison between the films obtained at the same drawing speed with the two different catalysts (Figure 6.2).

From Figure 6.2 it results also that HCl is a better catalyst for the formation of pure silica films under the conditions used, since it produces thicker films via sol-gel deposition. This is due to the fact that acid catalysis promotes a reticulated condensation that increases the density of the solution before the deposition of the films.

Table 6. 5   Mean thickness of the samples on the border step.

Sample name	Thickness (nm)	Sample name	Thickness (nm)
DBTEOS	53 ± 18	HCLTEOS	265 ± 60
DBP1T4	47 ± 23	HCLP1T4	465 ± 13
DBP2T3	74 ± 14	HCLP2T3	270 ± 40
DBP2T2	124 ± 18	HCLP2T2	196 ± 44
DBP3T1	168 ± 14	HCLP3T1	415 ± 20
PMMA	462 ± 20		
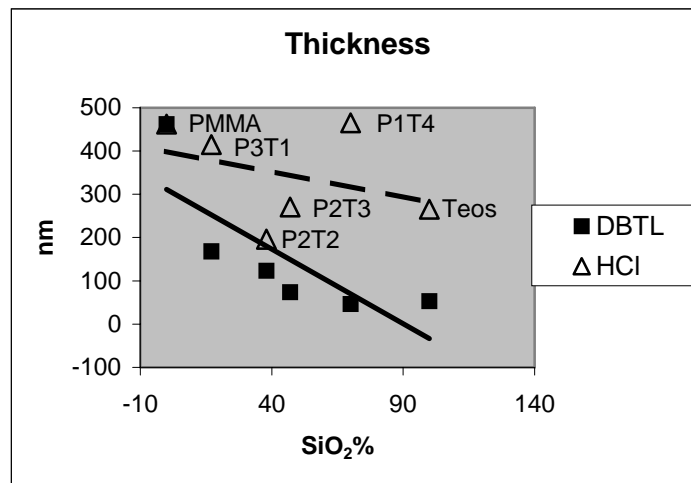
Figure 6. 2   Thickness of the films made with DBTL and HCl catalysis. Withdrawal speed = 0,41 cm/s Trend-lines are shown.
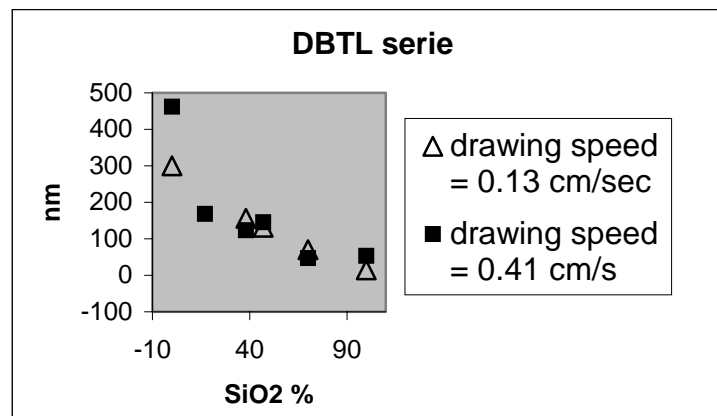
Figure 6. 3   Thickness of the films made with DBTL catalysis at two different drawing speeds.

6.4   Force modulation

The possibility of AFM to scan a surface with a extremely small tip is improved by force modulation which gives the possibility to distinguish the different elastic properties between two materials. This feature of AFM has been used to test the distribution and the dimension of the domains resulting from organic-inorganic phase separation during the formation of nanocomposite materials.

6.4.1 Experimental

Force Modulation pictures were made for every sample on the range 1×1 μm, in order to compare the pictures obtained. For the samples with greater phase separation, however, a scan size of 50×50 μm was chosen, to show the extent of the separation. Force modulation measurements were made using Force Modulation Etched Silicon tips (FESP, spring constant: 1-5 N/m; nominal tip radius of curvature: 5-10 nm). Cantilevers were mounted on a special holder equipped with a piezoelectric bimorph with resonant frequency amplitude of ca. 19 kHz. The experimental parameters used for the acquisition of the Force modulation pictures shown are reported in Table 6.6.

In all the Force modulation-AFM images shown, the scale is set so to associate softer materials with lighter colours.

Table 6. 6   Experimental parameter used in the force modulation experiments

Sample name	Scan size (μ)	Scan rate (Hz)	Z limit (μ)	Drive Amplitude (mV)
DBP1T4	1	1	5,399	200
DBP2T3	1	1,47	5,672	200
DBP2T2	1	1,09	5,399	200
DBP3T1	1	1	5,672	200
HCLP1T4	50	0,690	5,866	200
HCLP2T3	50	0,866	5,672	268,4
HCLP2T2	1	1	5,399	400
HCLP3T1	1	0,808	5,399	300

6.4.2 Results and Discussion

For the hybrid materials prepared, the softer domains are interpreted as PMMA areas. The PMMA domains are considered "softer" than amorphous silica, because of the E-modulus values that can be found in literature (E_{PMMA}= 2,24 − 3,24 GPa, E_{Glass}= 69 GPa) and because of experimental observations. The use of the force modulation technique on soft materials can in fact produce severe damages on the surface. This phenomenon was observed only on the samples with a higher percentage of PMMA and on the film made with PMMA alone. In Figure 6.4 the damage produced during a force modulation scan of 1×1 μm can be seen in a picture obtained zooming out to a 5×5 μm area. In the zoom out picture the drive amplitude was reduced in order not to increase the damages.
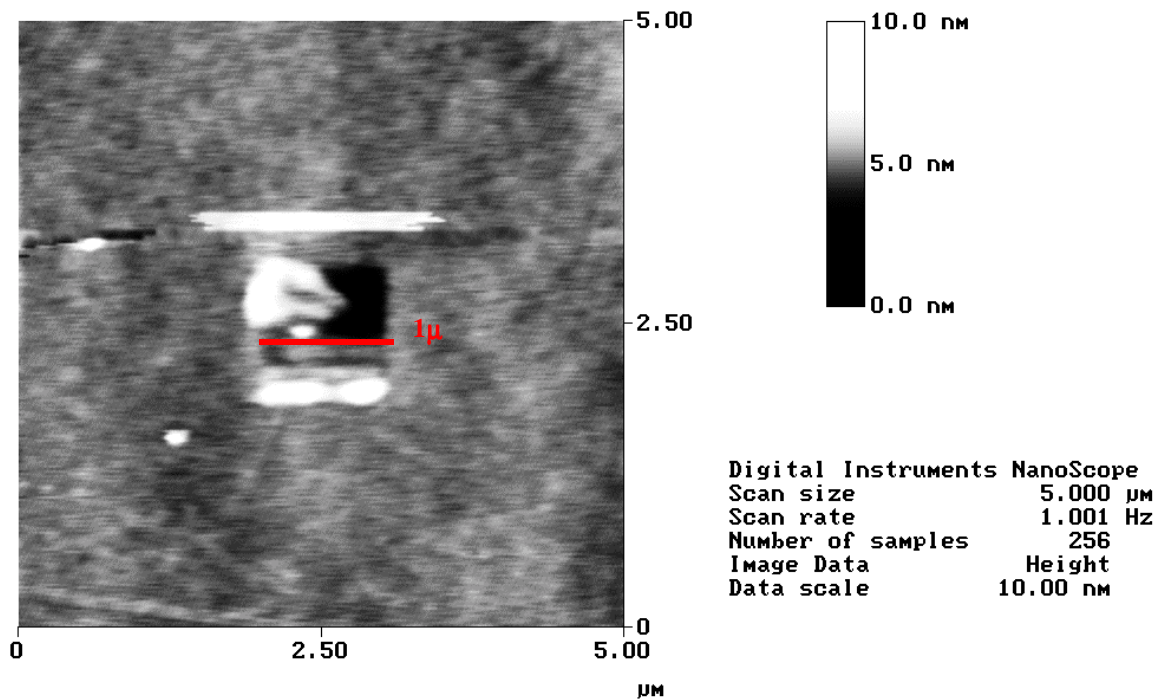
Figure 6. 4   Damaged area due to 1×1 μm force modulation scan on the PMMA film

From the force modulation picture collected, many observations can be drawn. The samples obtained seem, in fact, to follow mainly a spinodal-like decomposition process. This means that there is a spontaneous formation and continuous growth in the unstable parent phase of the other phase. According to the theory of spinodal decomposition, [97-98] phase separation is characterized, in its early stages, by a continuous change in the composition of the phases while the spacing of the morphology of these phases remains constant. Colloid particles of new phases appear only in unstable or metastable oversaturated solutions that posses a sufficient energy to do the work necessary for the formation of new interfaces.

The thermodynamic instability of the system is an indispensable condition for the isolation of a new phase, and the driving force is the change of its free energy. If we consider the dependence of free energy on the state of the system, the necessary condition for the stability or metastability of a fluid phase, derived by Gibbs, is the increase of the

chemical potential of a component with respect to the increasing density of that component. For a system of two components this reduces to the formula: $\left(\dfrac{\partial^2 G}{\partial c^2}\right)_{T,P} > 0$. If this condition is not met, the solution is unstable with respect to continuous composition changes. The limit of metastability, that is, where $\dfrac{\partial^2 G}{\partial c^2} = 0$, is called spinodal.

When the system is outside the spinodal the condition $\dfrac{\partial^2 G}{\partial c^2} > 0$ is valid, whereas inside the spinodal it is $\dfrac{\partial^2 G}{\partial c^2} < 0$, changing the sign of the second derivative of the free energy with respect to concentration. Depending on that, the system follows different mechanism of decomposition at the initial stage and of the isolation of a new phase.

In the metastable region, where $\dfrac{\partial^2 G}{\partial c^2} > 0$, the system can be unstable only to great fluctuation in concentration. This means that the system requires the formation of a nucleus of a definite critical size before to start the decomposition process. Therefore this mechanism of decomposition is called nucleation mechanism, as phase transformation take place through nucleation and the growth of the daughter phase in the parent phase. The composition of the daughter phase does not change with time and the interface between them remains sharp. If the daughter phase has formed, its growth is a result of the diffusion of matter to the surface and of the movement of the surface in the parent phase. Fluctuations larger enough to cause the formation of a new phase nuclei are rare.

If the process follows the nucleation mechanism and the system retains sufficient mobility, the drops of the dispersed phase coalesce and the system separates into two macroscopic phases.

On the other hand, if the system is inside the spinodal it is thermodynamically unstable with regards to fluctuation of the composition, any degree of witch causes phase separation. This means that a binary system that enter the spinodal, immediately separate into two phases. When the system has a low mobility it is capable of entering the region of thermodynamic instability instantly and then passing gradually to the final state of the lowest free energy and the fullest phase separation.

The spinodal decomposition produces in this way a high degree of interpenetration of forming phases at a certain level and morphologically presents two interconnected networks, the mesh size changing little with time and with the increase in the difference in the composition. [99, 100].

In the case of a hybrid made with silica obtained through sol-gel process and a polymer such as polymethylmethacrylate, the resulting materials appear transparent and homogeneous and the phase separation can be seen only on a nanometer scale. For this system the continuous change in composition through the interphase cannot be proved, but the second condition necessary to define a phase separation spinodal, that is its typical interconnected morphology, [101, 102] can be easily seen.

From the Force Modulation images, it can be said that for the DBTL catalysis and for samples obtained with low concentration of Silica for acid catalysis, the system follows a spinodal-like phase separation, with mesh sizes between 40 and 100 nm. (samples: DBP2T2, Figure 6.7; HCLP2T2, Figure 6.11). It can also be observed that acid catalysis promotes a greater phase separation than DBTL under the same conditions. The samples HCLP2T3 (Figure 6.10), and HCLP1T4 (Figure 6.9), for example show phase separation at a larger scale.

This may be due to the slower gelation time of acid catalysis leading to a nucleation-like phase separation. For the sample HCLP2T3 in particular, the phase distribution seems not to follow the topography, which is in this case probably due to the rapid solvent evaporation. For the sample HCLP1T4, the features ranging on a scale from 2 to 10 micrometers, are silica grains embedded in soft PMMA. In this case the process follows a nucleation-like decomposition. Difficulties were encountered in making the force mode analysis of the samples with the higher contents of PMMA, because the surfaces were too soft to be analyzed without damaging them, and the sample HCLP3T1 (Figure 6.12) and DBP3T1 (Figure 6.8) present scratches and artifacts.
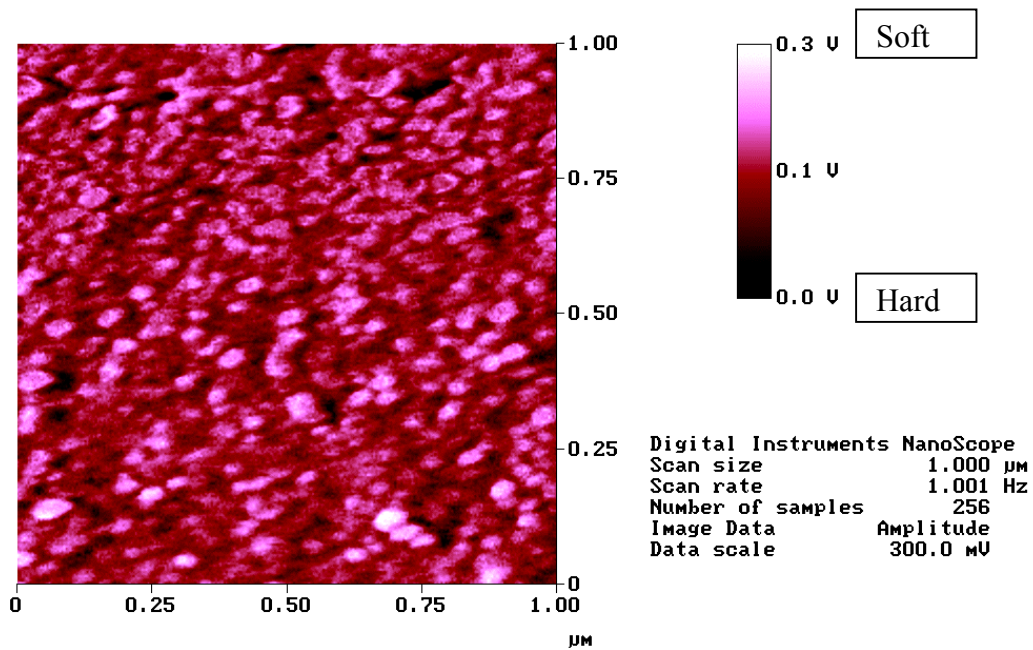
Figure 6. 5   **Sample DBP1T4, force modulation image. Spinodal-like decomposition is shown. Meshes dimension ≈ 30 nm**
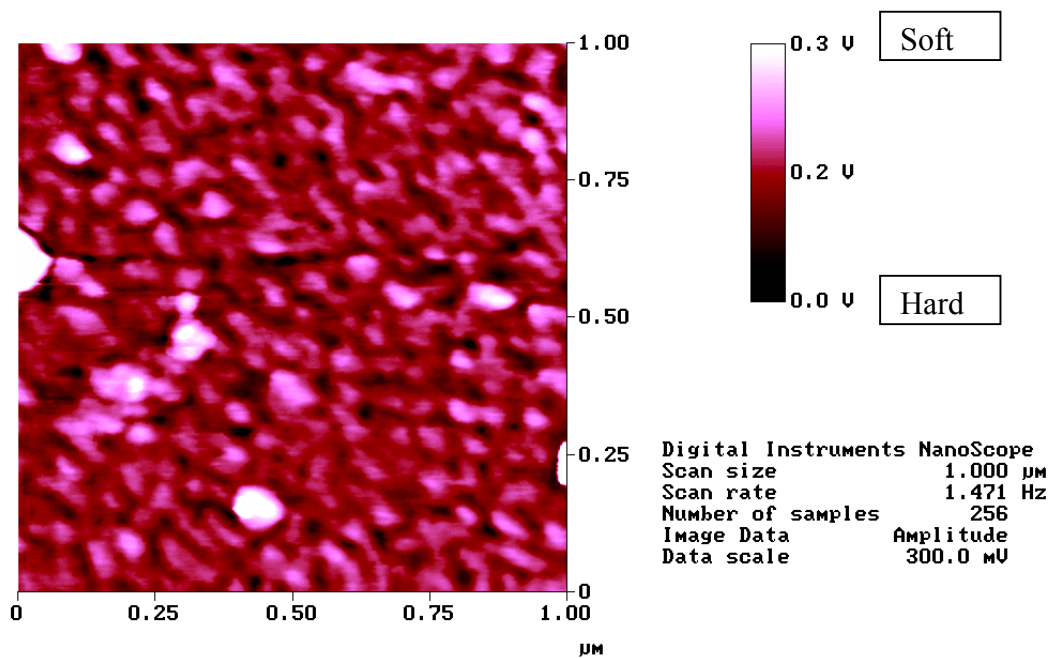
Figure 6. 6   **Sample DBP2T3, force modulation image. Spinodal-like decomposition is shown. Meshes dimension ≈ 40 nm**
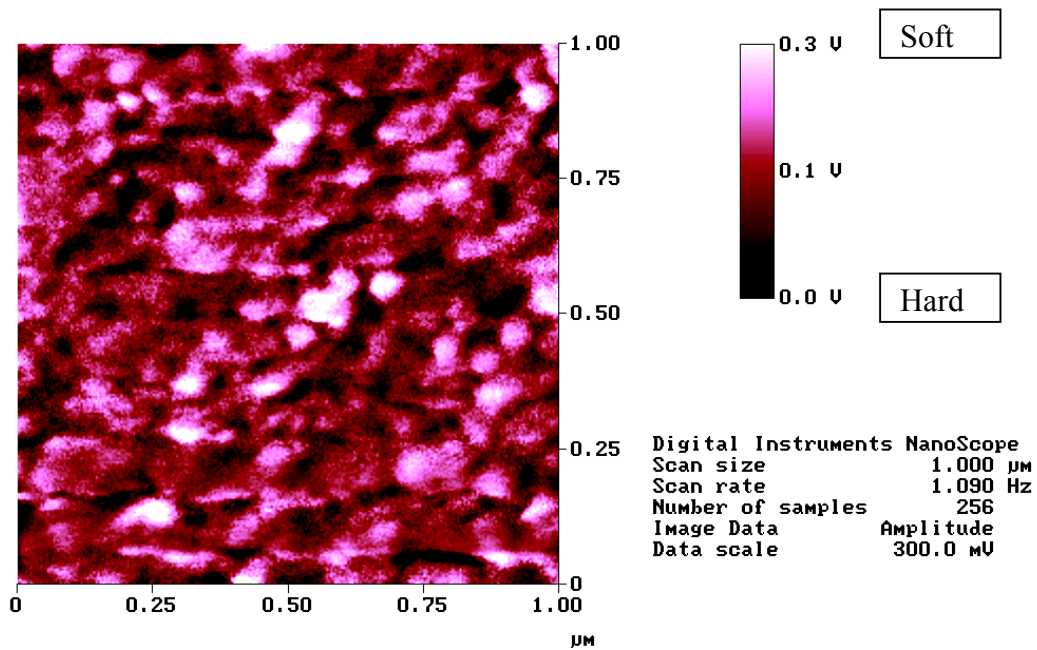
Figure 6. 7   **Sample DBP2T2, force modulation image. Spinodal-like decomposition is shown. Meshes dimension ≈ 60 nm.**
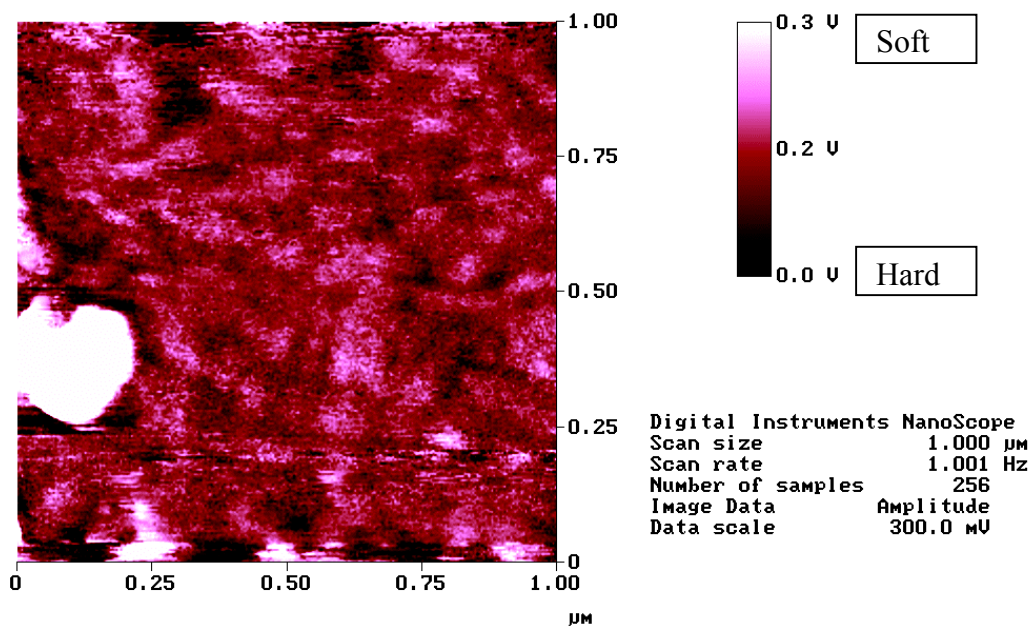
Figure 6. 8   **Sample DBP3T1, force modulation image. Spinodal-like decomposition is shown. Meshes dimension ≈ 50 nm. Sample has been ruined by measurements. The large white spot is an artefact due to the softness of the sample.**
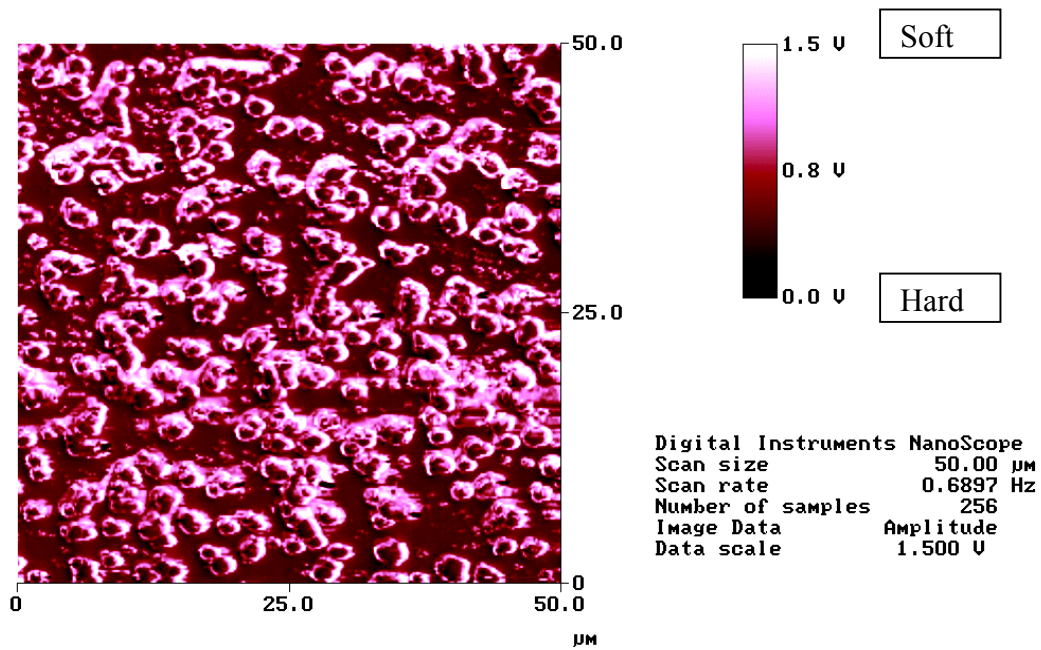
Figure 6. 9   **Sample HCLP1T4, force modulation image. Nucleation-like decomposition is shown on a larger area (50×50 μm). Silica grains have 2-10 μm diameter.**
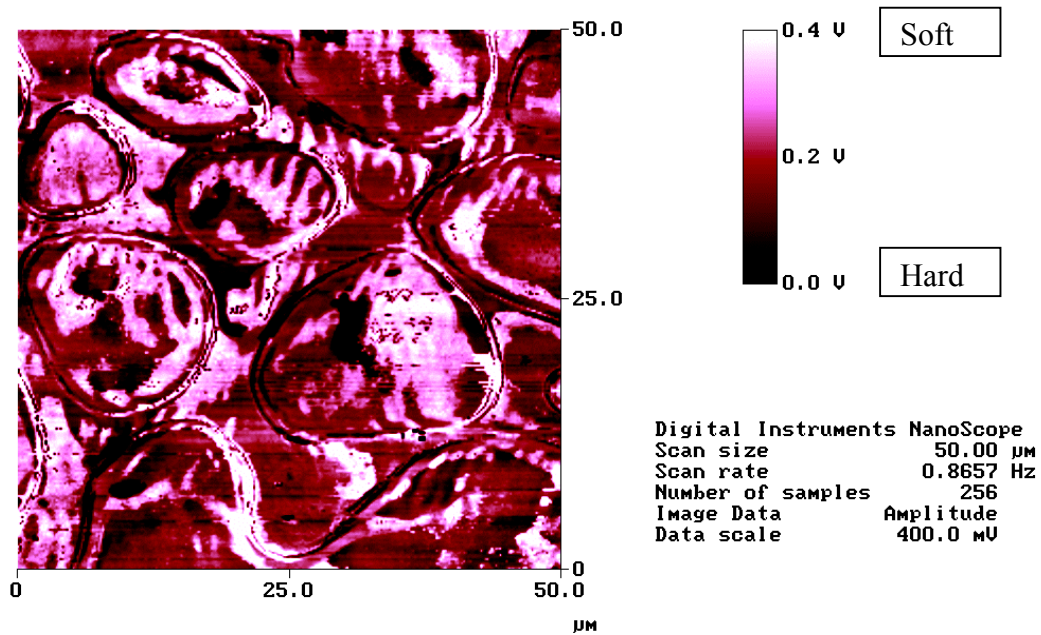
Figure 6. 10   **Sample HClP2T3, force modulation image. Phase separation is shown on a larger area. (50×50 μm).**
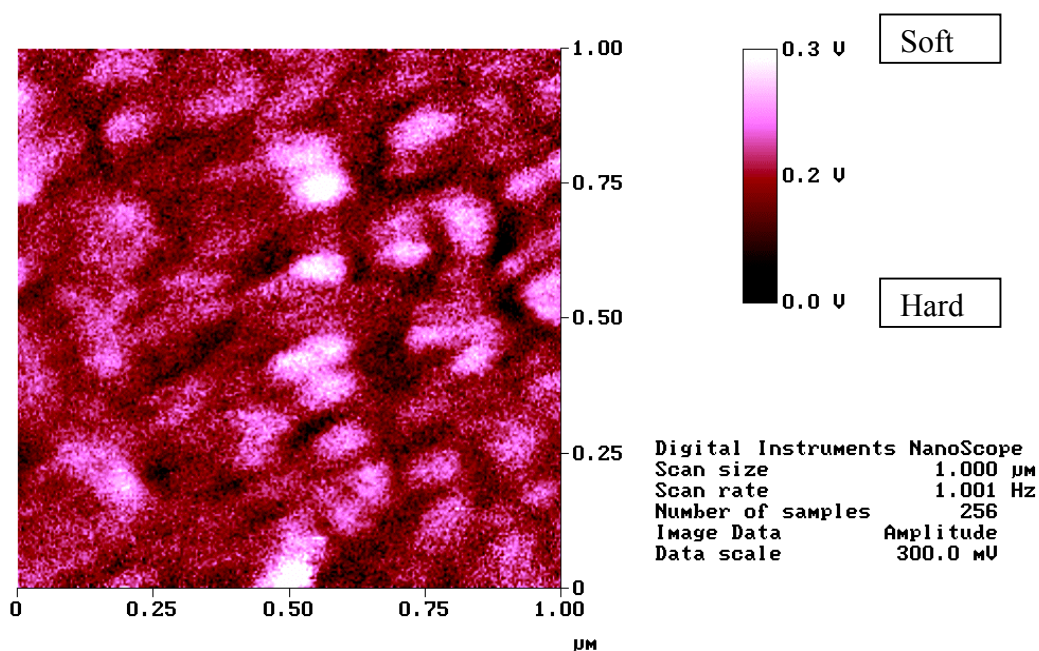
Figure 6. 11   **Sample HCLP2T2, force modulation image. Spinodal-like decomposition is shown. Meshes dimension ≈ 100 nm.**
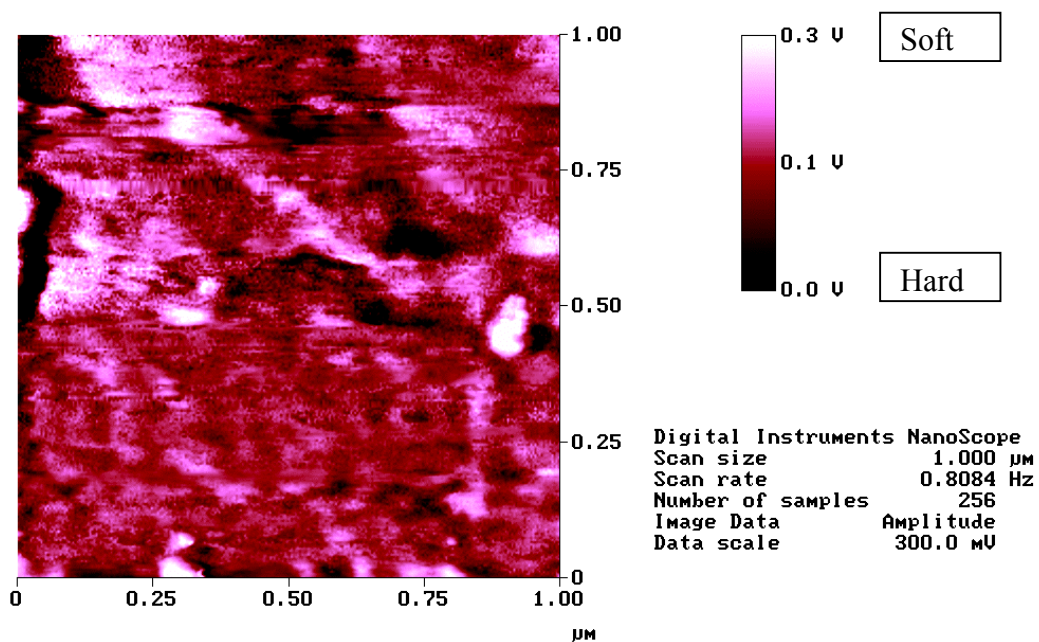
Figure 6. 12   **Sample HClP3T1, force modulation image. Spinodal-like decomposition is shown. Meshes dimension ≈ 40 nm. White large areas are artefacts due to the softness of the sample. Sample has been ruined by measurements.**

6.5 Force plot

Some preliminary experiments were made to understand how to correlate the measured force-distance curves to the elastic and plastic properties of the materials. Many possible approximations are proposed in the literature, to calculate the E-modulus of a material through its force plot, but to obtain a significant value the spring constant of the cantilever and the force applied must be exactly determined. Unfortunately the spring constant is different for any single tip and the force actually applied on the surface is subject to creeps and drifts that makes it difficult to determine a value with a sufficient precision.

For this reason, it was decided to proceed on a relative basis, applying the same procedure to a standard material as well as to the studied films, and using the standard material as a reference. The slope of the force curve on the contact region, normalized to that of the reference material, is used therefore as stiffness parameter, and allows us to compare the stiffness of the films analyzed by AFM.

6.5.1 Experimental

Force plot was performed using diamond coated tips purchased from Park Scientific Instruments. (Diamond Coated Ultralevers, spring constant : 1.6 N/m, cantilever length: 85 μm). The parameters used to collect all the force plots were kept constant in order to reduce the possible variables and are collected in Table 6.7. Z scan start parameters were adjusted to maximize the contact region of each plot. Measurements, after few trial to optimize the z scan start parameter, were made on a fresh area of the surface with a single impulse and only the extending curve was collected. This was made in order to collect data on a new surface and to avoid the eventual damages due to the approaching procedure. Evidences of the damaged produced on the surface of the softer samples come from pictures that can be done on the same surface after the force plot measurements (Figure 6.14) and from the differences between extending and retracting curves. These differences can be seen only at the first impulse, and disappear after few impulses owing to

the permanent deformation of the surface. All the samples were cleaned before the analysis with a flow of dry nitrogen in order to eliminate undesired dust particles from the surface.

Table 6. 7   Parameters used by force plot

tip	Diamond coated ultralevers
Scan modus	contact
Ramp size	300 nm
Cantilever force constant	1.6 N/m
Deflection setpoint	1 V
Z scan rate	9.30 Hz
Reverse rate	9.30 Hz
n° of samples	512

6.5.2 Method calibration

The first step was to test the reproducibility of the stiffness parameter chosen respect to the reference material and to the experimental conditions. The slopes calculated on the contact region of the force plot represent the deflection of the cantilever due to the contact with the surface during the tip-sample displacement. The deflection is given by the movement of the laser lever and for a determinate laser-cantilever-photodiode geometry, can be converted in the effective movement of the cantilever. For this reason a sensitivity factor (nmV^{-1}) must be calculated using a hard material (ideally infinitely hard) prior to extract any parameter.

The hard material used was silicon, used also as reference material. The indentation of the tip is assumed on this material to be negligible in the condition used, and anyway much lower than the indentation in the hybrid materials. The calculation of the sensitivity factor is however affected by the system geometry and introduces a great error.

More reproducible results are given if the slope obtained from the samples is normalized to that obtained for the reference material (silicon). Both values must be acquired in the same session (same system geometry). For this reason all the measurements relative to a set of composites were acquired during the same session, in order to maintain constant all the experimental conditions and the geometry of the system.

For this purpose, after the calibration of the sensitivity factor on the reference material, the laser spot focused at the top of the cantilever was not moved. Fine adjustments and the approaching procedure necessary before any measurement, do not affect significantly this parameter. As can be seen in Figure 6.13 three different approaches have been done on different place of the same surface (cleaned glass surface) after overstressed adjustments of the laser focus. The variation of the slope is almost within the error limit and for the purpose of comparison between materials is not relevant.
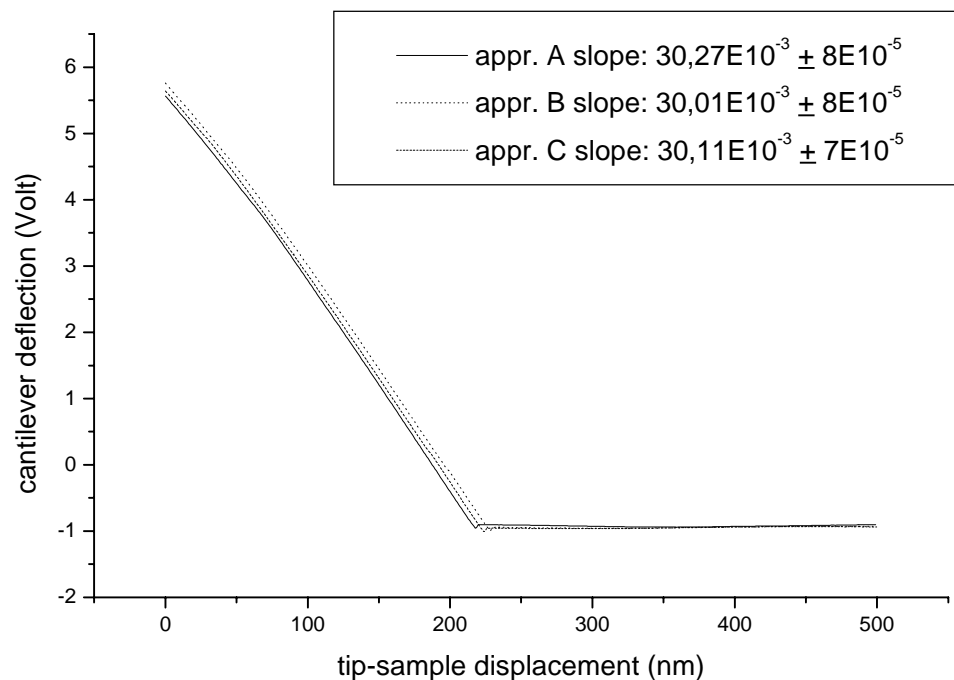
Figure 6. 13 **Force plot made after different approaches on a glass surface.**
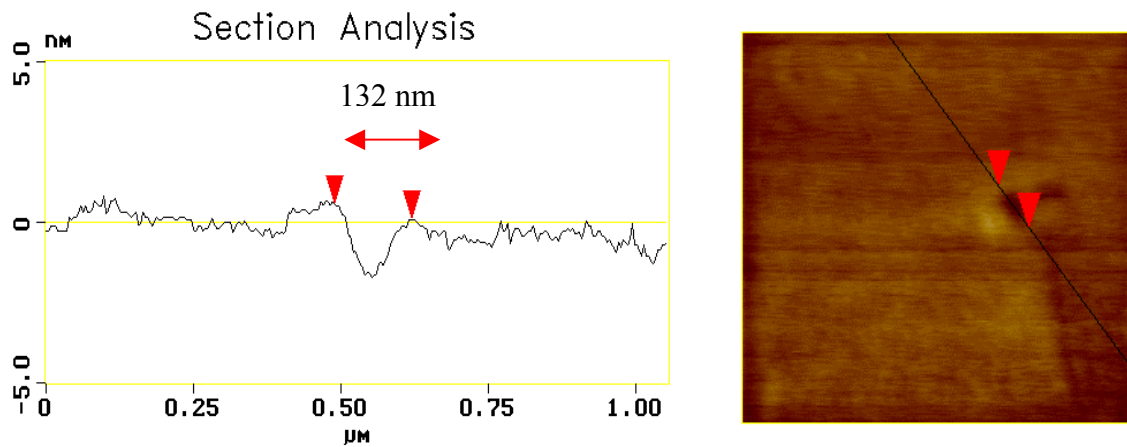
Figure 6. 14 **Section of the indentation produced on PMMA surface by a load of ca. 0,25 μN**

To check which kind of influence the tip exerts on the surface, some indentation experiments were done. [81, 82].

In Figure 6.14 the section of indentation produced on the PMMA sample with the force plot of Figure 6.15 is shown. The normal load applied is ca. 0,25 μN , and can be calculated from the force plot. The cantilever deflection result to be in fact 155 nm, and the cantilever spring constant is 1,6 N/m. The indentation was produced by a single run of the force plot on a new surface and then scanned with the same tip. The contact area between the tip and the surface has a diameter bigger than 100 nm and for this reason the measurements done with the force plot are considered not affected from the single grains of the two phases of the nanocomposite materials, but are the mean value between at least some of them. This ensures that the values obtained are not influenced by the position on the surface.
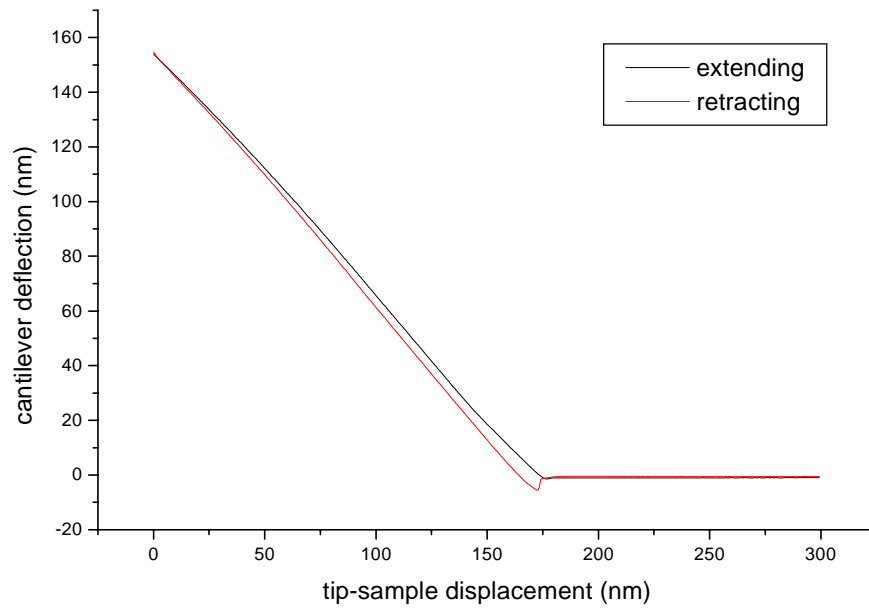
Figure 6. 15   Force plot of the indentation experiment on PMMA sample
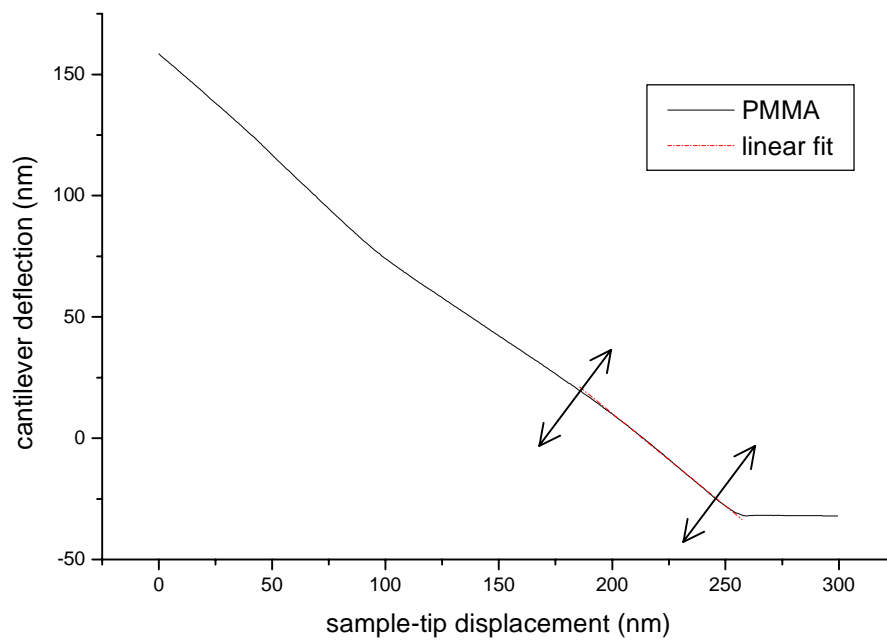
Figure 6. 16   Force plot on PMMA film. The linear fit is calculated on the part shown by the arrows.

6.5.3 Results and discussion

Slopes have been calculated fitting the first part of the contact region of each curve, in order to obtain more information about the elastic properties of the samples. The samples are in fact prepared as thin films, and after the first few nanometers the indentation of the tip can produce plastic deformations of the material or even meet the substrate and assume the same slope of the reference material. An example of the line fitting used to calculate the plots slope is shown in Figure 6.16.

The results for the DBTL and HCl series are reported in Figure 6.17 and Figure 6.18. The samples HCLP1T4 and HCLP2T3 were not analyzed because of their larger phase separation.
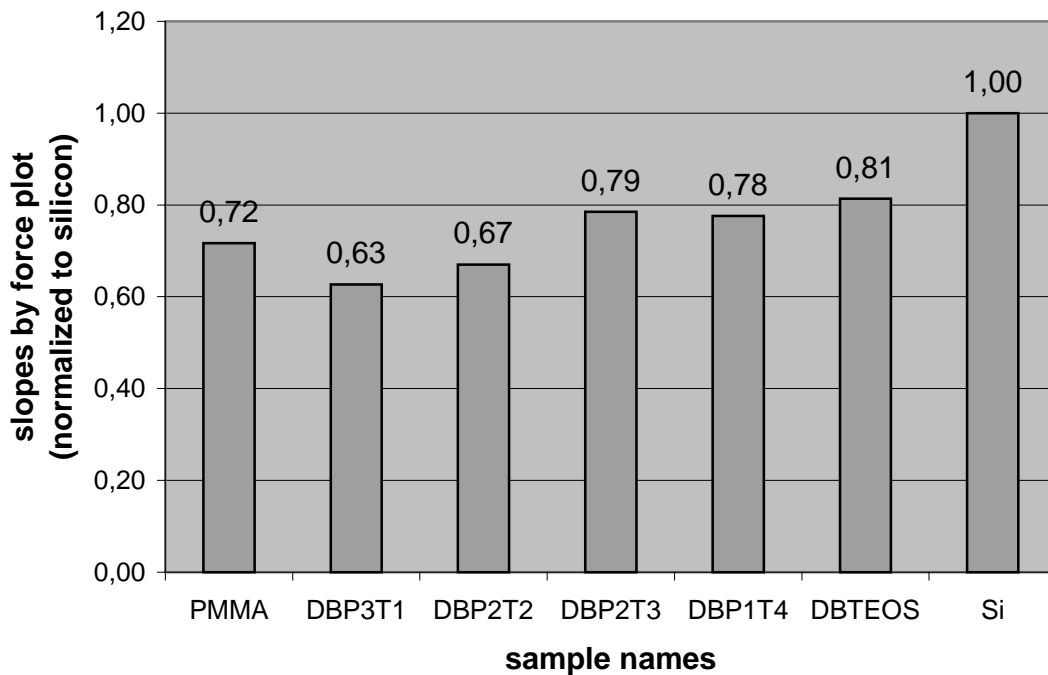
Figure 6. 17   Force plot analysis of the stiffness of the DBTL series.
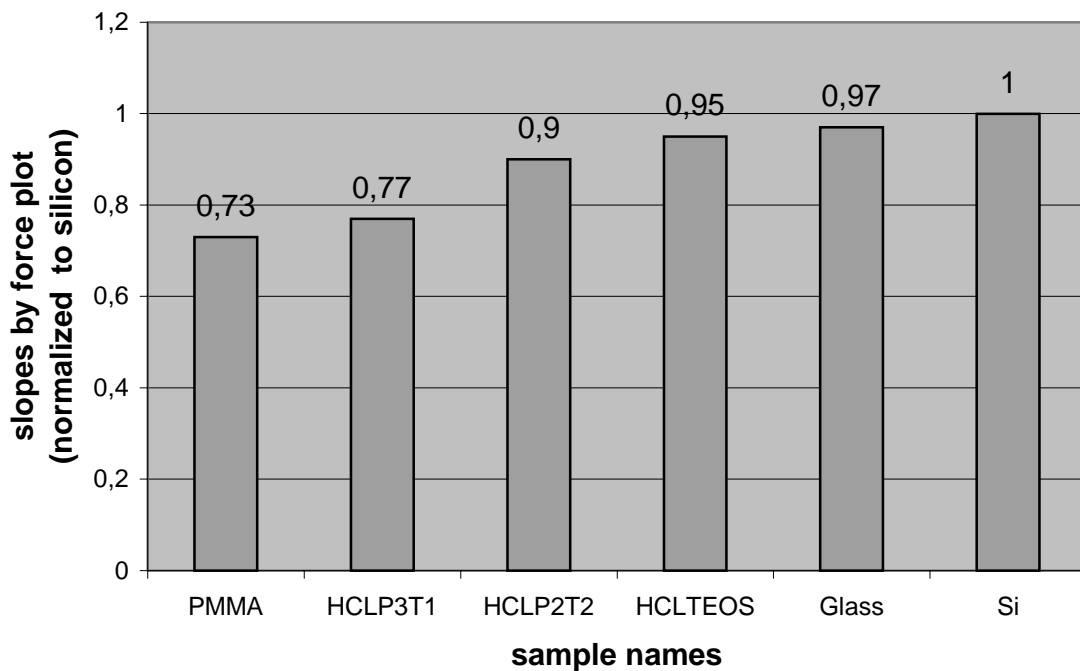
Figure 6. 18   Force plot analysis of the stiffness of the HCL series.

Both the DBTL and HCl series show a stiffness dependence on the composition, and the stiffness decreases as the percentage of PMMA in the composites increases. The first difference between the two series is given by the fact that the composites made with acid catalysis seem to be harder than their correspondent made with DBTL. Furthermore in the series prepared with DBTL as catalyst the samples DBP2T2 and DBP3T1 result to be softer than the PMMA alone. This minimum can be explained with the help of the information obtained by IR spectroscopy (Chapter 7). In the DBTL catalysis, in fact, the presence of H-bonds between the two phases is smaller than in the samples obtained with acid catalysis. This means that, even if with a good interpenetration, the two phases are less strong bound one to the other. For this reason the composites made with acid catalysis that result homogeneous, result also to have a higher stiffness parameter than their DBTL homologues.

6.6 Conclusions

The analysis made on the two set of samples demonstrates that AFM is a useful tool to analyze organic-inorganic hybrid materials. New information have been collected about phase separation at a nanometer scale, and macroscopic phase separation has been confirmed to happen under certain conditions.

The stiffness of the samples has also been tested on a scale comparable to that of the phase separation. The method used is limited to a comparative analysis, but useful information have been achieved in order to understand the stiffness dependence on the Si/PMMA ratio of the samples and on the catalyst employed. In particular a comparison between acid catalysis and DBTL catalysis for the sol-gel process of a solution of TEOS, can't be found in literature.

The clear dependence of the properties of the resulting materials that have been measured from the composition of the starting solutions, confirms the utility of this analysis method to test the effect of the compositional variations.

Chapter 7

Interaction between the two phases

7.1   Introduction

A crucial role in the formation of a hybrid material is played by the interaction occurring between the two phases. The existence of such interaction and its nature can modify the process of phase separation making more stable a homogenous mixture between the two materials and promoting the growth of two interpenetrating networks.

The quality of the interactions between the organic and inorganic part of the new material and the effective presence of both in the films produced was checked by IR analysis. Furthermore, IR spectroscopy allows us to reach a better comprehension of the relationship between the organic and inorganic part of the composite materials.

7.2   FT-IR analysis

The two materials used in this work to produce hybrid nanocomposites, namely PMMA and silica gel, interact through a H-bond between carboxyl groups of PMMA and hydroxyl groups still present on the amorphous silica gel. The amount of this interaction can be evaluated thanks to the shift of the characteristic C=O peak due to the formation of H-bonds [103-106].

Attention was also paid to understanding the role of the catalysis on the presence of H-Bonds between PMMA and silica. Although it is well known from the literature that acid catalysis produces a gel with a higher number of OH groups, scarce information is available on the role of the catalyst that is mainly used for natural stone conservation, i.e. DBTL (dibutyltin dilaurate). This effect due to the catalyst can be therefore studied, even if only qualitatively, with the IR spectroscopy.

7.3   Experimental

To obtain the same condition used for the film analyzed with AFM, the samples were prepared as thin films on KBr disks, by the dip coating technique, with a single immersion. Measurements were also done on films made from the starting materials, as references. The mixtures between the two components and the film deposition were made 24h after their preparation, to let the silica condensation to take place. Films were prepared also after 48h, to check if the process still goes on after one day. Some preliminary samples were prepared to test the possibility to analyze thin films with FT-IR spectroscopy. Films were prepared also using isopropanol as solvent for the TEOS solution.

The samples used for the peak deconvolution were prepared as described before, and the mixture between PMMA and TEOS were made with the same [Si]/[MMA] ratios used for the other analysis (see chapter 5).

7.4   Results and discussion

Both the samples prepared with the two starting materials alone (PMMA and SILICA) present a IR spectrum characteristic of these compounds, which confirms the effective deposition of the desired films. On the samples obtained starting from mixed solutions, both the peaks due to PMMA and silica are present, confirming the contemporary deposition of the two materials to form a composite. Samples prepared after 48 hours present no different spectra than those prepared after 24 hours, confirming the choice of one day as the right time lapse for the condensation of the silica gel.

All the spectra made on the composite materials present a peak at 1073 cm^{-1}, associated with Si-O-Si stretching, but more interest is given by the peak at 1730 cm^{-1} associated with the C=O stretching of the carbonyl groups present on the PMMA polymer [107].

It is possible to observe that on composite materials this peak becomes broader and undergoes a shift at lower energies due to a shoulder between carboxyl groups and silica hydroxyl groups (Figure 7.1).

Samples were prepared with silica made with both acid and DBTL catalysis, and a first sight shows that an higher amount of hydroxyl groups (3400 cm^{-1}) in the acid catalyzed films brings to a more evident shift on the C=O peak. Since the amount of water was in excess and can be considered constant in all the solutions, the C=O peak shift due to an higher OH- groups amount can be attributed to the different catalysis. This confirms the idea that DBTL is an efficient catalyst for the Si-O-Si bonds formation [93, 94] leaving less free OH groups respect the simple acid catalysis. (Figure 7.2). This idea is confirmed also by the simple observation that the gelation time for bulk materials is much shorter with DBTL as catalyst than with HCl as described in chapter 5.

No differences have been observed at the FT-IR analysis between the films prepared starting with solutions containing TEOS in THF or in isopropanol. This is due to the fact that the peak shift observed gives only qualitative information about the formation of H-bonds, and possible differences in the resulting systems result too small to be detected.
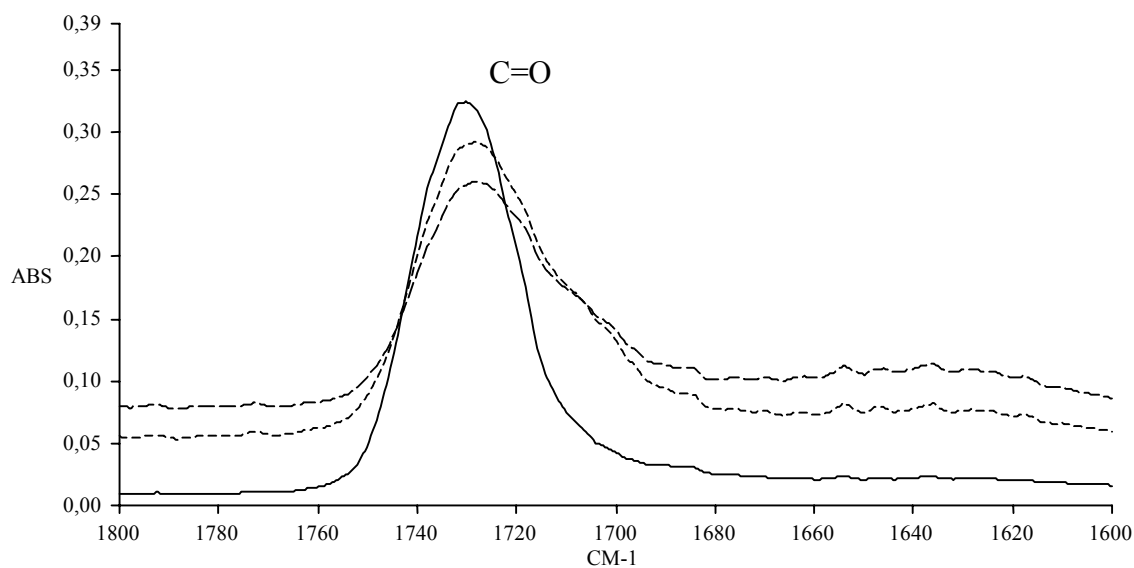
Figure 7. 1   **FT-IR spectra. Solid line: PMMA, Dot line: 2g PMMA 10% in THF + 2ml TEOS(HCl) 1M in isopropanol, Dash line : 2g PMMA 10% in THF + 3ml Teos(HCl) 1M in isopropanol.**
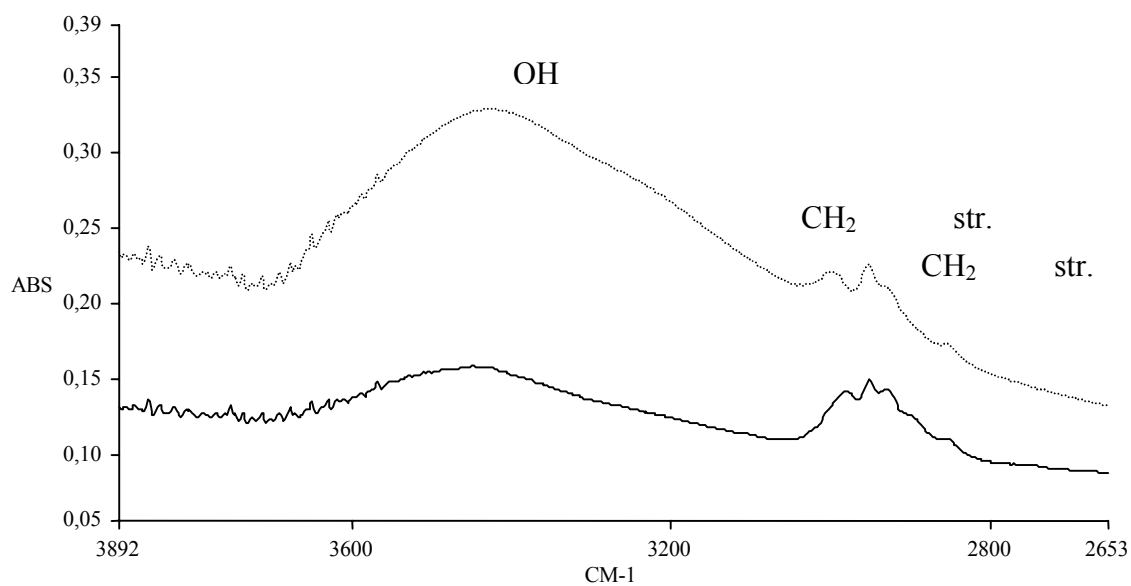
Figure 7. 2   **FT-IR spectrum, Dot line: 2g PMMA 10% in THF + 3ml Teos(HCl) 1M in isoprop. Solid line: 2g PMMA 10% in THF + 3ml Teos(DBTL) 1M in isoprop.**

Another relevant observation is that the amount of the peak shift is also due to the relative concentration of the two components. The higher the concentration of silica respect to PMMA, the greater the C=O peak shift (Figure 7.1, 7.2).

To quantify these observations, a deconvolution of the peaks was made, using a gaussian peak fitting. The results show in all the samples the presence of the two expected peaks at 1730 cm^{-1} and at 1710 cm^{-1}, within the errors due to the fitting. (Figure 7.3). The parameter R_A was calculated as the ratio between the areas of bounded and free carbonyl groups peaks.

[R_A= (area bounded CO peak at 1710 cm^{-1}) / (area free CO peak at 1730 cm^{-1})].
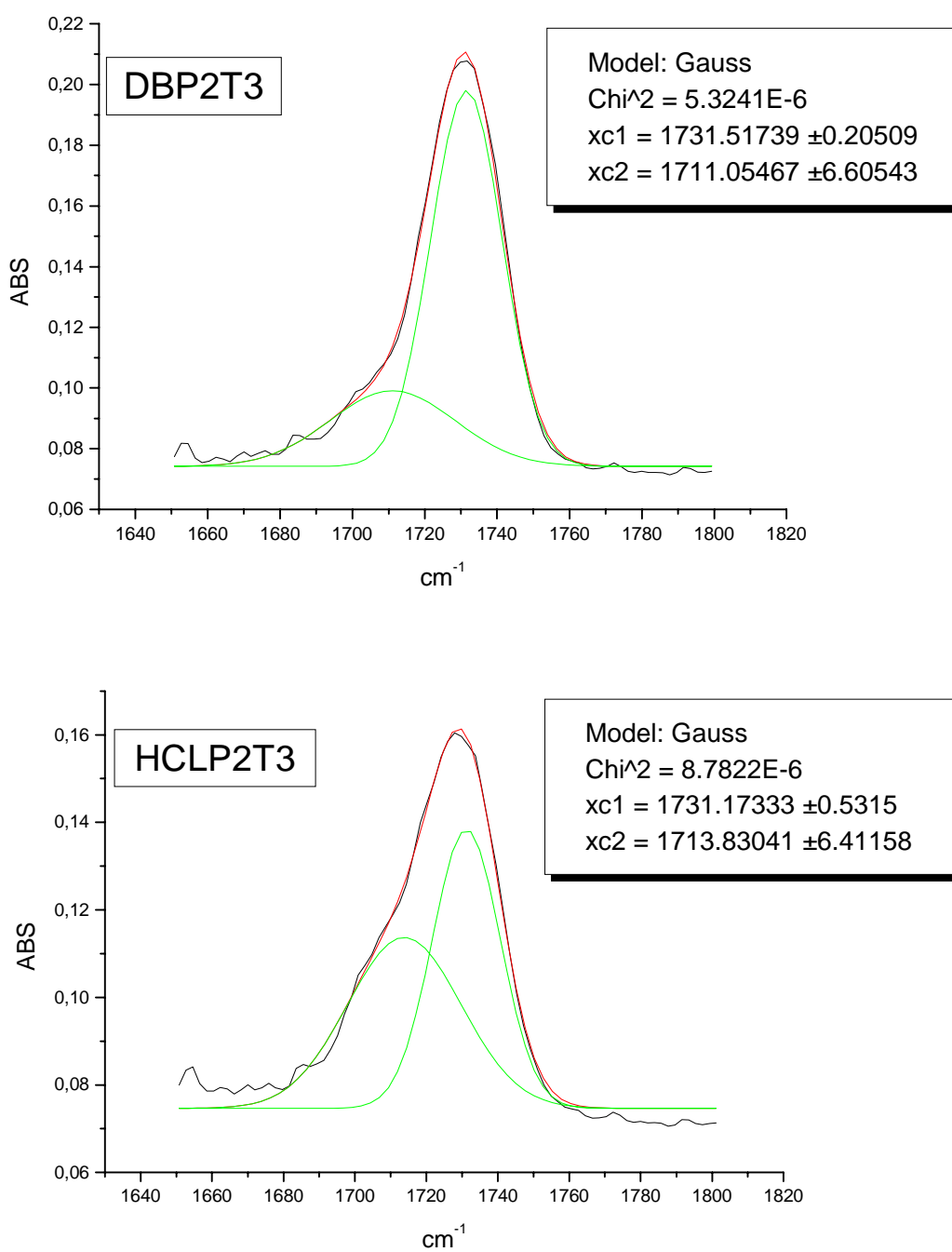
Figure 7. 3   **Examples of deconvolution for the C=O stretching peaks, samples made by acid catalysis (HCLP2T3) and by DBTL catalysis (DBP2T3).**

The ratio between the areas of the two deconvoluted peaks shows two different trends for the two catalysts employed. As expected, with acid catalysis the parameter R_A grows as the silica/dimethylmethacrylate molar ratio increases. On the other hand, when DBTL is used, R_A turns out to be relatively low and reaches a maximum at a silica/methylmethacrylate ratio, which corresponds to the composites that show a spinodal-like phase separation on AFM analysis (Figure 7.4). This observation leads to the hypothesis that an amorphous silica gel obtained by acid catalysis contains more OH groups than that obtained by DBTL catalysis. The composites formed with the DBTL catalysis, however, also achieve a good homogeneity most likely due to the shorter gelation time.
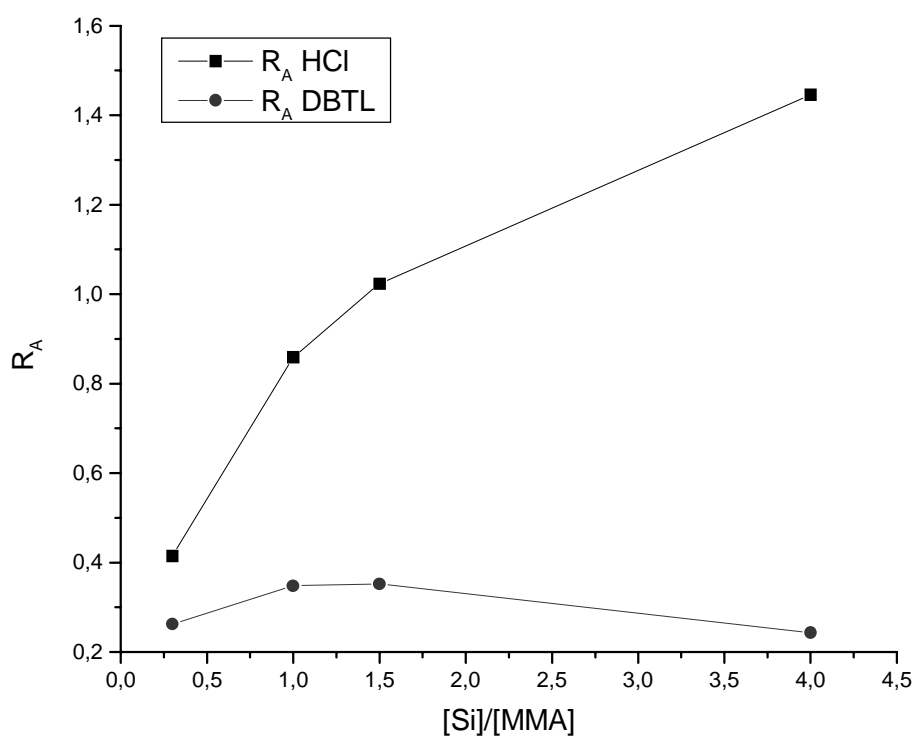
Figure 7. 4   **R_A plotted against the [Si]/[methylmethacrylate] molar ratio**

Samples were made also with PEOX (polyethyloxazoline) as organic part of the composite materials, [24] to test the effect of the presence in the polymer of a better hydrogen acceptor group than C=O in the H-bond formation. In the PEOX polymer this is

an amidic group, which should promote the interaction between the two phases. As for the PMMA/silica composite, a shift is observed on the C=O peak (1636 cm^{-1}), and a shoulder is now evident also on the OH broad peak (Figure 7.5, 7.6). However, the expected increase of the peak shift due to the amidic group is not observed or result to be too small for this method. The PEOX/silica composite shows a different time dependence respect to the PMMA/silica one, since the film made after 48h shows an higher peak shift than the one made after 24h.
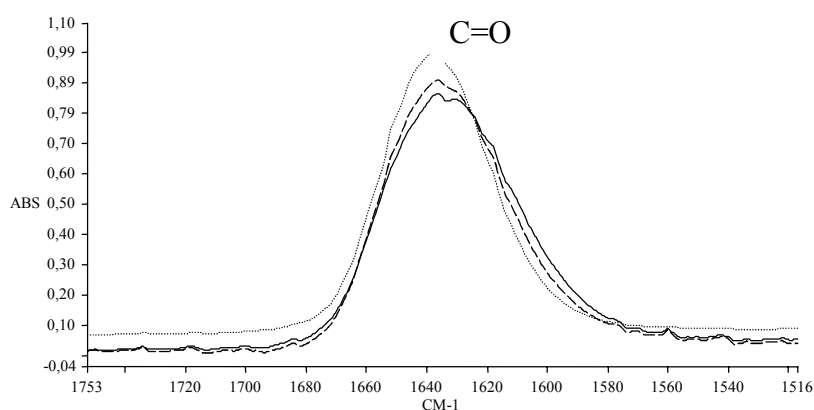
Figure 7. 5   **FT-IR spectrum.**
Dot line: PEOX 10% wt in isoprop.
Dash line: 2g PEOX 10% wt. In isoprop.+3ml TEOS(DBTL) 1M in isoprop. After 24h
Solid line: 2g PEOX 10% wt. In isoprop.+3ml TEOS(DBTL) 1M in isoprop. After 48h
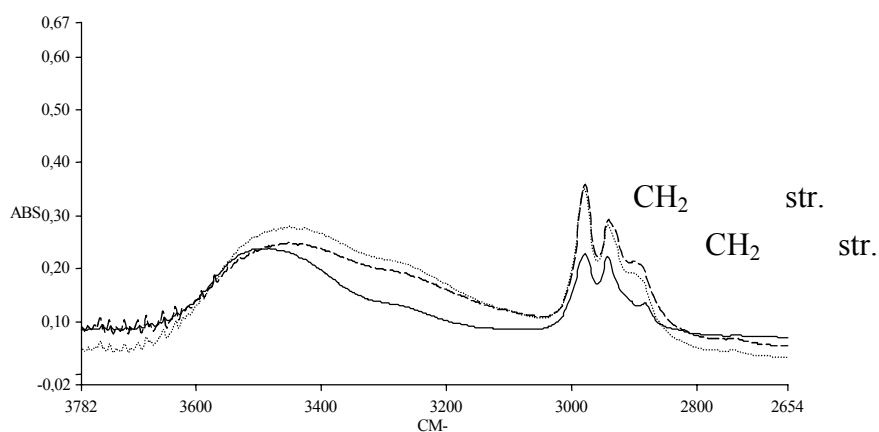
Figure 7.6   **FT-IR spectrum.**
Solid line: PEOX 10% wt in isoprop.
Dash line: 2g PEOX 10% wt. In isoprop.+3ml TEOS(DBTL) 1M in isoprop. After 24h
Dot line: 2g PEOX 10% wt. In isoprop. + 3ml TEOS(DBTL) 1M in isoprop. After 48h

7.5   conclusions

Despite the higher number of H-bonds that are formed by the acid catalysis, the evolution of the system in thin films formation seems not to depend on that. In fact composites made with DBTL as catalyst result to be from AFM observation, more homogeneous than the others. This is surely due to the fact that on thin film formation, kinetic phenomena are more important than the weak interaction due to Hydrogen bonds, and even if these bonds can play a role also in the kinetic, the resulting system can be far away from thermodynamic equilibrium [102]. The mobility of the two separating phases decreases in fact dramatically during the rapid evaporation of the solvent, and other parameters control the resulting morphology of the system. In this case the nucleation and spinodal separation theory can help us to understand the behavior of the two phases in the thin films formation process.

Chapter 8

Properties on a micro- and macro-scale

8.1   Introduction

In the previous chapters the characteristics and the properties of the hybrids materials used for natural stone protection and consolidation have been tested. A complete study of these materials must anyway take account of their behaviour in the real stone-hybrid material system. Even if the materials studied here are a simplified model of the commercial products actually used, it was considered convenient to test the behaviour of ours materials as consolidants, with methods similar to those used in the practice.

For this purpose a mixture of sands with different corn size was consolidated in disk-shaped forms through soaking with the same solutions used for the formation of the films.

The effectiveness of the treatment was tested determining the biaxial flexural strength rupture modulus and the E-modulus of the so formed disks. SEM and polarization microscopy were used to control the effective distribution of the consolidant material between the sand grains.

8.2   Sample preparation

Consolidant materials are usually tested by direct application on natural stone samples, whose properties are controlled before and after the application of the product. Many applications are required to notice an effective consolidation. Furthermore the properties of the different variety of stones (i.e. porosity, chemical composition and structure of the mineral) influence greatly the consolidation process.

For these reasons it was decided to use quartz sand to simulate a completely loosened sand stone. In this way the consolidation of the sand can be attributed completely to the action of the materials used and to the interaction between the grains and the forming composite. It was decided to use a mixture of sands with a wide corn-size distribution, in order to increase the contact surface between grains. In such a way the formation of films between the grains results maximized and a more effective consolidation can be observed.

Two types of sands were used with different corn size distribution: DORTSILIT NR 9H and DORTSILIT 6400, purchased from Dorfner. The properties and the corn distribution of the two sands are reported in Table 8.1 and 8.2.

Solutions of TEOS and PMMA were prepared as described in Chapter 5, 24h before to be mixed with the sand in order to let TEOS condensation to take place. Preliminary tests were made using only the sand DORTSILIT NR9H and the samples obtained resulted fragile and crumbled. These samples were prepared simply soaking the sand with the solutions and after drying they were analyzed by polarization microscopy.

A mixture composed of 75 % wt. of DORTSILIT NR 9H and of 25 % wt. of the fine sand DORSILIT 6400 was prepared in order to have a wide mesh size distribution. Sands were weighted and stirred until a homogenous mixture could be seen. 16 g. of this mixture were weighted into petridishes with a diameter of 6 cm. The internal part of the petridishes were covered with aluminium foil in order to simplify the extraction of the disks after their hardening. The sand has been levelled and slightly pressed to form a disk as regular as possible. 4,5 ml of the previously prepared solutions were poured gently on the sand and the samples so formed were let dry at ambient conditions. After few days solid disks could be extracted and the aluminium foil was removed. 5 samples for every solution were prepared and mean diameter and thickness of each sample were measured (Table 8.3)

A single application treatment was chosen in order to avoid interferences of the following treatments with the first one. The acrylic resin for example can be solved by further application of the solvent while the silica gel can not. In this case the proportion of the two components of the solution in the second treatment can be altered and loose any possible relation with the materials analyzed in the first part of this work.

DORTSILIT 6400

Oxide:	SiO$_2$	Al$_2$O$_3$	Fe$_2$O$_3$	TiO$_2$	K$_2$O	Na$_2$O	CaO	MgO			Lost on ignition:
MA %	98,9	0,45	0,019	0,04	0,15	0,01	0,02	0,01			0,20
Analysis according to DIN 51001 with XRF											

Mineralogical composition				**Granulation**	
				(ALPINE LUFTSTRAHLSIEB, SEDIGRAPH 5100)	
Quartz	98	MA.%			MA.%
Feldspar	1	MA.%		> 71 µm	3
others	1	MA.%		63 - 71 µm	4
Physical Data				40 - 63 µm	21
				20 - 40 µm	25
Whiteness R457abs	78	%		10 - 20 µm	21
Spec. Surface	0,89	m2/g	Acc.to BET(DIN 66132)	4 - 10 µm	15
Density	2,63	g/ml	DIN ISO 787, Teil 10	< 4 µm	11
Bulking volume	0,93	g/ml			
Ramming volume	0,67	ml/g	DIN ISO 787, Teil 11	Residue > 71 µm max. 5 MA.%	
Oil Absorption	19	g/100g	DIN ISO 787, Teil 5	Mean grain size: 21 µm	
pH	6 - 8		DIN ISO 787, Teil 9		
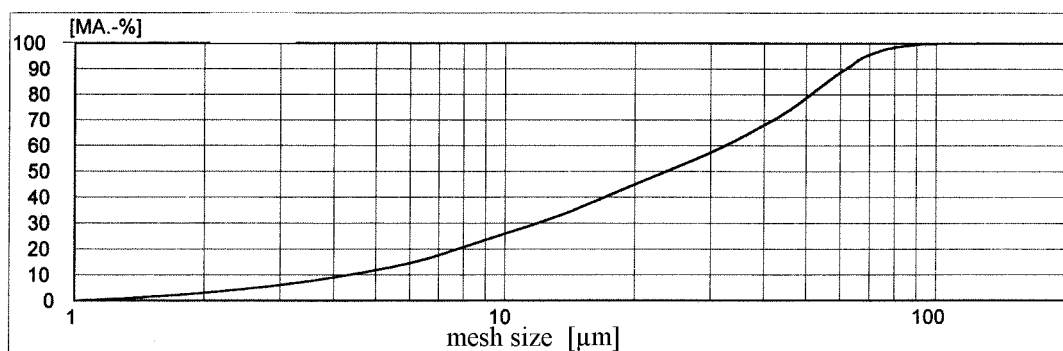
Table 8. 1 **Physical and mineralogical data of sand DORTISLIT 6400.**

Mean grain size: 21 µm

DORTSILIT NR. 9 H

Oxide:	SiO$_2$	Al$_2$O$_3$	Fe$_2$O$_3$	TiO$_2$	K$_2$O	Na$_2$O	CaO	M O	Lost on ignition
MA.%	97,8	1,07	0,04	0,24	0,30	0,04	0,02	0,02	0,39

Mineralogical composition				granulation
				(ISO 3310 T1)
Quartz		95,9	MA.-%	> 0,8 mm trace
Kaolinite		1,6	MA.-%	0,63 - 0,8 mm 1 MA.-%
K-Feldspar		1,8	MA.-%	0,5 - 0,63 mm 2 MA.-%
Na-Feldspar		0,3	MA.-%	0,4 - 0,5 mm 9 MA.-%
Others		0,4	MA.-%	0,315 - 0,4 mm 22 MA.-%
				0,2 - 0,315 mm 43 MA.-%
				0,1 - 0,2 mm 22 MA.-%
				< 0,1 mm 1 MA.-%
Physical Data				
humidity	Ca.6	MA -%	DIN ISO 787, Teil 2	
fire dried	< 1	MA -%		
Density	2.65	g/ml	DIN ISO 787, Teil 10	Mean grain size: 0,28 mm
Bulk density	1.40	g/ml		
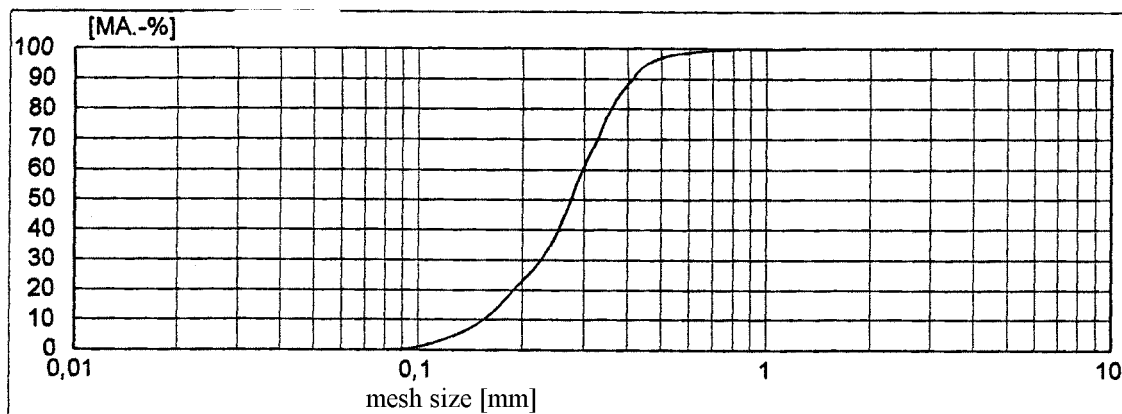
Table 8. 2   **Physical and mineralogical data of sand DORTISLIT NR 9 H.**

Mean grain size: 0,28 mm

Table 8. 3   Diameter and thickness of the samples made by consolidated sand

sample name	mean diameter (mm)	mean thickness (mm)	sample name	mean diameter (mm)	mean thickness (mm)
TEOS HCL A	44,32	5,73	TEOS DBTL A	45,33	5,45
TEOS HCL B	47,22	5,77	TEOS DBTL B	47,25	5,72
TEOS HCL C	47,10	5,62	TEOS DBTL C	47,40	5,53
TEOS HCL D	47,52	5,82	TEOS DBTL D	47,48	5,60
TEOS HCL E	46,87	5,58	TEOS DBTL E	47,35	5,55

sample name	mean diameter	mean thickness	sample name	mean diameter	mean thickness
HCLP1T4 A	45,72	5,63	DBP1T4 A	44,58	5,55
HCLP1T4 B	47,20	6,08	DBP1T4 B	47,27	5,67
HCLP1T4 C	47,23	5,82	DBP1T4 C	47,40	5,70
HCLP1T4 D	47,45	5,65	DBP1T4 D	47,17	5,68
HCLP1T4 E	47,00	5,55	DBP1T4 E	47,28	5,70

sample name	mean diameter	mean thickness	sample name	mean diameter	mean thickness
HCLP2T3 A	46,20	5,40	DBP2T3 A	46,00	5,60
HCLP2T3 B	47,48	5,80	DBP2T3 B	47,37	5,78
HCLP2T3 C	47,30	5,47	DBP2T3 C	47,40	5,57
HCLP2T3 D	47,05	5,75	DBP2T3 D	47,17	5,60
HCLP2T3 E	47,37	5,57	DBP2T3 E	47,15	5,77

sample name	mean diameter	mean thickness	sample name	mean diameter	mean thickness
HCLP2T2 A	46,97	5,72	DBP2T2 A	46,42	6,15
HCLP2T2 B	47,12	5,63	DBP2T2 B	47,33	5,55
HCLP2T2 C	47,40	5,53	DBP2T2 C	47,37	5,62
HCLP2T2 D	47,42	5,57	DBP2T2 D	47,25	5,60
HCLP2T2 E	47,32	5,73	DBP2T2 E	47,33	5,65

sample name	mean diameter	mean thickness	sample name	mean diameter	mean thickness
HCLP3T1 A	46,55	5,55	DBP3T1 A	46,02	5,78
HCLP3T1 B	47,27	5,87	DBP3T1 B	47,43	5,62
HCLP3T1 C	47,22	6,05	DBP3T1 C	47,37	5,62
HCLP3T1 D	47,48	5,60	DBP3T1 D	47,05	5,63
HCLP3T1 E	47,38	5,47	DBP3T1 E	47,15	5,62

sample name	mean diameter (mm)	mean thickness (mm)	sample name	mean diameter (mm)	mean thickness (mm)
PMMA A	45,8	5,63	PMMA D	47,13	5,55
PMMA B	47,25	5,77	PMMA E	47,12	5,68
PMMA C	47,17	5,57			

8.3   Polarization microscopy

Through the polarization microscopy it is possible to distinguish the sand grains from the consolidating materials. The sand corns have, in facts, a crystalline structure that interacts with the polarized light and transmits or stops it depending on the incident angle. The amorphous silica formed from the sol-process and the PMMA polymer, on the other side, results dark under polarized light at every angle. The comparison between the photos done on the same area with and without polarized light allows us to distinguish the sand grains from the amorphous material formed through the consolidation process. The two photos were taken choosing an angle where the higher number of grains resulted visible.

Furthermore the thin slices were prepared through impregnation with blue colored epoxy resin, in order to distinguish under normal light the second treatment from the hybrid material under study. The blue color is in fact due to the epoxy resin added later to prepare the microscopy slides and represents the voids left after the consolidating treatment. Some examples are reported in the following pages.

From the comparison between the images obtained, it can be seen as the contact surface between the grains results higher in the samples prepared using a mixture of sands with a wider corn-size distribution, than in those prepared using only the sand DORTISILIT NR 9H. In particular in Figure 8.1 a larger free space between the grains can be noticed. Therefore the possibility of film formation and of effective consolidation for samples prepared with mixed sand results higher.

The samples prepared with a larger corn size distribution (Figure 8.2 and 8.4) result on the other hand consolidated in a more effective way. The voids between large corns are filled by the smaller corns. this can be easier observed with the polarized light (Figure 8.3 and 8.5) since the smaller grains are embedded in the amorphous matrix due to the consolidant and can't be seen under normal light. The presence of the smaller grains provide in fact a larger contact surface between the grains and promotes the formation of the amorphous phase as film between them.

These observations agree with the fact that the samples prepared with mixed sand result more compact and hard than those prepared only with large corn sand, which result fragile and crumbly.
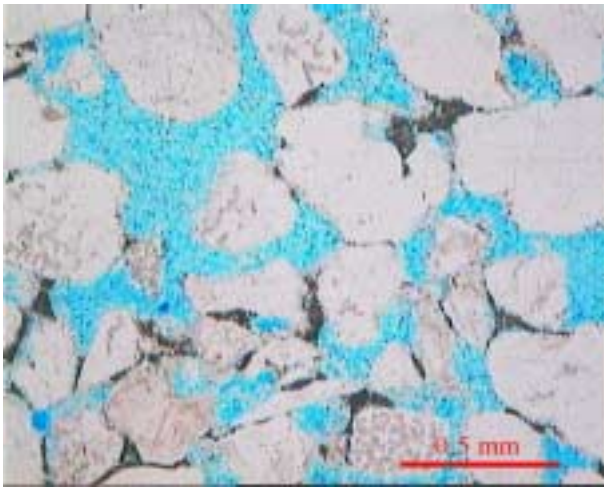
Figure 8. 1   DBP2T2,   Sand: Dortsilit NR9H
Voids between grains can be seen in blue colour.
The consolidant is present as film between the grains.
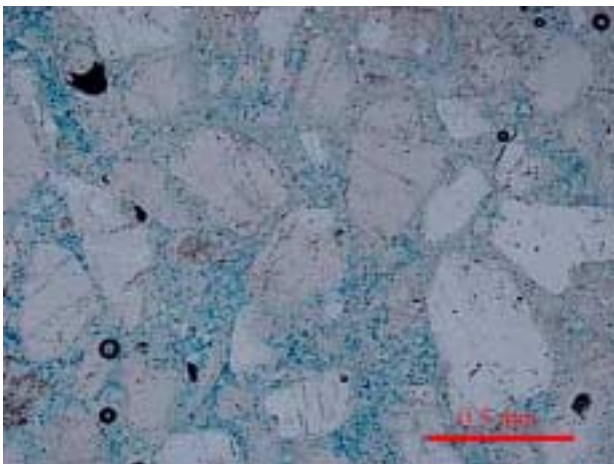
Figure 8.2   DBP2T2, sand: 75 % wt. of DORTSILIT NR 9H and 25 % wt.   of   DORSILIT   6400. normal light.
Most of the space between grains is filled
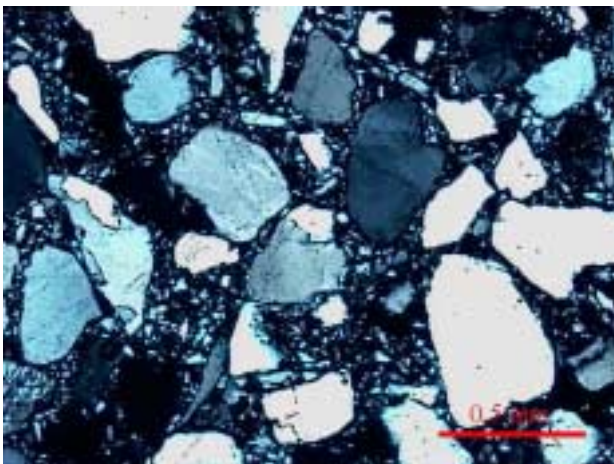
Figure 8. 3   DBP2T2, sand: 75 % wt. of DORTSILIT NR and   25 % wt.   of   DORSILIT   6400. polarized light. Space between grains   is   filled   by   smaller grains   embedded   in   an amorphous phase.
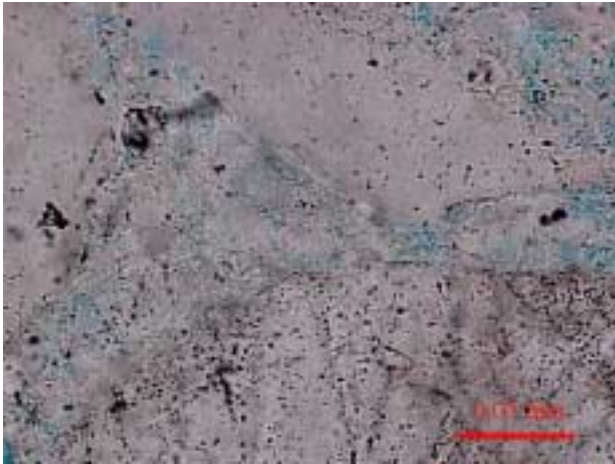
Figure 8. 4 DBTEOS, sand: 75 % wt. of DORTSILIT NR 9H and 25 % wt. of DORSILIT 6400. normal light.
Amorphous material between sand grains.
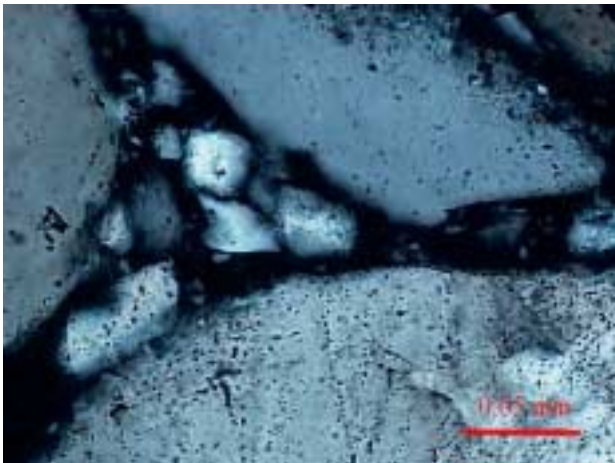
Figure 8. 5 DBTEOS, sand: 75 % wt. of DORTSILIT NR 9H and 25 % wt. of DORSILIT 6400. polarized light.
Smaller grains are embedded in the amorphous phase.

8.4   Scanning Electron Microscopy (SEM)

The images obtained by Scanning Electron Microscopy (SEM) [108, 109] on the fracture surface of the sand disks, confirm what has already been observed by optical microscopy. The space between larger sand grains is filled by smaller grains, but many voids are left. The disposition of the grains results a casual packing. It's possible to see how the grains are held together by a film of the hybrid material on the contact surface, but it's impossible to distinguish correctly the grains from the amorphous material. Only two example photos are reported (Figure 8.6 and 8.7).
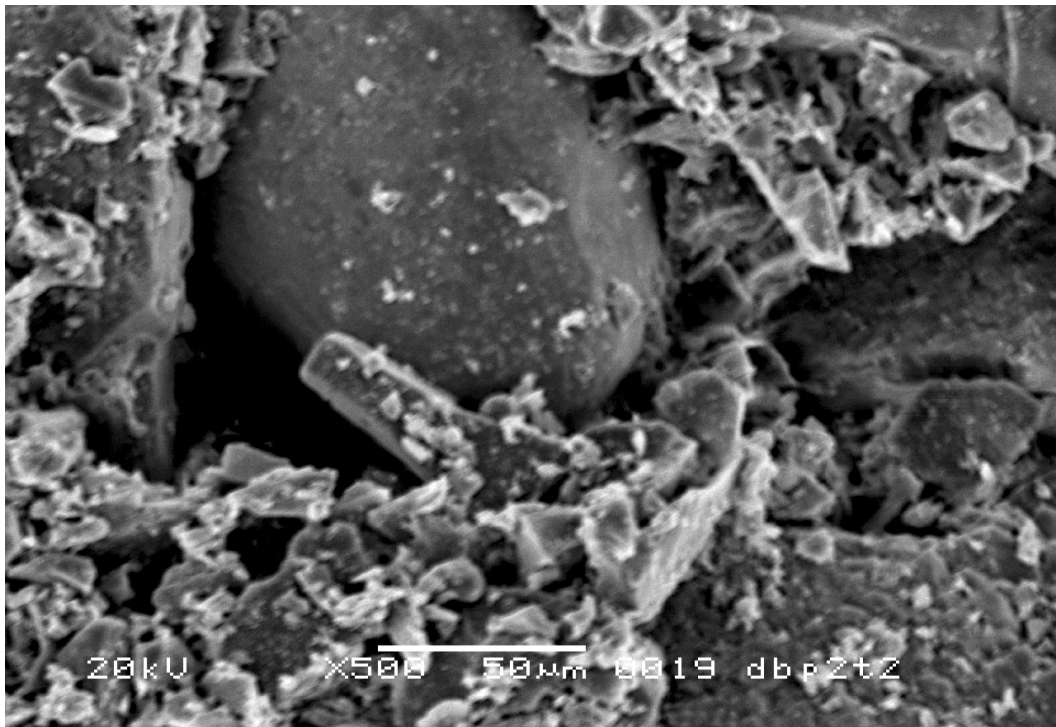
Figure 8. 6   SEM photo of the sand disk sample DBP2T2, fracture surface
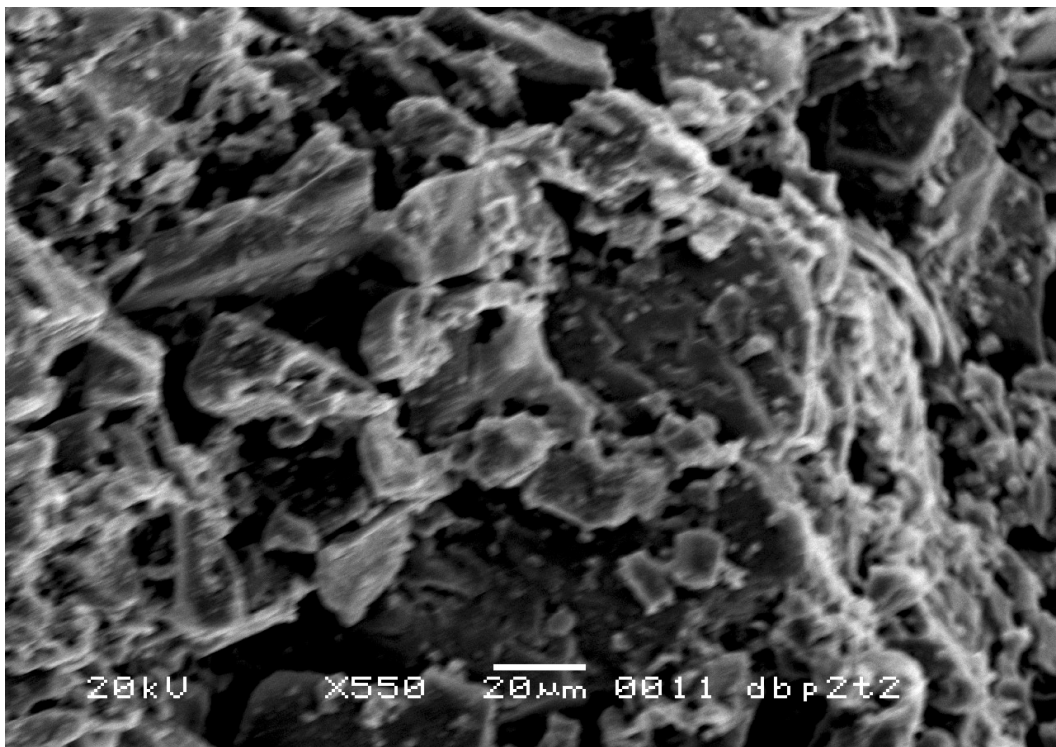
Figure 8. 7   SEM photo of the sand disk sample DBP2T2, fracture surface

8.5   Biaxial Flexural Strength

The biaxial flexural strength experiment was done to check the consolidating effect of the hybrid materials studied. The same solutions used for the preparation of the thin films via dip-coating were used to impregnate the sand as described in the sample preparation paragraph to form disk-shaped samples. To obtain a more accurate value five samples for every solution were prepared. The mean value for the E-Modulus and for the hardness parameter σ (rupture modulus) are reported together with the error calculated as the half of the difference between the higher and the lower value. In figure 8.8 and 8.9 the mean σ values are reported against the theoretical percentage of silica in the hybrid material used as consolidant. The percentage of silica is calculated assuming that all the TEOS present in the starting solution has proceeded towards complete reaction to SiO_2.

As expected, the σ value increases as the content of PMMA in the starting solution becomes higher, because of the adhesive and mechanical properties of the acrylic resin. A first difference can be noted between the samples prepared using solutions with DBTL and acid catalysis. The first ones show a linear growth of the σ value with respect to the variation of the components of the solution. (Figure 8.8) This confirms the formation of hybrids with properties that are a different from those of the two starting materials.

Furthermore the linear dependence of the σ value on the composition of the starting solution suggests the possibility to tune the properties of the material depending on the requirements of the practical applications. The samples prepared with acid catalysis, on the other hand, show a step-like dependence of σ at about 50 % of silica content.(Figure 8.9) This phenomenon is probably due to the macroscopic phase separation between PMMA and silica gel, already observed during the film formation (Chapter 6). Due to that, no hybrid material is formed, and the properties of the consolidated disks depend on the component present in larger amount.

The E-modulus was also calculated and reported against the percentage of silica (Figure 8.10 and 8.11). This parameter gives less information than σ, as result from the fact that the value remains almost constant between the errors. It must be noted that the E-modulus regards not the hybrid material alone, but the whole system. In this case the

elasticity is mostly due to the fact that, once consolidated, the sand corns are packed together in the same casual way, as it results from SEM and polarization microscopy pictures, not depending on the consolidant used. In this system the E-modulus results random distributed around the same value.

Table 8. 4 **Rupture modulus σ and E-Modulus value of the sand disk samples, DBTL and HCl series. The 5 experimental values and the mean value are reported for the five disks prepared with each starting solution.**

TEOS DBTL

	σ (N/mm^2)	E (kN/mm^2)
A	-	-
B	0,14	0,23
C	0,22	0,47
D	0,28	2,42
E	0,26	3,19
mean	**0,225**	**1,5775**
max error	**0,07**	**1,48**

TEOS HCl

	σ (N/mm^2)	E (kN/mm^2)
A	0,34	0,65
B	0,23	0,8
C	0,36	0,92
D	0,3	0,86
E	0,47	0,74
mean	**0,34**	**0,794**
max error	**0,12**	**0,135**

DBP1T4

	σ (N/mm^2)	E (kN/mm^2)
A	0,34	1,15
B	0,53	-
C	0,47	-
D	0,83	2,48
E	-	-
mean	**0,5425**	**1,815**
max error	**0,245**	**0,665**

HCLP1T4

	σ (N/mm^2)	E (kN/mm^2)
A	0,5	3,77
B	0,27	0,71
C	0,77	1,82
D	0,64	1,43
E	0,94	3,72
mean	**0,624**	**2,29**
max error	**0,335**	**1,53**

DBP2T3

	σ (N/mm^2)	E (kN/mm^2)
A	0,76	2,54
B	0,72	2,38
C	0,79	2,13
D	0,85	-
E	0,88	1,98
mean	**0,8**	**2,2575**
max error	**0,08**	**0,28**

HCLP2T3

	σ (N/mm^2)	E (kN/mm^2)
A	1,2	4,04
B	0,89	2,75
C	1,13	4,67
D	1,26	2,55
E	1,29	5,03
mean	**1,154**	**3,808**
max error	**0,2**	**1,24**

DBP2T2

	σ (N/mm^2)	E (kN/mm^2)
A	0,77	3,07
B	0,80	-
C	0,93	3,46
D	1,29	6,27
E	0,99	-
mean	**0,956**	**4,26666667**
max error	**0,26**	**1,6**

DBP3T1

	σ (N/mm^2)	E (kN/mm^2)
A	1,21	2,42
B	1,53	4,17
C	1,01	1,69
D	1,46	3,04
E	1,3	2,64
mean	**1,302**	**2,792**
max error	**0,26**	**1,24**

HCLP2T2

	σ (N/mm^2)	E (kN/mm^2)
A	1,12	2,96
B	0,99	4,48
C	1,13	-
D	1,34	2,61
E	1,35	2,43
mean	**1,186**	**3,12**
max error	**0,18**	**1,025**

HCLP3T1

	σ (N/mm^2)	E (kN/mm^2)
A	0,99	-
B	0,8	0,8
C	0,92	1,63
D	1,64	4
E	1,26	1,96
mean	**1,122**	**2,0975**
max error	**0,42**	**1,6**

PMMA

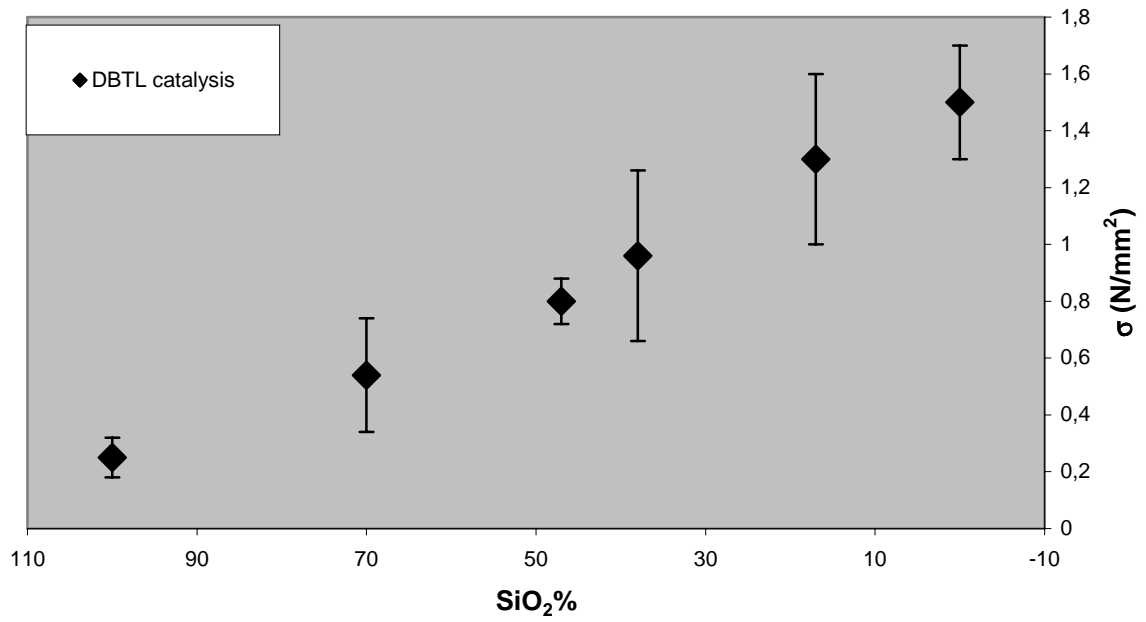|	σ N/mm^2	kN/mm^2
A	1,37	2,13
B	1,59	4,59
C	1,43	3,57
D	1,73	3,19
E	1,35	-
mean	**1,494**	**3,37**
max error	**0,19**	**1,23**

Figure 8. 8   **Rupture modulus σ for the DBTL catalysed series**
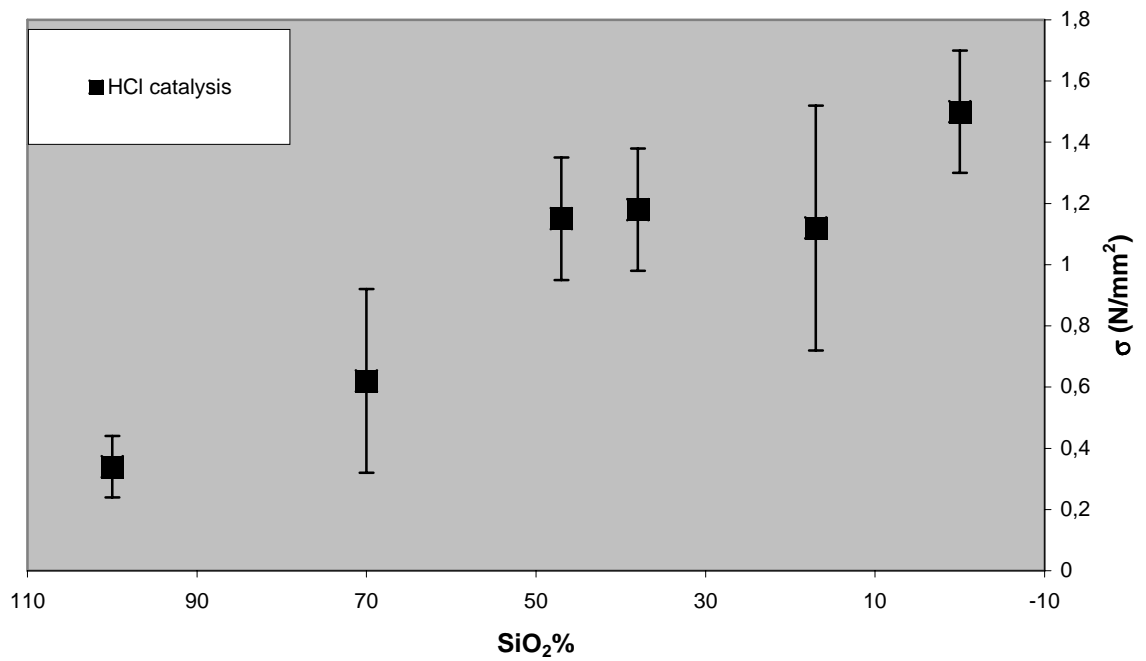

Figure 8. 9   **Rupture modulus σ for the HCl catalysed series**

Figure 8. 10   E-Modulus for the DBTL catalysed series
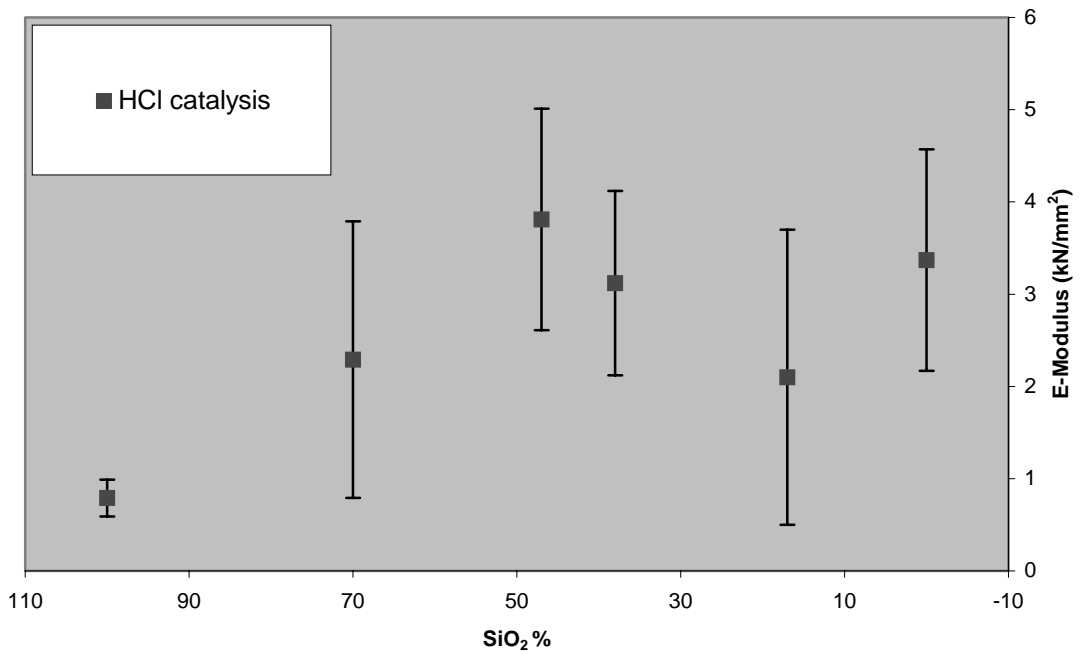
Figure 8. 11   E-Modulus for the HCl catalysed series

8.6   Conclusions

The behaviour of the mixtures, whose properties on a nanometer scale were studied in chapter 6, has been tested in a more complex system, simulating the behaviour of the materials in the stone's structure. The images obtained by Scanning Electron Microscopy and polarization microscopy reveal a casual disposition of the grains, which are held together by the consolidant. The use of a sand mixture with a wide corn-size distribution increases the contact surface between the grains and from the images, it can be seen how the smaller corns fill the voids between the larger ones. Photos obtained using polarized light made it possible to distinguish the small grains (10-100 μ) from the amorphous consolidating material. This material, added as solution, forms films between the grains, leading to the consolidation of the sand in disk-shaped forms.

The mechanical properties of the samples so obtained have been tested, and as result a difference between the samples prepared using DBTL or acid catalysis can be seen. In the first case, in fact, the material added seems to be a real hybrid, whose properties are tunable depending on the composition of the starting solution. In the case of the acid catalysis, a phase separation occurs, as confirmed also from the data obtained from the study of the materials alone (Chapter 6, 7).

These results, which were obtained on model systems, are of great importance in order to develop new materials with the properties required from practical applications and to acquire new information about the commercial products already in use, by the employment of different analytical methods.

Chapter 9

Analysis of the technological product

9.1   Introduction

The methods applied in the previous chapters to study the structural evolutions involved in the formation of an hybrid material, can be also used to characterize more specifically an already existing technical product.

For this reason the same measurements applied to the model system, described until now, were applied to a technological product, which for reasons of industrial secret will be here called with the acronym GS001.

The product GS001 is principally composed by a solution which, once applied, produces via sol-gel process the hybrid material for the consolidation of the natural stone. The solvent used, as well as the exact composition of the acrylic resin used, cannot be reported here.

The results obtained on this product give an idea about the perspectives and the possible application of this method based on AFM microscopy not only in the field of the pure research but also for the analysis of industrial products.

9.2   Atomic Force Microscopy analysis.

Films were made with dip coating technique using the product GS001 as received. Substrates used were normal glass. Different samples were prepared varying the withdrawal speed. This means varying the film thickness in order to check the effect on the topography of the film. Although the films resulted all transparent and homogeneous at a first sight, they revealed different features under AFM analysis. Similarly to what is described in the theory of the sol-gel process, beyond a critical thickness the topography of

the film shows in fact the presence of fractures and cracks, due most probably to the different evolution of the material at the interface with the air and at the interface with the substrate.

The topography of the film GS001-A, (Figure 9.1) which was obtained with the slowest withdrawal speed, is the only one which doesn't show cracks. Comparison with the model system can be hardly done because of the substantial differences between the solutions used for the model and the solution of GS001 (i.e. viscosity, solvent, concentration of the reagents).

Force modulation experiments didn't give any contrast between the two phases and couldn't be done without damaging the surface, owing to the different acrylic resin used. They are therefore not reported.

Force plot experiments were conducted on the film GS001-A, following the method described in Chapter 6. Results are reported in table 9.1. The stiffness of the material results greater than that of the materials analyzed previously (see chapter 6.5.3).

Table 9.1   Topographical properties of the film GS001-A and force plot result.

Aspect	Transparent, homogenous
Roughness RMS	9,88 nm
Roughness Ra	7,48 nm
Z range	91,183 nm
Force plot slope (normalized to Silicon)	0,956

9.3   Biaxial Flexural Strength

The Biaxial flexural strength was used to test the effectiveness of the consolidation properties of the product GS001. The samples were prepared as described in chapter 8, using the product to consolidate sand disks. The results are reported in table 9.2 and if they are compared with the data reported in table 8.4 for the SiO_2/PMMA samples it can be

seen as the product GS001 is a better stone consolidant than the mixtures used as model system.
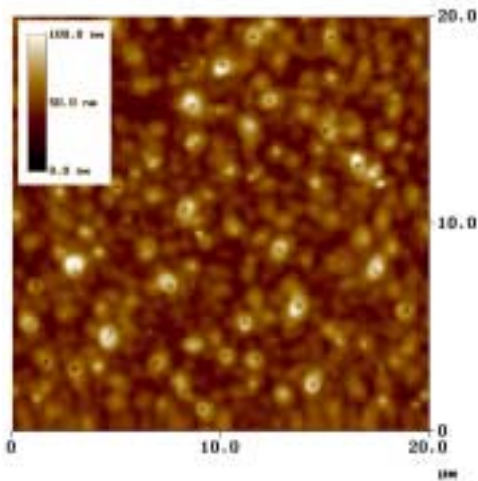
Figure 9.1   Film GS001-A
dipping :0,05 ± 0,007 cm/sec
withdrawal: 0,033 ± 0,005 cm/sec
T = 25 °C
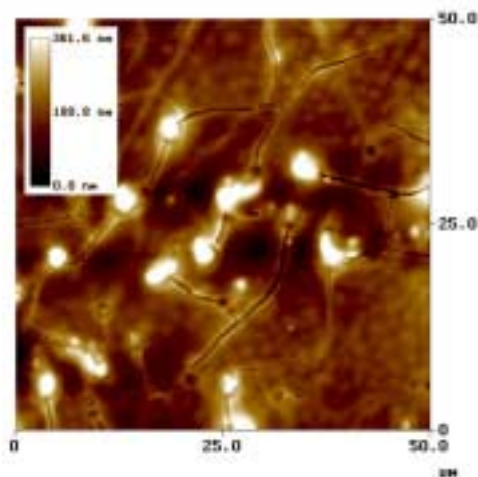
Figure 9.2   Film GS001-B
dipping: 0,14 ± 0,02 cm/sec
withdrawal: 0,13 ± 0,02 cm/sec
T = 25 °C
The film is thicker and some cracks can be seen.
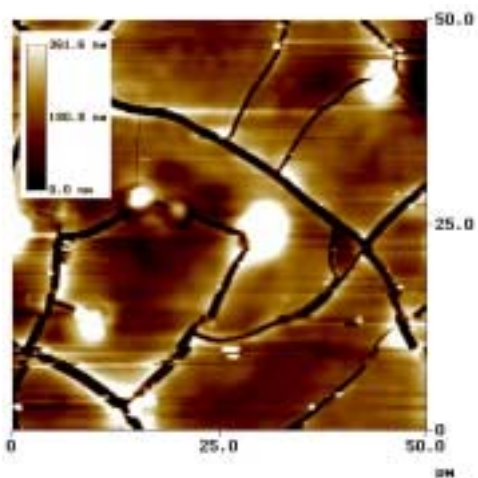
Figure 9.3   Film GS001-C
dipping: 0,27 ± 0,03 cm/sec
withdrawal: 0,21 ± 0,03 cm/sec
T = 25 °C
The film is too thick to dry without the formation of structural defects.

The rupture modulus σ results in fact higher than in the other samples, indicating an effective consolidation of the sample, while the E-modulus remains low enough not to have a brittle and fragile sample. These differences are due to the fact that the product GS001 uses an acrylic resin other than PMMA and with better mechanical properties.

Table 9.2   **Biaxial flexural strength data on the sample prepared with GS001**

sample name	mean diameter (mm)	mean thickness (mm)	rupture modulus (σ N/mm^2)	E-modulus (kN/mm^2)
GS001 a	46,43	5,75	1,57	2,7
GS001 b	47,20	5,55	2,14	3,81
GS001 c	46,87	6,12	1,31	0,87
GS001 d	46,72	5,45	2,13	3,35
GS001 e	46,83	5,62	1,52	2,37
Mean value			1,74	2,62
Max. error			0,4	1,5

9.4   Conclusions

The analysis of the technological product shows how the method developed here and based on the AFM microscopy can provide not only many valuable information to understand the development of a system as complex as that of the formation of an hybrid material, but, together with other common techniques, can also be used for a better characterization of an industrial product. These information represent in fact a great help in the development of the product and in its characterization, especially if the analysis is made in order to compare different samples or the effectiveness of different products.

Conclusions

This work shows how an approach based on AFM combined with Force Modulation and other common techniques, is a valuable tool in understanding the structure of composite materials on nano- and micrometer scales. In particular, thin films of such materials were studied, which is particularly useful in order to understand their use as natural stone consolidants. In fact, the composite materials investigated here as model films should not be too different from those formed among stone grains under real operational conditions. Moreover, the approach described here offers the remarkable opportunity of a rapid testing of compositional variables.

The model system studied here, imitates, in fact, the materials actually used, at the same time maintaining the simplicity necessary to reach a good control of all the compositional variables. The experimental path chosen involves the use of different solutions to produce, via sol-gel, nanocomposite hybrid materials based on Silica and Polymethylmethacrylate with different Silica/Polymethylmethacrylate ratios. In this way different experimental parameters could be controlled and varied in order to understand the evolution of the nanostructure of the system.

The samples were synthesized using acid or dibutyltindilaurate $(CH_3CH_2CH_2CH_2)_2Sn[OCO(CH_2)_{10}CH_3]$ catalysis and prepared as both thin films and monoliths. The use of this model system made it possible to advance some hypotheses about the mechanism involved in the phase separation process. In fact, it was observed how the phase separation process can follow the spinodal decomposition path or the nucleation one, depending on the composition of the starting solution.

In order to understand how these systems evolve after the relevant initiation steps the Atomic Force Microscopy (AFM), combined with the Force Modulation technique, was used. This approach to the nanocomposite hybrid materials is totally new and allows a further insight in the nanostructure of these kind of materials. In this way it was possible to verify the topography of the materials together with their elastic properties. Force modulation analysis, in fact, allowed us to observe how the two phases separate, by

creating a map of the relative hardness on the surface of the resulting material. This analysis, together with other conventional techniques, i.e. IR spectroscopy, helped us to understand the evolution of the system starting from different compositional variables.

In particular, the role of dibutyltindilaurate (DBTL) as catalyst for the sol-gel process was studied, comparing it with the standard acid catalysis. Materials produced with the two catalysts showed, in fact, many structural and compositional differences.

This opens new perspectives for the use of this catalyst for such an application, as its properties in the sol-gel catalysis are scarcely described in literature.

The consolidating properties of the materials studied were also tested on a macroscopic scale, and quartz sand samples were used to mimic the effect of the hybrid materials on completely loosened sand stone. The mechanical properties obtained through a biaxial flexural strength test were compared with the distribution of the consolidant between the grains, which were observed with polarization microscopy. These results represent the connection with the practice, which is necessary to develop a new method to produce and analyze such hybrid materials as natural stone hardeners.

Further steps will be done using the method developed in this work, to test the effect of changing other compositional variables such as solvent, temperature and content of water. This method based on Force Modulation and AFM can also be used in general to test the properties of other hybrid materials independently from the practical application.

Abbreviations

AFM	Atomic Force Microscopy
DBTL	Dibutyltindilaurate $(CH_3CH_2CH_2CH_2)_2Sn[OCO(CH_2)_{10}CH_3]$
EFM	Electric Force Microscopy
FESP	Force-modulation Etched Silicon Tip
FT-IR	Fourier Transform Infrared Spectroscopy
LFM	Lateral Force Microscopy
MFM	Magnetic Force Microscopy
MMA	Methylmethacrylate CH_2:$C(CH_3)COOCH_3$
MA.-%	percent mass
PEOX	polyethyloxazoline
PMMA	Polymethylmethacrylate
SEM	Scanning Electron Microscopy
SPM	Scanning Probe Microscopy
STM	Scanning Tunneling Microscopy
TEOS	Tetraethoxysilane $(CH_3CH_2O)_4Si$
TESP	Tapping Etched Silicon Tip
THF	Tetrahydrofurane

Literature

[1]   E.M.Winkler, *Stone in architecture – Properties, Durability*, Springer-Verlag, Berlin, Heidelberg. **1997**.

[2]   L.Lazzarini, M.Laurenzi-Tabasso, *Il restauro della pietra*, Cedam edit., Padova **1986**.

[3]   R.Snethlage, *Steinkonservierung – Forschungsprogramm des Zentrallabors für Denkmalpflege 1979-1983. Arbeitsheft 22* – Bayerische Landesamt für Denkmalpflege, München. **1984**

[4]   G. G. Amoroso, V. Fassina, *Stone Decay and Conservation (Atmospheric Pollution, Cleaning, Consolidation and Protection)*, Elsevier, **1983**.

[5]   C. V. Horie, *Materials for Conservation (Organic Consolidants, Adhesive and Coatings)*, Butterworth-Heinemann, **1987**.

[6]   L.Sattler, R.Snethlage, *Engineering Geology of ancient Works, Monuments and Historical sites, Athen* 19/09-23/09/88, 953-956, Marinos & Koukis (eds), Rotterdam: Balkema. **1988.**

[7]   K. Hempel, A. Moncrieff, *Report on Work Since Last Meeting in Bologna, October 1971,* Rossi-Manaresi, Raffaella ed. **1976**.

[8]   Wittman F. H., Prim P., (1983) *Materiaux et Contructions (Materials and structures),* 94 (16), 235-242, **1983**.

[9]   Drillmore, *Proceedings of the workshop*, Drilling Methodologies for monuments restoration, Münich, March **2000**.

[10]   M. A. Nugent, S. L. Brantley, C. G. Pantano, P. A. Maurice, *Nature*, 395, 588-591, **1998**.

[11]   C. M. Eggleston, S. R. Higgins, P. A. Maurice, *Env. Sci. & Tech. : news and research notes*, 32 (19), **1998**.

[12]   C.Zilg, R.Mülhaupt, J.Finter, *Macromol.Chem.Phys.*, 200, 661-670, **1999**.

[13]   E. P. Giannellis, *Adv. Mater.*, 8 (1), 29-35, **1996**.

[14]   M Zanetti, S. Lomakin, G. Camino, *Macromol. Mater. Eng.*, 279, 1-9, **2000**.

[15]   J.Wen, G.L.Wilkes, *Chem. Mater.*, 8, 1667-1681, **1996**.

[16]   P.Judenstein, C.Sanchez, *J.Mater.Chem.*, 6(4), 511-525, **1996**.

[17]   L.Mascia, *La chimica e l'industria*, 80, 623-628, **1998**.

[18]   L. Mascia, T. Tang, *J. Mater. Chem.*, 8 (11), 2417-2421, **1998**.

[19]   L. A. Schwegler, M. Möller, *Macromol. Chem. Phys.,* 199 (9), 1859-1864, **1998**.

[20]   Y. Wei, D. Jin, C. Yang, G. Wei, *J. Sol-Gel Sci. Technol.,* 7, 191-201, **1996**.

[21]   A. B. Wojcik, L. Klein, *J. Sol-Gel Sci. Technol.*, 5, 77-82, **1995**.

[22]   C. J. T. Landry, B. K. Coltrain, D. M. Teegarden, T. E. Long, V. K. Long, *Macromolecules*, 29 (13), 4712-4721, **1996**.

[23]   T.Saegusa, *Macromol.Symp.* 98, 719-729, **1995**.

[24]   I. A. David, G. W. Scherer, *Chem. Mater.,* 7, 1957-1967, **1995**.

[25]   B.K.Coltrain, C.J.T.Landry, J.M.O'Reilly, A.M.Chamberlain, G.A.Rakes, J.S.Sedita, L.W.Kelts, M.R.Landry, V.K.Long, *Chem.Mater.,* 5, 1445-1455, **1993**.

[26]   Y. Wei, D. Jin, D.J. Brennan, D.N. Rivera, Q. Zhuang, N.J. DiNardo, K. Qiu, *Chem. Mater.*, 10, 769-772, **1998**.

[27]   T. Çaykara, O. Güven, Ş. Süzer, *Polymer,* 39 (21), 5269-5271, **1998**.

[28]   C. Bruchertseifer, K. Stoppek-Langner, J. Grobe, M. Deimel, A. Benninghoven, *Fresenius J. Anal. Chem.,* 358, 273-274, **1997**.

[29]   R. Bishoff, S.E. Cray, *Prog. Polym. Sci.,* 24, 185-219, **1999**.

[30]   J.M. Yang, H.S. Chen, Y.G. Hsu, F.H. Lin, Y.H. Chang, *Angew.Makromol.Chem.*, 251, 49-60, **1997**.

[31]   J.M. Yang, H.S. Chen, Y.G. Hsu, F.H. Lin, Y.H. Chang, *Angew.Makromol.Chem.*, 251, 61-72, **1997**.

[32]   C.J. Brinker, G.W. Scherer, *Sol-Gel Science: The Physics and Chemistry of Sol-Gel Processing*, Academic Press, New York, **1990**.

[33]   R. J. P. Corriu, D. Leclerq, *Angew. Chem. Int. Ed. Engl.,* 35, 1420-1436, **1996**.

[34]   U. Schubert, *J. Chem. Soc., Dalton Trans.,* 3343-3348, **1996**.

[35]   C. Roger, M. Hampden-Smith, *Chemtech*, 26-31, October **1993**.

[36]   D. C. Bradley, R. C. Mehrotra, D. P. Gaur, *Metal Alkoxides, Academic Press,*
          1978.

[37]   R. Campostrini, G. Carturan, G. Soraru', P. Traldi, *J. Non-Cryst. Solids*, 108,
          315-322, **1989**.

[38]   C. A. Morris, M. L. Anderson, R. M. Stroud, C. I. Merzbacher, D. R. Rolison,
          Science, 284, 622-624, **1999**.

[39]   G. Binnig, H. Roher, C. Gerber, E. Weibel, *Phys. Rev. Lett.* 49, 57, **1982.**

[40]   G. Binnig, H. Roher, *Helv. Phys. Acta*, 55, 726, **1982**.

[41]   G. Binnig, C. F. Quate, C. Gerber, *Phys. Rev. Lett.* 56, 930, **1986.**

[42]   G. Friedbacher, *Nachr. Chem. Tech. Lab.*, 43 (3), 342-346, **1995**.

[43]   U.D. Schwarz, 287-842, *Scanning Force Microscopy*, in S. Amelinckx, D. van
          Dyck, J. van Landuyt, G. van Tandeloo, *Handbook of Microscopy (application
          in materials Science, Solid-State Physic and Chemistry)*, VCH Verlag, **1997.**

[44]   C. F. Quate, *The AFM as a Tool for Surface Imaging*, ed. Surf.Science., **1994**.

[45]   Y. Martin, H.K. Wickramasinghe, *Appl. Phys. Lett.*, 50, 1455, **1987**.

[46]   R. Proksch, G. D. Skidmore, E. D. Dahlberg, S. Foss, J. J. Schmidt, C. Merton,
          Appl. Phys. Lett., 69 (17), 2599-2601, **1996**.

[47]   R. Proksch, P. Neilson, S. Austvold, J. J. Schmidt, *Appl. Phys. Lett.*, 74 (9), 1308-1310, **1999**.

[48]   F. Saurenbach, B. D. Terris, *Appl. Phys Lett.*, 56 (17), 1703-1705, **1990**.

[49]   C.H. Ahn, T. Tybell, L. Antognazza, K. Char, R.H. Hammond, M.R. Beasley, Fischer, and J.-M. Triscone. *Science*, 276, 1100, **1997**.

[50]   R. Overney, E. Meyer, *MRS Bull.*, 19, 26, **1993**.

[51]   S. Yamamoto, H. Yamada, *Langmuir*, 13, 4861-4864, **1997**.

[52]   R.M. Overney, E. Meyer, J. Frommer, H.-J. Güntherodt, M. Fujihira, H. Takano, Y. Gotoh, *Langmuir*, 10, 1281-1286, **1994**.

[53]   A.A. Galuska, R.R. Poulter, K.O. McElrath, *Surface and Interface Analysis,* *25*, 418-429, **1997**.

[54]   S. N. Magonov, V. Elings, V.S. Papkov, *Polymer*, 38 (2), 297-307, **1997**.

[55]   D.Sarid, J.P.Hunt, R.K.Workman, X.Yao, C.A.Peterson, *Appl. Phys. A*, 66, S283-S286, **1998**.

[56]   L.Delineau, R.Brandsch, G.Bar, M.-H.Whangbo, *Surface Science*, 448, L179-L187, **2000**.

[57]   G.Bar, R.Brandsch, M.Bruch, L.Delineau, M.-H.Whangbo, *Surface Science*, 444, L11-L16, **2000**.

[58]   F. J. Giessibl, *Appl. Phys. Lett.*, 76 (11), 1470-1472, **2000**.

[59]   F. J. Giessibl, S. Hembacher, H. Bielefeldt, J. Mannhart, *Science*, 289, 422-425, **2000**.

[60]   S. J. O'Shea, M. E. Welland, *Langmuir*, 14, 4186-4197, **1998**.

[61]   R.Raiteri, H.-J.Butt, D.Beyer, S.Jonas, *Phys. Chem. Chem. Phys.*, 1, 4881-4887, **1999**.

[62]   W. F. Heinz, J. H. Hoh, *Trends in Biotechnology*, **17** (*4*), 143-150, **1999**.

[63]   Instruction Manual, Digital Instruments, **1997**.

[64]   Courtesy of Digital Instruments (instruction manual)

[65]   C. M. Lieber, *Chem & Eng. Ne*ws, 28-41, Apr. 18, **1994**.

[66]   B.Cappella, G.Dieter, *Surface Science Reports*, 34, 1-104, **1999**.

[67]   A.Moore, P.M.Williams, M.C.Davies, D.E.Jackson, C.J.Roberts, S.J.B.Tendler, *J.Chem.Soc.,Perkin Trans.,* 2, 253-258, **1998**.

[68]   A.Döppenschmidt, M.Kappl, H.-J.Butt, *J. Phys. Chem. B*, 102 (40), 7813-7819, **1998**.

[69]   L.-O. Heim, J. Blum, M. Preuss, H.-J. Butt, *Phys. Rev. Lett.*, 83 (16), 3328-3331, **1999**.

[70]   R.Raiteri, H.-J.Butt, D.Beyer, S.Jonas, *Phys. Chem. Chem. Phys.*, 1, 4881-4887, **1999**.

[71]   M.H.Whangbo, S.N.Magonov, H.Bengel, *Probe Microscopy,* OPA (Overseas Publisher Association), Amsterdam, Vol. 1, pp.23-42, **1997**.

[72]   J.Domke, M.Radmacher, *Langmuir*, 14, 3320-3325, **1998**.

[73]   A.K.Jämting, J.M.Bell, M.V.Swain, L.S.Wielunski, R.Clissold, *Thin Solid Films*, 332, 189-194, **1998**.

[74]   G.Bar, L.Delineau, R.Brandsch, M.Bruch, M.-H.Whangbo, *Appl. Phys. Lett.*, 75 (26), 4198-4200, **1999**.

[75]   J.A.Ogilvy, *J. Phys. D: Appl. Phys.*, 26, 2123-2131, **1993**.

[76]   B.Bhushan, J.N.Israelachvili, U.Landman, *Nature*, 374, 607-616, **1995**.

[77]   B.Bhushan, V.N.Koinkar, *Appl. Phys. Lett.*, 64 (13), 1653-1655, **1994**.

[78]   N.A.Burnham, R.J.Colton, *J. Vac. Sci. Technol.*, A7 (4), 2906-2913, **1989**.

[79]   M.Kempf, M.Göken, H.Vehoff, *Appl. Phys. A*, 66, S843-S846, **1998**.

[80]   M.S.Bobij, S.K.Biswas, J.B.Pethica, *Appl. Phys. Lett.*, 71 (8), 1059-1061, **1997**.

[81]   E.Liu, B.Blanpain, J.-P.Celis, J.R.Roos, *J. Appl. Phys.*, 84 (9), 4859-4865, **1998**.

[82]   W. Shen, S. M. Smith, F. N. Jones, C. Ji, R.A. Ryntz, M. P. Everson, *Journal of Coatings Technology*, 69 (873), 123-135, **1997**.

[83]   M. Troyon, Z. Wang, D. Pastre, H. N. Lei, A. Hazotte, *Nanotechnology*, 8, 163-171, **1997**.

[84]   B.Reusch, J.Geis-Gestorfer, Ch.Ziegler, *Appl. Phys. A*, 66, S805-S808, **1998**.

[85]   J.P.Aimé, Z.Elkaakour, C.Odin, T.Bouhacina, D.Michel, J.Curély, A.Dautant, *J. Appl. Phys.*, 76 (2), 754-762, **1994**.

[86]   G. Müller, M. Raith, *Methoden der Dünnschiliffmikroskopie, Clausthaler Tektonische Hefte 14*, Sven von Longa Verlag, **1993**.

[87]   R. Telle, G. Petow, F. Mücklich, 7-31, *Fundamental of Light Microscopy*, in S. Amelinckx, D. van Dyck, J. van Landuyt, G. van Tandeloo, *Handbook of Microscopy (application in materials Science, Solid-State Physic and Chemistry),* VCH Verlag, **1997**.

[88]   R. Telle, G. Petow, F. Mücklich, 33-53, *Optical Contrasting Microstructure*, in S. Amelinckx, D. van Dyck, J. van Landuyt, G. van Tandeloo, *Handbook of Microscopy (application in materials Science, Solid-State Physic and Chemistry), VCH Verlag*, **1997**.

[89]   W. D. Callister Jr., *Materials science and engineering-an introduction*, Wiley ed., **1991**.

[90]   G. Weiss, *Allgemeine und Angewandte Geologie, Rehie B*, 31-32, Friedrich Pfeil Verlag, München, **1992**.

[91]   L. Sattler, *Untersuchungen zu Wirkung und Dauerhaftigkeit von Sandsteinfestigungen mit Kieselsäureester.*, 20-31, Doktorarbeit – Landesamt für Denkmalpflege, **1992**.

[92]   B. Jousseaume, V. Gouron, M. Pereyre, J-M. Francès, *Applied Organometallic Chemistry*, 5, 135-138, **1991**.

[93]   J.Evans, S.Karpell, *J.Organomet.Chem.Libr.*, 16, 83-95, **1985**.

[94]   F.W.Van der Weij, *Makromol.Chem.*, 181, 2541-2548, **1980**.

[95]   G. Schiavon, *tesi di laurea presso l'Universita' degli studi di Padova*, **1997**.

[96]   L.Armelao, R.Bertoncello, S.Coronaro, A.Glisenti, *Science and Technology for Cultural Heritage*, 7 (2), 47-69, **1998**.

[97]   J.W.Cahn, *J.Chem.Phys.* 42,1,93-99, **1965**.

[98]   Y.S.Lipatov, *Colloid chemistry of Polymers* (Elsevier)

[99]   P. G. de Gennes, *J. Chem. Phys.,* 72 (9), 4756-4763, **1980**.

[100]   S.Reich, Y.Cohen, *J.Polym.Sci.,Polym.Phys.Ed.*, 19, 1225, **1981**.

[101]   M. Böltau, S. Walheim, J. Mlynek, G. Krausch, U. Steiner, *Nature*, 391, 877-879, **1998**.

[102]   S.Walheim, M.Böltau, J.Mlynek, G.Krausch, U.Steiner, *Macromolecules*, 30, 4995-5003, **1997**.

[103]   C. J. T. Landry, B. K. Coltrain, B. K. Brady, *Polymer,* 33 (7), 1486-1495, **1992**.

[104]   C.Landry, B.K.Coltrain, J.A.Wesson, N.Zumbuyadis and J.Lippert, *Polymer*, 33 (7) 1496-1506, **1992**.

[105]   H.Sakai, Y.Imamura, *Bull.Chem.Soc.Jpn*., 53, 1749-1750, **1980**.

[106]   K. K. Kalnin'sh, A. N. Krasovskii, B.G. Belen'kii, G.A. Andreyeva, *Polymer Sci. USSR*, 18, 2636-2644, **1976**.

[107]   R. M. Silverstein, G. C. Bassler, *Spectrometric identification of organic compounds*, Wiley.

[108]   S. L. Flegler. J. Heckmann, K. L. Klomparens, *Elektronenmikroskopie, Grundlagen, Methoden, Anwendungen*, Spektrum Verlag, **1995**.

[109]   S. Amelinckx, D. van Dyck, J. van Landuyt, G. van Tandeloo, *Handbook of Microscopy (application in materials Science, Solid-State Physic and Chemistry)*, 537-561, VCH Verlag, **1997.**